Szymon Nosewicz

DISCRETE ELEMENT MODELING OF POWDER METALLURGY PROCESSES

Supervisor: dr hab. Jerzy Rojek

Acknowledgments

Szymon Nosewicz

Institute of Fundamental Technological Research
Polish Academy of Sciences

Abstract

The proposed doctoral dissertation presents a numerical and experimental analysis of manufacturing of new materials by powder metallurgy techniques. The scope of the thesis includes three main parts:

- formulation of an original numerical model of powder metallurgy,

- simulations of hot pressing for different combinations of process parameters,

- verification of the numerical model based on own experimental results.

The main part of the doctoral dissertation is dedicated to the theoretical and numerical investigations. An original numerical model of a powder metallurgy process has been formulated and implemented within the discrete element framework. The proposed model allows to study the motion (shrinkage and rearrangement) of powder particles during compaction and sintering stage and takes into account the growth of cohesive necks. In order to verify, calibrate and validate the numerical model, several simulations of hot pressing and sintering process have been performed. Numerical results have shown the correct representation of the density, shrinkage and densification rate of sintered specimens for different combination of process parameters. Validation of numerical model has been brought by performance of own experimental studies, which refers to manufacture the intermetallic NiAl, ceramic Al_2O_3 and NiAl-Al_2O_3 composite specimens and characterization of its mechanical and microstructural properties. Further numerical studies have comprised evaluation of micro- and macroscopic stresses during and after powder metallurgy process.

The results presented in this thesis have shown that the developed original discrete element model is an effective and suitable tool to analysis phenomenon occurring during the powder metallurgy process. Numerical model allows to study the material mechanism both at microscopic (such as a rearrangement and interaction of powder particles) and macroscopic scale (such as shrinkage, material densification or macroscopic stress). Presented results allow to the conclude that the new discrete element model can be applied to development and optimization of powder metallurgy processes.

Szymon Nosewicz

Instytut Podstawowych Problemów Techniki
Polskiej Akademii Nauk

Abstrakt

Niniejsza rozprawa doktorska przedstawia numeryczną oraz doświadczalną analizę procesu wytwarzania materiałów technikami metalurgii proszków. Zakres pracy badawczej obejmuje trzy główne punkty:

- opracowanie oryginalnego modelu procesów metalurgii proszków,

- symulacje jednoosiowego prasowania na gorąco przy różnych kombinacjach parametrów procesu,

- weryfikację modelu numerycznego za pomocą własnych badań doświadczalnych.

Główną częścią rozprawy są badania o charakterze teoretycznym i numerycznym. W ramach pracy doktorskiej został opracowany oraz zaimplementowany oryginalny model elementów dyskretnych. W celu weryfikacji, kalibracji oraz walidacji modelu numerycznego przeprowadzono szereg symulacji numerycznych. Wyniki z symulacji wskazują na prawidłowe działanie modelu, poprawne odwzorowanie prędkości zagęszczania i skurczu . Walidacja modelu numerycznego została przeprowadzona za pomocą własnych badań eksperymentalnych, które polegały na wytworzeniu szeregu próbek intermetalicznych NiAl, ceramicznych Al_2O_3 oraz kompozytowych $NiAl/Al_2O_3$ wraz z charakteryzacją właściwości mechanicznych i mikrostrukturalnych. Dalsze badania numeryczne dotyczyły analizy naprężeń generowanych w czasie procesu spiekania oraz naprężeń resztkowych po procesie wytwarzania.

Wyniki zawarte w niniejszej rozprawie doktorskiej pokazują, że opracowany w ramach metody elementów dyskretnych model jest efektywnym narzędziem do modelowania procesu metalurgii proszków. Pozwala badać mechanizmy procesu na poziomie zarówno mikro- (przegrupowanie i oddziaływanie ziaren w trakcie prasowania i spiekania) jak i makroskopowym (skurcz, zagęszczanie materiału oraz naprężenia makroskopowe). Na tej podstawie można stwierdzić, że przedstawiony model może być wykorzystywany do projektowania i optymalizacji procesów metalurgii proszków.

Symbols and abbreviations

The following list provides the most frequently used symbols and abbreviations:

a	–	radius of the interparticle boundary (cohesive neck)
a_0	–	initial particle boundary radius
a_{max}	–	maximum value of radius of the interparticle boundary at the equilibrium state
A_{s}	–	surface (solid-vapor) interface area
A_{gb}	–	grain boundary (solid-solid) interface area, cross-sectional area of cohesive neck
b	–	Burgers vector
c	–	constant of the Roberts and Garboczi model
c_{n}	–	viscosity (damping) coefficient
C	–	concentration of material (amount of substance per unit volume)
C_{a}	–	fraction of lattice sites occupied by the atoms
C_{cr}	–	critical damping for the system of two rigid bodies
d_{ij}	–	distance between the particle centres
d^{avg}	–	average Feret diameter
d_{br}	–	specimen diameter in the Brazilian test
d_{sp}	–	specimen diameter in the ultrasonic test
d_{p}	–	particle diameter
D	–	lattice diffusion coefficient
D_0	–	pre-exponential factor of the lattice diffusion
D_0'	–	pre-exponential factor of diffusion
$D_{0\mathrm{gb}}$	–	pre-exponential factor of the grain boundary diffusion
D_{a}	–	atomic self diffusion coefficient

D_{eff}	–	effective grain boundary diffusion coefficient
D_{gb}	–	grain boundary diffusion coefficient
D_{m}	–	domain size
D_{s}	–	surface diffusion coefficient
e	–	strain energy function
E	–	Young's modulus of a sintered material
$\overline{E}$	–	effective Young's modulus
E_0	–	Young's modulus of a fully dense material
f	–	correlation factor
$\mathbf{F}_i$, F	–	resultant force
$\mathbf{F}_{ij}^{\text{c}}$	–	contact force between discrete elements i and j
$(\mathbf{F}_{\text{n}})_{ij}$, F_{n}	–	normal contact force
F_{n}^{d}	–	viscous (damping) component of the normal contact force
F_{n}^{e}	–	elastic component of the normal contact force
$F_{\text{n}}^{\text{sint}}$	–	sintering driving force
$F_{\text{teor}}^{\text{sint}}$	–	theoretical sintering force
F_{n}^{T}	–	thermal component of the normal contact force
F_{n}^{v}	–	viscous sintering component of the normal force (viscous force)
$(\mathbf{F}_{\text{T}})_{ij}$, F_{T}	–	tangential contact force of discrete element
$\mathbf{F}_i^{\text{ext}}$	–	external load applied to the i-th discrete element
G	–	shear modulus
ΔG_{gb}	–	grain boundary Gibbs free energy
ΔG_{s}	–	surface Gibbs free energy
ΔG_{T}	–	total Gibbs free energy
ΔG_{v}	–	volume Gibbs free energy
h_{sp}	–	specimen height in the ultrasonic test
h_{br}	–	specimen height in the Brazilian test
H	–	specimen height in the numerical model
H_0	–	initial specimen height in the numerical model
ΔH	–	enthalpy of activation of the bulk (lattice) diffusion
ΔH_{gb}	–	activation enthalpy of the grain boundary diffusion
ΔH_{s}	–	activation enthalpy of the surface diffusion
j_{gb}	–	grain boundary atomic flux
J^{d}	–	diffusion flux
$J_{i,j}$	–	moment of inertia
k_{B}	–	Boltzmann constant
k_{n}	–	normal contact stiffness

$k_\mathrm{n}^\mathrm{eff}$	–	effective normal stiffness
k_T	–	tangential contact stiffness
ΔL	–	length change
L_0	–	initial length
$\mathbf{L^c}$	–	branch vector
L_{ii}	–	diffusion transport coefficient
L_u	–	specimen thickness in the ultrasonic test
m	–	particle mass
m'	–	scaled particle mass
m_a	–	atomic mass
m_s	–	mass of the dry specimen
m_n	–	mass of the specimen saturated with a well penetrating liquid
m_w	–	weight of the liquid saturated specimen suspended in the fluid
n_i^c	–	number of elements being in contact with the i-th discrete element
N_a	–	number of atoms in the unit cell
N_c	–	number of contacts in the representative volume element
p	–	external pressure
R	–	gas constant
$R_{0x},\ R_{0y}$	–	initial radii of geometrical model of the numerical specimen in the x and y direction
$R_x,\ R_y$	–	bulk radii of the geometrical model of the numerical specimen in the x and y direction
P_f	–	maximum applied tensile force
q	–	constant of the Ryshkewitch model
r	–	particle radius
$\overline{r}$	–	effective particle radius
$r(T)$	–	particle radius dependent on the temperature
r_at	–	atomic radius
s	–	constant of cohesive bond segments
$\mathbf{s}_{ij}^c$	–	vector connecting particle centres with contact points
ΔS	–	diffusion entropy
t	–	time
Δt	–	time increment (time step)
Δt_cr	–	critical time step
Δt_{1-2}	–	time difference between the first and second multiple ultrasonic echoes

t_0 – time of sintering activation
t_{end} – time of sintering end
t_{rel} – transition time
t_{s} – sintering time
T – temperature
ΔT – temperature increment
$\mathbf{T}_i$ – resultant moment about the central axes
$\mathbf{T}_i^{\text{ext}}$ – external moment applied to the i-th element
T_{m} – melting temperature
T_{s} – sintering temperature
$\mathbf{u}_i, u$ – displacement of a discrete element
$\dot{\mathbf{u}}_i, \dot{u}$ – velocity of a discrete element
u_{rn}^{e} – elastic part of the normal relative displacement
u_{rn}^{T} – thermal part of the normal relative displacement
u_{rn}^0 – initial penetration of two particles
u_{rT} – relative tangential displacement
$\mathbf{v}_{\text{r}}$ – relative velocity between two discrete elements
v_{rn} – normal relative velocity
v_{rn}^{e} – elastic part of the normal relative velocity
v_{rn}^{v} – viscous part of the normal relative velocity
v_{rn}^{T} – thermal part of the normal relative velocity
v_{rT} – relative tangential velocity
V – bulk volume
V_0 – initial volume
ΔV – change of volume
V_{L} – velocity of a longitudinal wave
V_{p} – discrete element volume
V_{RVE} – volume of a representative volume element
V_{T} – velocity of a shear wave
V_{u} – volume of a unit cell
V_{uw} – ultrasonic wave velocity
$\mathbf{x}_{\mathbf{p}}^{\mathbf{(i)}}$ – centroid of a particle
Z – coordination number
α – linear coefficient of thermal expansion
α_m – mass scaling factor
β – safety factor related to the critical time step
γ_{s} – surface (solid-vapour) energy
γ_{gb} – grain boundary (solid-solid) energy

δ	–	width of the grain boundary
ϵ	–	linear strain
ϵ_{v}	–	volumetric strain
ζ, ζ'	–	coefficients ensuring gradual change of sintering parameters
η	–	sintering viscosity coefficient
η_{∞}	–	sintering viscosity coefficient in the Maxwell element before sintering
η_{teor}	–	theoretical sintering viscosity coefficient
λ	–	lattice parameter
μ	–	chemical potential
ν	–	Poisson's ratio of a sintered material
ν_0	–	Poisson's ratio of a fully dense material
ν_1	–	constant of the Roberts and Garboczi model
ν_{D}	–	Debye frequency
ξ	–	fraction of the critical damping (damping ratio)
θ	–	porosity of a sintered material
ρ	–	bulk density
$\overline{\rho}$	–	average density
$\overline{\rho}_0, \overline{\rho}_1$	–	constants of the Roberts and Garboczi model
ρ_{f}	–	density of the fluid at the measurement temperature
ρ_{rel}	–	relative density
$\dot{\rho}_{\mathrm{rel}}$	–	densification rate
ρ_{theo}	–	theoretical density
$\rho_{\mathrm{theo}}(T)$	–	temperature-dependent theoretical density
σ	–	total average microscopic stress in the cross-section area
$\overline{\sigma}$	–	total macroscopic stress in the representative volume element
σ_{n}	–	local normal stress
σ^{sint}	–	microscopic stress induced in the cross section area by the sintering driving force
$\overline{\sigma}^{\mathbf{sint}}$	–	macroscopic stress induced by the sintering driving force
σ^{v}	–	microscopic stress induced in the cross-section area in the viscoelastic Maxwell element
$\overline{\sigma}^{\mathbf{ev}}$	–	macroscopic stress induced in the viscoelastic Maxwell element
σ_0	–	maximum strength for a full dense material
σ_{BTS}	–	tensile strength in a Brazilian test specimen
σ_{mod}	–	strength for a given relative density
$\boldsymbol{\sigma_{\mathbf{P}}}$	–	total average stress in a particle

τ_{Mr}	–	Maxwell relaxation time
$\tau_{\omega_{\max}}$	–	critical time step resulting from undamped vibrations
$\phi_x,\ \phi_y,\ \phi_z$	–	material shrinkage in x, y, z direction
ϕ_{V}	–	volumetric shrinkage
$\varphi,\ \varphi'$	–	coefficients related to transition time
Ψ	–	dihedral angle
$\boldsymbol{\omega}$	–	angular velocity
$\omega_{\max}$	–	angular eigenfrequency of the particle system
Ω	–	atomic volume

Contents

1

Introduction

1.1 Background and motivation

Powder metallurgy is a technology commonly used for manufacturing metal, ceramic or composite materials applicable in many industrial branches. For ceramic materials, powder metallurgy is the most widely used production process, however it is also a popular metal forming technology used to produce dense and precision components [1]. The ability to use powder metallurgy to mass produce reliable precision parts consistently at a cheap rate is very attractive, for example to the automotive industry (Fig. 1.1). Powder metallurgy is an energy saving, green technology offering improved performance and greater design flexibility compared with traditional manufacturing methods such as casting, extrusion, forging, stamping and machining. The automotive industry has accepted powder metallurgy technology, with the result that over 70% of its production worldwide is aimed at the automobile manufacturing sector [2].

Figure 1.1. Images of valve system parts manufactured by powder metallurgy technique (www.fine-sinter.com).

From the technological point a view, powder metallurgy is a process consisting of mixing granular materials, compacting into a desired form, heating and sintering the compressed material in a controlled atmosphere, and finally, cooling to room temperature. There are several techniques of powder metallurgy. Pressure-assisted sintering, in which powder compacting and sintering occur simultaneously, is one of these techniques, which recently has become most common [3]. In the case when the pressure is applied uniaxially, it is referred to as *hot pressing*. The process without additional pressure is called *free sintering*.

Sintering is the most important stage of powder metallurgy process. It involves consolidation of loose or weakly bonded powders at elevated temperatures, below the melting temperature. In some cases, during sintering of multicomponent systems, the melting point of one of the components can be lower than the sintering temperature. Then we have liquid-state sintering. Yet, in many systems, especially for pure compounds, sintering does not involve the formation of any liquid, and it is referred to as *solid-state sintering*. Solid-state sintering is a subject of investigation in the present work.

During sintering, granular material is converted into a polycrystalline solid body (Fig. 1.2). The final microstructure is a result of evolutionary changes due to particle compaction and rearrangement, formation and growth of diffusion bonds, shrinkage of the bulk material, grain growth, gradual reduction and elimination of porosity. These processes, in turn, are result of processes of diffusion and mass transport occurring at atomistic scale.

a)   b)
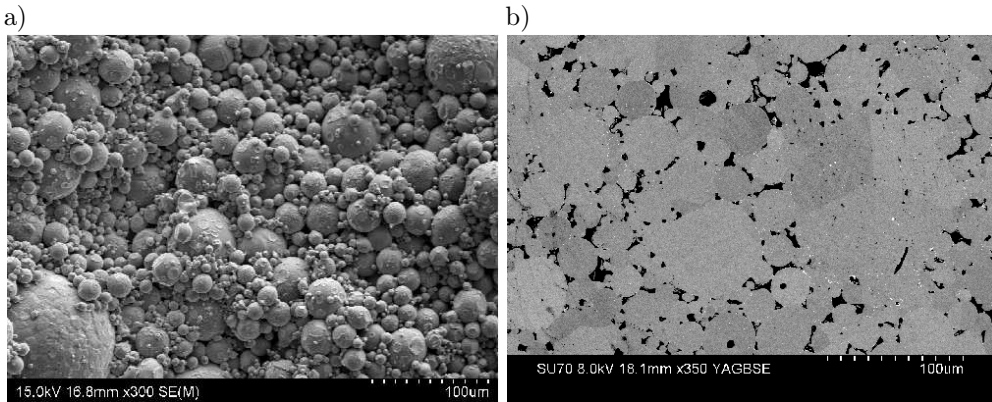
Figure 1.2. Structural change of the intermetallic NiAl material during sintering: a) morphology of the powder, b) microstructure of the sintered material.

Great progress in technology of powder metallurgy techniques enables permanent development of modern materials, such as composites – materials formed from two (or more) components (e.g., metallic, intermetallic or ceramic ones) with different physical and chemical properties, which together give different and usually improved characteristics with respect to individual components. Composite materials with a metal matrix are produced by casting and powder metallurgy methods [4]. In this work, the attention will be focused on the NiAl-Al$_2$O$_3$ composite belonging to a class of intermetallic-matrix composites reinforced with ceramics. This class of composites combine advantageous properties of intermetallic phases (high specific strength, low density, heat resistance, high melting point) and advantages of ceramics (such as wear resistance). Intermetallic-ceramic composites can be widely applied, instead of steel or metal alloys, in aerospace and automobile industries for elements working in conditions of intense friction (brake discs, clutches, cranes, valves) and treated with the rapidly changing temperatures (nozzles, combustion chambers, engine guards, exhaust systems).

Due to increasing significance of powder metallurgy, its analysis has become a major task in material manufacturing engineer's wish list. The current state of knowledge points to the necessity of research towards better understanding of relations between manufacturing process parameters and final material properties. Experimental studies of the manufacturing process have a number of physical limitations associated with inability to test the powder during the process. Therefore, importance given in material engineering to numerical modeling, which complements experimental research, is justified. A relatively short time of calculation, possibility of numerous tests at low costs, and an accurate prediction of real behaviour leads to a more and more frequent use of numerical methods reducing amount of experimental studies.

Modeling of powder metallurgy process is quite a new and challenging research task. The quality and final shape of sintered components are affected by many variables, processing parameters (temperature, pressure, etc.) and material properties (powder size, creep and diffusion constants, etc.). An efficient and effective modeling of powder metallurgy and sintering processes should allows to analyze accurately manufacturing process and evolution of material during the process. Precise numerical representation of powder metallurgy gives possibility to optimize the process by selecting appropriate sintering process parameters (temperature, pressure, time) and predict properties of sintered material, such as density, porosity as well as mechanical properties. Moreover, the risk of cracking of the material during cooling, due to the presence of significant residual stresses, can be effectively minimized by results of numerical simulations.

Numerical modelling can be a promising tool to study the complicated process of powder metallurgy, nevertheless choosing the appropriate method seems to be a fundamental issue.

1.2 Modeling of sintering: state of the art review

Sintering of granular material is a very complex process, affected by many factors and therefore it is difficult for modeling. There are different approaches to modeling of sintering, including phenomenological and mechanistic approaches, continuous and discrete formulations, modeling at macro, micro and atomistic levels, and multiscale modeling combining models at different levels. Different sintering models are reviewed in [5–8]. Here, it will be discussed the state of the art in modeling of sintering classifying the models into the following groups:

- continuum macroscopic models,
- micromechanical models,
- atomistic models,
- multiscale models.

Discrete element models of sintering, the topic of main interest in this thesis, will be reviewed separately.

Continuum macroscopic models

In the continuum macroscopic approach, the porous powder under compaction is treated as a continuous medium at the macro-scale. Its deformation behaviour is described by constitutive equations based on a modified plasticity theory of solids. The constitutive model for densification of metal powder compacts under high temperature generally incorporates the mechanisms of power-law creep, diffusional creep, and grain growth. Continuum models of sintering can be classified into two types:

- continuum phenomenological models,
- continuum micromechanics-based models.

Continuum phenomenological models

The macroscopic behaviour of sintered materials is a result of a complex combination of elastic, viscous, plastic and thermal deformation [9, 10]. Phenomenological sintering models generally incorporate mechanisms of thermal

and elastic deformation along with the viscous creep flow [10–13]. In the phenomenological modeling, constitutive model parameters are obtained by fitting experimental data. In the modeling of sintering the dependence of the viscosities and the sintering potential on the temperature must be known. A direct measuring of the viscosities has been carried out by several research groups [13, 14]. Conventional constitutive models of sintering are expressed in terms of the evolution of two scalar state variables, density and particle size. They do not provide any information about how changes in initial particle size distributions or agglomeration influence the constitutive response.

Among the well-known phenomenological sintering models there are models presented by Abouaf et al. [15], Duva et al. [16], Cocks [17], McMeeking [18], and Ponte [19]. In particular, the model of Abouaf et al. [15] is the most general empirical model, it requires the density function to be determined through hydrostatic and uniaxial compression experiments. Phenomenological models of sintering are presented in [13]. Phenomenological approaches are reviewed by Olevsky [20], Exner and Kraft [6], Cocks [21] and German [22, 23].

Continuum micromechanics-based models

Structural theories for the particle level can be used to determine mechanical properties of a unique fictitious continuous material that represents a real heterogeneous material. Different densification mechanisms (powder creep, diffusion, etc.) are analysed in the view of a single particle and its surrounding (contact). The rate equation of densification is obtained. On the basis of the densification rate equation, density and final shape as well as their variation in time, temperature and pressure can be predicted. Continuum constitutive sintering models derived from micromechanical ideas were developed by Scherer [24], Abouaf et al. [15], Jagota and Dawson [25], McMeeking and Kuhn [26], Svoboda et al. [27, 28], Riedel et al. [29–32], to name the few. A micro-mechanical based continuum mechanics model for finite element analysis is presented in [33].

Micromechanical models

Micromechanical models consider microstructural changes during sintering. These models fall into two basic types:

- micromechanical models based on topological structure evolution,
- particle models.

Micromechanical models based on topological structure evolution

In this approach, model topologies approximating initial microstructure are constructed. Then, the evolution of the discretized structure is simulated. The simulation methods can be divided into:

- probabilistic methods,

- deterministic methods.

Probabilistic methods consist in Monte Carlo simulations applied to a physical model including the effects responsible for the evolution of the structure such as variable surface diffusivity, grain boundary diffusivity, and grain boundary mobility [34–37]. Monte Carlo methods can be used with various principles such as maximum entropy and dihedral angle equilibrium. The application of the Monte Carlo method for grain growth simulations originates from Potts [38] model for magnetic domain evolution. Anderson et al. [35] were the first to introduce the Potts model into the simulations of grain growth. The Monte Carlo method was applied to sintering process simulation in [34, 39]. These simulations reproduce essential features of individual processes with relative success. They are especially suitable for the simulation of the late stage of sintering. Results of Monte Carlo simulation of microstructure evolution during sintering are shown in Fig. 1.3.
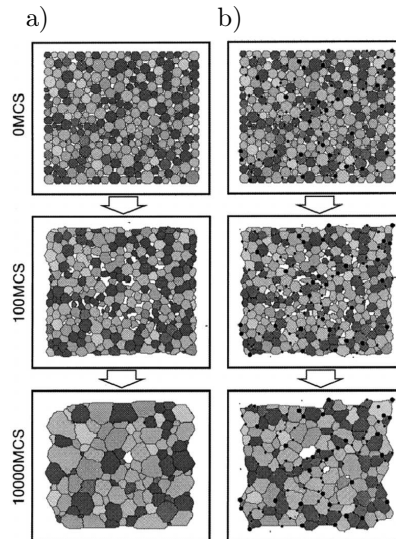
Figure 1.3. Monte Carlo simulation of microstructure evolution during sintering [34].

Deterministic methods of the microstructure evolution use analytical equations of motion to calculate new grain boundary locations. Pan, Cocks and their co-workers [40, 41] developed a finite element formulation to model microstructural evolution of materials at elevated temperatures. A finite element scheme was used to study the sintering of powder compacts [42].

Particle models

Discrete models of sintering considered an interaction of particles and the local problems of particle necks. Sintering is treated as the collective result of thermally activated adhesion processes which produce the growth of contacts between particles. Sintering models at the particle scale have been used in the classical works on sintering. Frenkel [43] and Kuczynski [44] studied mechanisms of the neck growth and shrinkage for the early sintering stages (particle bonding) using a two-sphere model. The two-particle model has been extrapolated for the intermediate shrinkage state by Kingery and Berg [45]. Coble [46] developed a cylindrical pore model, a spherical pore model for late sintering stages was developed by MacKenzie and Shuttleworth [47]. More sophisticated models taking superpositions of various sintering mechanisms into account were developed by Ashby [48], Arzt [49], and Exner and Arzt [50].

Atomistic models

Nowadays, computational techniques allow to model the behaviour of solid materials at the atomistic level. Molecular dynamics (MD) is a method providing a detailed picture of the evolution of atomic positions and velocities as a function of time. The atomic interactions are characterised by the inter-atomic potentials, hence the chemical composition of the material is explicit in the model. The thermodynamic and kinetic properties of the material can be extracted from the results of simulation. Direct molecular dynamic simulation of particle sintering is limited to a small number of nanosized particles due to a large demand for computing power (Fig. 1.4).

Such simulations have been performed by a number of authors, e.g. [34, 51–54]. Molecular dynamics techniques were used to simulate Cu and Au nanoparticle arrays at different temperatures to study surface energies, grain boundary mobility and sintering by Zeng et al. [54]. Sintering process and subsequent martensitic transformation in sintered Fe-Ni nanoparticles were studied using MD techniques by Kadau et al. [55].
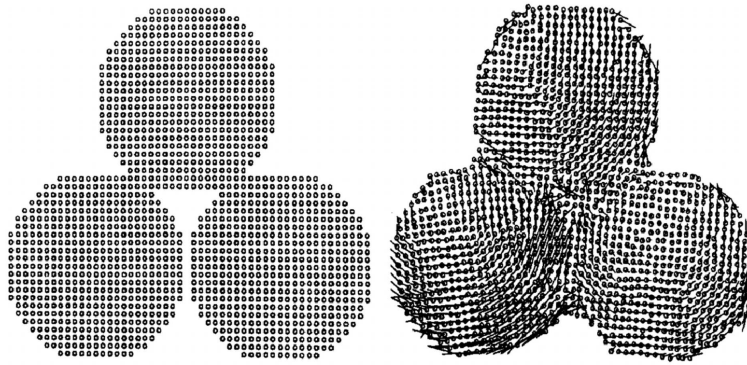
Figure 1.4. Molecular dynamics simulation of particle sintering [54].

Multiscale models

Multiscale modeling of sintering integrates sintering models at the atomistic, particle and continuum levels [8]. The idea of multiscale modeling is presented in Fig. 1.5. The review of multiscale studies of sintering is provided in [56].
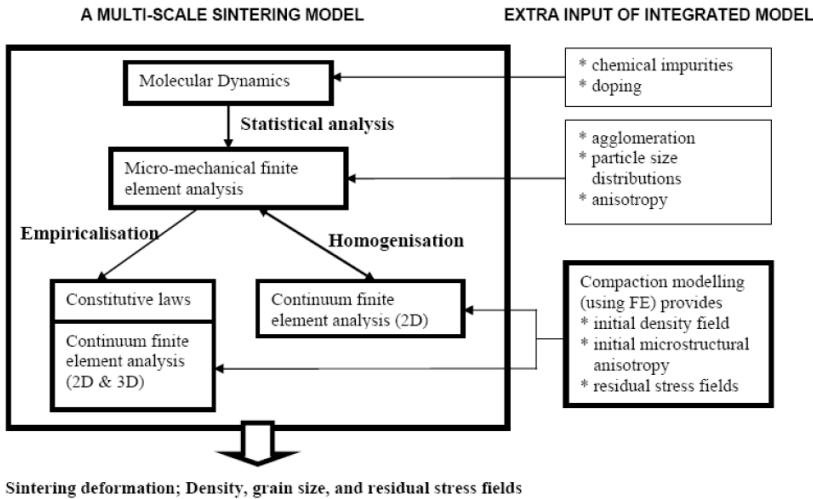
Figure 1.5. Flowchart for the integration of sintering models at atomistic, particle and continuum levels [8].

Discrete element modeling of powder sintering

In numerical modeling of engineering problems, some problems can be represented by an adequate model using a finite number of well-defined components [57]. The behaviour of such components is either well known or can be independently treated mathematically. The global behaviour of the problem can be obtained through well-defined relations between the individual components (elements). Such systems are termed discrete. Discrete models take into account the discontinuities, defects, molecular structure of the material and its particle size. Discrete modeling have been developed in response to the deficiency of a continuous model associated with the lack of ability to consider all kind of defects in the material, and the difficulties in formulating constitutive equations of those models.

A growing ability of computational techniques has widened the range of possibilities to employ particle sintering models. Sintering models have been implemented within the discrete element method which allows to model interaction of very large collections of particles [58–75]. Parhami and McMeeking [58] have implemented a particle sintering model derived by Coble [46] in the quasi-static formulation of the lattice type discrete element method to study the free and pressure-assisted sintering. The concepts of Parhami and McMeeking have been incorporated in the dynamic formulation of the discrete element method by Martin et al. [59] and used for investigation of free sintering of metallic powders. A similar model has been applied by Henrich et al. [64] to simulate the free and pressure-assisted solid-state sintering of powders with special attention to the influence of particle rearrangement during sintering. The study of sintered particle rearrangement has been also performed by Martin et al. [74] with special application of Non Smooth Discrete Element Method. The microstructure evolution and force distribution during solid-state sintering were studied by [75] at the particle length scale for a planar layer system of copper particles. The effect of particle size distributions on sintering has been studied by Wonisch et al. [65], who proved that particle distribution in the specimen has a significant effect on the strain rates and viscosity during sintering. In [66] discrete element modeling was employed to determine anisotropic constitutive parameters of sintered material as a function of density. Anisotropy phenomena have been also studied by Rasp et al. [67] and Martin [68] by a discrete simulation of sintering of thin ceramic stripes constrained by a substrate. Modeling results confirmed that the occurrence of anisotropy develops along the thickness of the substrate. Furthermore, collective particle behaviour such as interparticle coordination and particle rearrangement have been investigated by coupling *in situ*

X-ray microtomography and discrete element simulation in papers [69]. The analysis of powder rearrangement allowed Martin [70] to study the evolution of a crack both in a non-constrained and constrained sintering (Fig. 1.6).
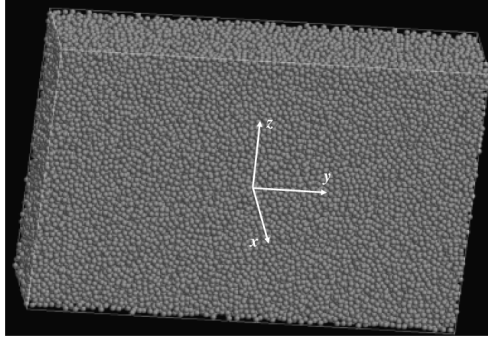
Figure 1.6. Discrete element simulation of alumina powder sintering [70].

In the papers [58, 61, 64, 65], both the free and pressure-assisted sintering have been modeled, yet a special procedure had to be introduced to consider the effect of additional loading during pressure-assisted sintering. The sintering models presented in all the above are not capable to support additional external loading. Therefore the problem of stress-assisted sintering is decomposed into two problems, that of the free sintering and that of the stress induced deformation. Macroscopic strains induced by external stresses are calculated and particle displacements due to these strains are added to the displacements obtained for free sintering.

Generally, discrete element models of sintering process considered simulations of one-phase powder, however two-phase powder sintering models have been also employed recently. Schneider et al. [71, 72] and Liu et al. [76] have modeled the composite anode and cathode of solid oxide fuel cells (SOFC) as the sintered mixtures of electrolyte and electrocatalyst particles. Olmos et al. [63] have analysed the sintering behaviour of metal powder mixed with ceramic inclusions. In this work discrete element modeling of copper-alumina free sintering was supported by experiments.

1.3 Objectives and scope of the thesis

The main scientific aim of the proposed thesis is the numerical analysis of powder metallurgy and sintering process employed in manufacturing of granular materials. The proposed work is focused at the three specific objectives:

- formulation and development of an original discrete element model of powder metallurgy,

- experimental studies of a powder metallurgy process,

- verification and validation of the numerical model based on own experimental results.

The presented research objectives involving numerical and experimental analysis are included in the scope of the thesis, detailed as follows:

1. **Numerical modeling of powder metallurgy process within the framework of discrete element method:**

   (a) **Formulation of the powder metallurgy model**. The original powder metallurgy model will be formulated and implemented within the framework of the discrete element method. The presented studies will involve the formulation of the model for the compaction and cooling stage, and the new formulation of the sintering model. Discrete element model will include the viscous, elastic, cohesive and thermal interaction of particles.

   (b) **Numerical simulation of powder metallurgy process**. The numerical model will be verified by simple tests of two particle sintering. The performance of the new model will be compared with that of the standard viscous model in the area of the correspondence and efficiency. Numerical model will be calibrated and validated by the own experimental results of pure NiAl, pure Al_2O_3 and NiAl-Al_2O_3 relative density. Material phenomenon occurring during simulations of powder processing, such as shrinkage of the material, decrease of porosity, interaction between the particles and rearrangement of particles will be analyzed.

   (c) **Numerical analysis of stresses**. The stresses in the NiAl-Al_2O_3 composite will be determined in the two scales: micro- and macroscopic. Microscopic stress will be analyzed in the two places subject to cracking: the cohesive neck and the whole body of particle. Macroscopic stress will be calculated by the application of averaging methods.

2. **Experimental investigations of powder metallurgy process:**

   (a) **Fabrication of powder metallurgy specimens**. Pure NiAl, pure Al_2O_3 and NiAl-Al_2O_3 composite specimens will be manufactured by hot pressing procedure at different combinations of sintering process parameters: temperature, pressure and time. Density measurements will provide data for the density–time curves for a specific temperature

and pressure. The experimental results will be used in the calibration and validation process of numerical model.

(b) **Characterization of sintered specimens**. Manufactured specimens will be characterized to determine the mechanical properties and study the microstructure of materials. Mechanical analysis consists of non-destructive ultrasonic tests and indirect tension (Brazilian type) test. The elastic constants and tensile strength will be assessed in the relation to the microstructural features of materials, e.g., porosity or shape of pores. Characterization will provide data for the optimization process of powder metallurgy of studied materials and will assess the influence of the sintering process parameters on the material properties.

The execution of the tasks formulated in the work will allow to verify the following thesis:

The original discrete element model of powder metallurgy process, due to its theoretical and numerical character, is an efficient and suitable tool to represent correctly the macroscopic and microscopic effects of manufacture process of novel composite materials, such as shrinkage, change of density and evolution of stress.

1.4 Outline of the thesis

Presented thesis has been divided and reported in seven sections and three appendices. The outline of the thesis is as follows:

Section 1 presents the background and practical motivation of the research work. The state of the art in numerical modeling of powder metallurgy is reviewed. The objectives and the thesis are formulated.

Section 2 introduces the basic information of the main stage of powder metallurgy – sintering process. The driving forces of sintering, related to the minimisation of the free energy of powder particles, applied pressure and sometimes chemical reaction, are described. Mechanisms of mass transport, with the diffusion playing an important role in sintering, are presented.

Section 3 presents experimental investigation of powder metallurgy processes and manufactured materials. Manufacturing of the intermetallic NiAl, ceramic Al_2O_3 and composite $NiAl-Al_2O_3$ specimens by hot pressing at different combinations of sintering process parameters: temperature, pressure and time has been investigated. Experimental studies provided data on density evolution which were essential for the model calibration and validation. Microscopic observa-

tions allowed to see microstructure changes during the process. Furthermore mechanical properties (elastic moduli and tensile strength) of the manufactured materials have been determined.

Section 4 introduces the formulation of an original numerical model of powder technology process within the framework of the discrete element method. The model is aimed to model all the stages of the powder metallurgy process: powder compaction stage, heating, sintering, and cooling. Particle interaction at the stage of powder compaction and cooling is represented by the the Kelvin-Voigt element model. An original thermo-viscoelastic model is formulated for the sintering stage. The rheological scheme of this model employs the Maxwell element. A smoothing algorithm for the transition between different model types is proposed. Time integration of the equations of motion and constitutive equations is presented. Numerical stability of the time integration schemes is discussed. Furthermore, the proposed section presents the determination of the material parameters of the sintering model.

In Sec. 5 the numerical results of the simulation of powder metallurgy and sintering process are shown. The numerical model is verified by simple tests of sintering of two copper particle. Application of the model to simulation of the real powder metallurgy process of the pure NiAl, pure Al_2O_3 and NiAl-Al_2O_3 composite materials is presented. The model calibration and validation based on the own experimental results is shown. The influence of sintering process parameters on the sintering kinetics is analysed.

Finally, Sec. 6 presents the determination and analysis of the microscopic and macroscopic stress during and after the hot pressing process of the NiAl-Al_2O_3 composite. Evolution of macroscopic stresses and distribution of microscopic stresses in the necks and particle bodies is analysed.

Section 7 contains the summary of the research work presented in the thesis. Original elements are emphasized and possible continuation of the research is presented.

The three appendices present details on the following topics:

- Derivation of the model of the two-particle interaction during sintering.

- Estimation of material parameters of sintering model.

- Original algorithm of generation of a geometrical model of powder specimen.

Sintering

Introduction

Sintering is regarded as the most important stage in powder metallurgy process. Sintering can be defined as the thermal treatment of a powder (or compact) at a temperature below the melting point of the main constituent, for the purpose of increasing its strength by bonding together of the particles [77]. The obtained sintered body is characterized by significantly different form compared to the initial state. The evolution of sintered powder is governed by many factors at different scales. Due to the complexity of the process, the description of sintering phenomenon is a non-trivial task.

Presented section contains a short description of the basic mechanisms of sintering – driving forces of sintering, mass transport and evolution of material during sintering. The purpose of this section is to bring the essential data for understanding the process, formulation of the numerical model, interpretation of experimental results and numerical studies of powder metallurgy and sintering process.

2.1 Driving forces of sintering

Sintering of polycrystalline materials is rooted in the material evolution at the atomic scale. When the thermal energy of the system is high enough, atoms from high chemical potential sites move to low chemical potential regions, thus lowering the total free energy of the system, which can be expressed as:

$$\Delta G_{\mathrm{T}} = \Delta G_{\mathrm{v}} + \Delta G_{\mathrm{gb}} + \Delta G_{\mathrm{s}}, \tag{2.1}$$

where ΔG is the Gibbs free energy, and subscripts T, v, gb and s refer to total, volume, grain boundary and surface.

Sources that ensure the lowering of the free energy of the system are commonly referred to as *the driving forces for sintering* [3]. Three possible driving forces are the curvature of the particle surfaces, externally applied pressure and chemical reaction (Fig. 2.1).
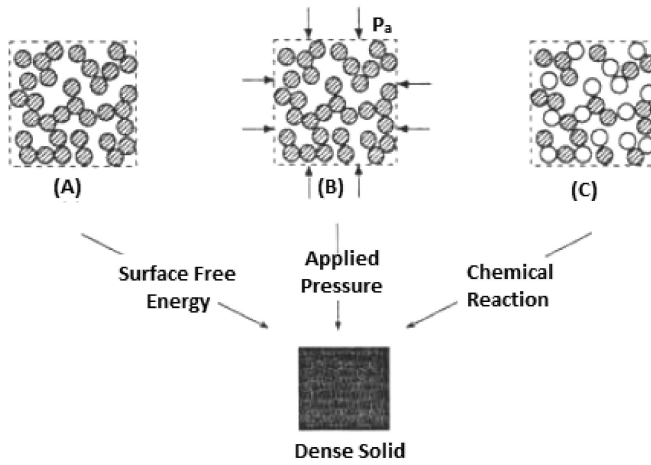
Figure 2.1. Schematic diagram illustrating three main driving forces of sintering: surface free energy, applied pressure, and chemical reaction [3].

Solid bonds formed between the particles during sintering can reduce the surface energy by removing free surfaces [78]. Furthermore, the reduction of the area of free surface of powder particles also occurs through spheroidization of pores and their elimination. The change of the free energy of the sintering body due to interparticle bonding can be expressed as:

$$\Delta G_{\mathrm{s}} = \gamma_{\mathrm{s}} \mathrm{d}A_{\mathrm{s}} + \gamma_{\mathrm{gb}} \mathrm{d}A_{\mathrm{gb}}, \qquad (2.2)$$

where γ is the interface energy, A is the interface area, $\mathrm{d}A$ is the change of the interface area. The subscripts s and gb denote the surface (solid-vapour) and the grain boundary interface (solid-solid) respectively.

Externally applied pressure normally provides a major contribution to the driving force when the pressure is applied over a significant part of the heating process as in the case of hot pressing and hot isostatic pressing [3]. Surface curvature also provides a contribution to the driving force, but for most practical situations it is normally a lot smaller than that provided by the external pressure.

Chemical reaction can be another way to provide a driving force for sintering. Sometimes the addition of a very small amount of the second material greatly increases the rate of sintering. Usually, this can be attributed to the formation of a phase with a much lower melting point in which the diffusion is much faster. Despite the advantage of this method, the chemical addition is hardly ever used deliberately to drive the densification process in advanced materials, because

microstructure control becomes extremely difficult when the chemical reaction occurs concurrently with sintering.

In the presented research investigation, the chemical reaction is neglected and the main driving force causing the material densification is applied pressure. Application of external loading affects an easier regrouping of powder particles at the compaction stage and an intensification of mass transport mechanism at the sintering stage.

2.2 Mass transport mechanism of sintering

Several material mechanism can be considered in the area of particle contacts. Some of them contribute to densification, others only change the shape of the particles. Generally more than one material transport mechanism contributes to the sintering and different mechanism dominate the process at different stages of the process or at different temperature regimes. There are several groups of mass transport mechanisms occurring during the sintering process: mechanisms of diffusion, viscous and plastic flow, evaporation or condensation of the vapours. Diffusion mechanisms occurring in the sintering process generally include surface diffusion, grain boundary diffusion and lattice diffusion (Fig. 2.2).
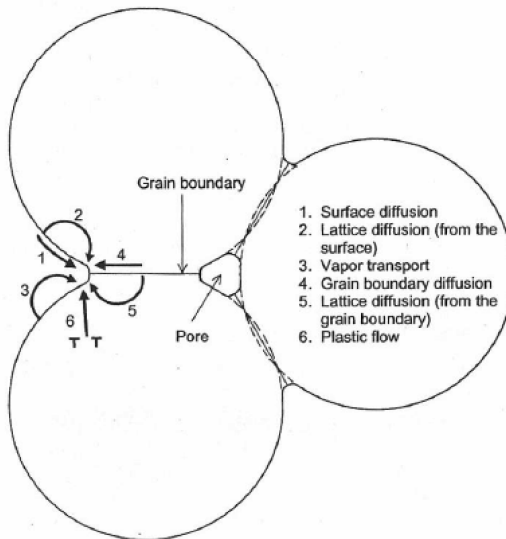
Figure 2.2. Material transport pathways to the neck area [3].

Surface diffusion occurs at temperatures above 0.3 of the material melting temperature. The movement of atoms in the surface characterized by a higher energy and increased mobility in comparison to the atoms located in inside the particles, is associated with the gradient of chemical potential dependent on the curvature of the surface. The result of surface diffusion is a change in the surface profile resulting in the coalescence and spheroidization of pores substantially without changing their volume.

The grain boundary diffusion is the dominant mechanism of mass transport during sintering in the temperatures ranging from 0.5 to 0.8 of the material melting temperature and in the case of particles of small size. Due to the fact that significant number of material defects are located at the grain boundaries area, it becomes a privileged way to atomic flow. The stress distribution at the grain boundary determines the occurrence of differences in concentration of vacancies in these areas.

Bulk (volume, lattice) diffusion occurs during sintering when the temperature is above 0.8 of the melting point. Depending on the structure of the neck area, there are two kinds of bulk diffusion mechanism. The first leads to the increase in the contact area between particles with a simultaneous approach of particles center, and the second does not involve a particle motion.

The participation of different diffusional mass transport in the sintering process depends on the temperature and particle size of the sintered powder. Ashby [48] provided a theoretical analysis of sintering with simultaneous mechanisms of mass transport involving the construction of sintering diagrams (Fig. 2.3).
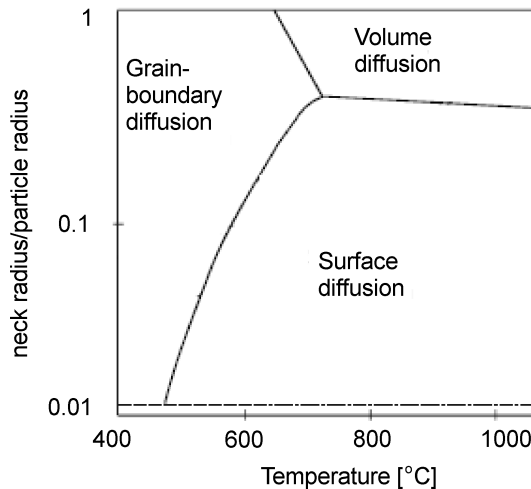
Figure 2.3. Neck size sintering diagram for copper spheres.

The diagram is divided into various fields, and within each field, a single mechanism is dominant, i.e., it contributes most to the neck growth for sintering of cooper with a radius of 57 µm [3]. Figure 2.3 is divided into three fields corresponding to surface, grain boundary and volume diffusion. Temperature determines the type of mass transport mechanism, however it is also the indicator of particular stage of sintering process.

2.3 Stages of sintering

The solid state sintering can be divided into three stages: initial, intermediate and final. There is no clear-cut distinction between the stages, but each stage can be described by its general characters, as shown in (Fig. 2.4).
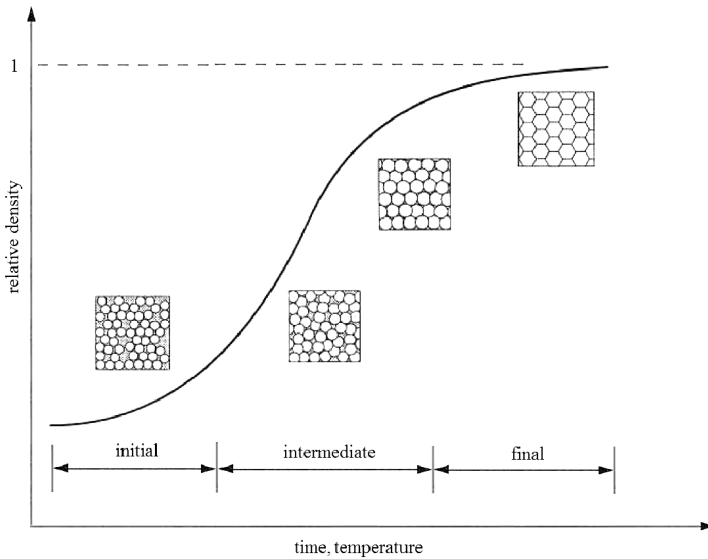
Figure 2.4. Schematic representation of stages of solid state sintering [79].

In *the initial stage*, in low temperatures, significant changes in the microstructure of the system do not occur. The main mechanism responsible for the mass transport at this stage of sintering is the surface diffusion. The density of the material does not increase dramatically at this particular stage; however, powder particles become partially rounded and cohesive connections between the particles start to form (Fig. 2.5).
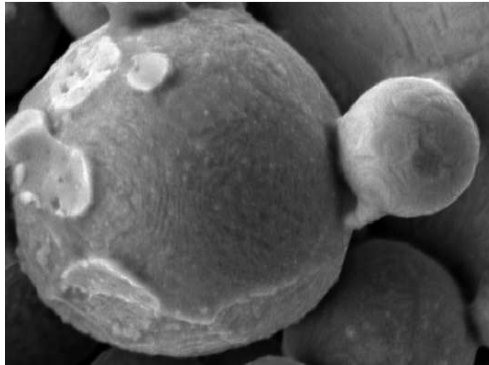
Figure 2.5. Cohesive neck of NiAl particle formed during sintering process.

Material shrinkage accompanied by an increase of the density and the grad-ual elimination of porosity activates in *the intermediate stage*. In microstructure an increase in the particle compaction and contacts between individual particles can be observed. Furthermore, grain growth starts. The mass transport mech-anism causing such a significant increase in the density of the material is the grain boundary diffusion. Material indicates the reduction of the number and size of pores. At this stage of sintering, microstructure compaction measured by changes in density, porosity and particle surface area, are the greatest and determine the properties of the sintered components.

The final stage of sintering is characterized by a significant reduction in the rate of particles compaction. Microstructural changes consist in the evolution of pores shape to be more spherical (Fig. 2.6). The final stage also refers to the iso-lation of pores located at the particle corners. It is also known as the coarsening involving the growth of the larger particles and the consumption of the smaller particles. The final microstructural effect of sintering is a polycrystalline body with almost zero porosity.
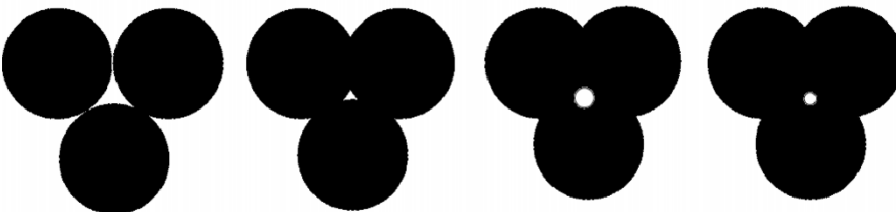
Figure 2.6. Schematic representation of pores shape evolution during solid state sintering.

Microscopic changes of the powder material have its results at the macroscopic scale. The spheroidization of particles, the formulation of diffusion bonds, particles rearrangement and particles compaction refer to an evolution of the main physical properties, such as a density, shrinkage, porosity or colour. While the physical properties are changed, the material indicates higher elastic properties, mechanical strength, hardness or wear resistance.

Summary

In the powder metallurgy, sintering is the main stage of material manufacturing process. Sintering involves the consolidation of loose or weakly bonded powders at elevated temperatures, close to the melting temperature with or without additional pressure. The cohesive connections between particles in the form of necks are formed and grow due to mass transport, with the surface and grain boundary diffusion being the most important mechanism of mass transport in sintering. Diffusion process is strictly related to the temperature influencing mobility of atoms. The driving force of sintering is minimisation of the free energy of the particles mainly due to the curvature of the particle surfaces and applied pressure. The stresses induced by sintering at the necks cause particle attraction, which results in material shrinkage and reduction and elimination of porosity. Microstructural changes can be controlled by a sintering process parameters (sintering temperature and time, applied pressure) during a manufacturing process. Selection of appropriate sintering conditions affects the material properties, such as density, porosity, shrinkage and hence mechanical strength and elastic constants.

3

Experimental investigation
of powder metallurgy process

Introduction

The present section provides a description of the experimental investigations of powder metallurgy process carried out in this work. The main purpose of the experimental studies has been to obtain the data for validation of the developed numerical model of sintering. Hot pressing of one-phase intermetallic NiAl and ceramic Al_2O_3 powders as well as of two-phase mixtures NiAl-Al_2O_3 has been investigated. The NiAl-Al_2O_3 composite was selected as a novel promising material. A number of tests have been carried out taking different combinations of sintering process parameters. Experimental studies have encompassed density measurements, determination of mechanical properties and microstructure observations. Density measurements for different sintering time produced the curves of density evolution which will be used as the main reference data for the model validation. The characterization of mechanical properties included nondestructive ultrasonic tests allowing the determination of the elastic constants of the material, and indirect tensile strength test (only for composite materials). Microstructural characterization was based on the study of distribution of particles, the analysis of the cohesive connections between individual particles and porosity studies. The results of the microstructure observations were analyzed in context of the densification, elastic properties and strength of obtained specimens. Characterization allowed to assess quality of manufactured materials. The following experimental results have been presented in detail in [80–82].

The powder metallurgy experiments and the part of microstructural studies were carried out in cooperation with the Department of Metal-Ceramic Composites and Joints at the Institute of Electronic Materials Technology (ITME) under tutorship of dr hab. inż. Katarzyna Pietrzak and dr inż. Marcin Chmielewski. The ultrasonic examination of manufactured specimens was carried out with the support of dr inż. Sławomir Mackiewicz from Department of Strength of Materials of IPPT PAN.

3.1 Materials specification and characterization

Intermetallic phases of the Ni-Al type belong to materials characterized by low density and advantageous properties such as a high melting temperature, high resistance to oxidation at high temperatures (to about 1200^oC), high value of the Young's modulus stable in an increased temperature, high mechanical fatigue, tensile and compressive strengths (also at high temperatures), and good frictional wear resistance [83–86]. This unparalleled combination of unique physicochemical and mechanical properties offers a wide range of application possibilities for these materials. They are widely used in the automobile, aerospace, metallurgical, chemical and power generation industries. Unfortunately, intermetallic compounds also manifest several drawbacks, i.e. brittleness and difficulties of mechanical processing at the room temperature, or susceptible to creep at the high temperatures. These disadvantageous properties restrict their application range.

The drawbacks (the brittleness and susceptible to creep) can be eliminated by reinforcement of the intermetallic phase with ceramics such as Al_2O_3. Aluminium oxide Al_2O_3 (alumina) is a well-known ceramic material characterized by low density, high stiffness and high melting temperature. Strong chemical bonds between the aluminium and oxygen atoms makes the aluminium oxide resistant to acids and to other chemical matters. Main properties of NiAl and Al_2O_3 are presented in the Table 3.1.

Table 3.1. Properties of intermetallic NiAl and ceramic α-Al_2O_3 materials [87–91].

Properties	NiAl	Al_2O_3
Density [g/cm^3]	5.91	3.97
Melting point [K]	1911	2345
Young's modulus [GPa]	188	416
Poisson's ratio	0.31	0.23
Flexural strength [MPa]	346	380
Hardness Vickers [kGmm^{-2}]	310	1900
Fracture toughness [MPa m^{-1}]	7.2	3.5
Coefficient of thermal expansion [10^{-6}K^{-1}]	11.5	7.4

Intermetallic based composites reinforced with ceramic particles belong to novel materials with a wide range of industrial applications. NiAl matrix composite reinforced with ceramic Al_2O_3 particles shows advantageous properties such as excellent mechanical and properties as well as high frictional wear resistance [87, 92–94]. This makes it suitable for elements working in conditions

of intense friction (brake discs, clutches, cranes, valves) and for parts subject to rapidly changing temperatures (nozzles, combustion chambers and exhaust systems).

Properties of composites can be tailored according to application requirements taking suitable phase composition and designing specific microstructure which can be produced by appropriate manufacturing process [95, 96]. The control of manufacturing process and understanding of microstructure evolution during this process is essential in optimization of intermetallic-ceramic composites. Due to the differences in the atomic structure and properties between intermetallics and ceramic materials, there are some difficulties in manufacturing of these composites, e.g. occurrence of significant thermal stresses leading to material cracking. Investigation of intermetallic-ceramic composite properties and manufacture process has become a major task of material science.

Manufacturing processes and properties of intermetallic NiAl composites with ceramic reinforcements have been discussed in several papers [87, 91, 97–105]. In most of the referred studies, hot pressing process was employed to obtain a fully dense composite material. Composite properties depend on various factors. It was shown in [98] that the phase composition of $NiAl/Al_2O_3$ composite has a crucial impact on the toughness enhancement. An influence of mechanical powder mixing on properties of $NiAl/Al_2O_3$ composite was studied in [87, 97]. The experiments have shown that the physical and mechanical properties such as bulk density, strength and hardness of the composite closely depend on the parameters of both the mixing and sintering processes. The increase in strength, in comparison to pure NiAl phase, was attributed to microstructural refinement observed in SEM images.

Different experimental methods have been used to determine mechanical properties of $NiAl/Al_2O_3$ composite. In [91, 99, 103], the Young's modulus, Poisson's ratio and strength parameters were determined by the bending strength test. A non-destructive method based on ultrasonic sound wave propagation measurements was employed to determine the elastic constants of an intermetallic composite in [100, 101]. Experimental data can be compared with theoretical predictions. In [105], the authors present theoretical nonlinear relations for the estimation of elastic constants of $NiAl/Al_2O_3$ composite material.

All the referred works report promising mechanical properties of NiAl matrix composites, however, there is still a lack of full understanding of dependence of the macroscopic composite properties on microstructure and evolution of this relationship during manufacturing process. Present studies of manufacturing of $NiAl/Al_2O_3$ may bring essential data for optimization of two-phase powder metallurgy process and apparent improve a composite properties.

3.2 Experimental procedure

Specimen manufacturing

Current study involves fabrication of three types of specimens: a nickel aluminide (NiAl), an aluminium oxide (Al_2O_3) and a NiAl-Al_2O_3 composite. The specimens were manufactured from intermetallic NiAl powder delivered by the Goodfellow Company and ceramic Al_2O_3 powder from NewMet Koch. Morphology of these powders is shown in Fig. 3.1.

a)   b)
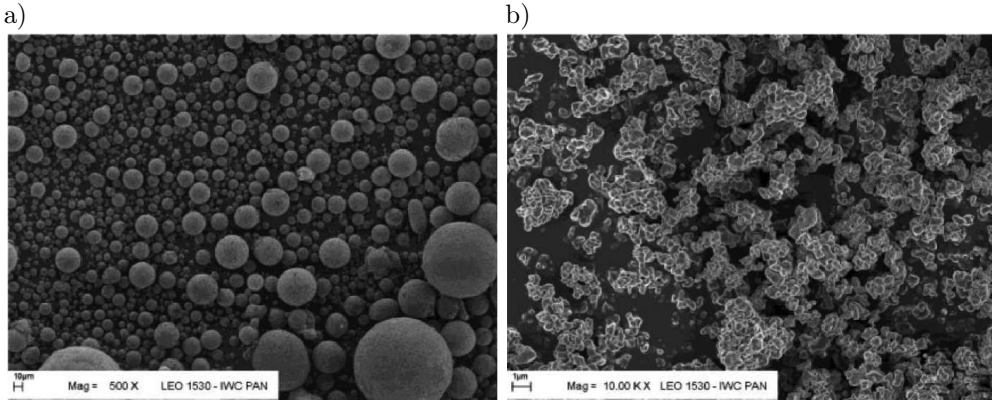
Figure 3.1. SEM images of the powders: a) NiAl, b) Al_2O_3.

The particle size of the starting powders was analyzed with the Clemex image analyzing system. The average Feret diameter $d_{NiAl}^{avg} = 9.71$ µm was estimated for the NiAl powder and $d_{Al_2O_3}^{avg} = 2.28$ µm for the Al_2O_3 powder. The particle size distributions of the intermetallic NiAl and ceramic Al_2O_3 powders are shown in Fig. 3.2.

a)   b)
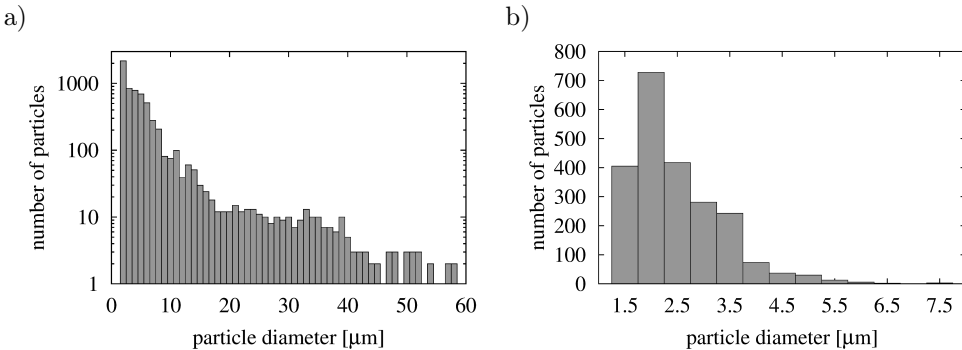
Figure 3.2. Particle size distribution of: a) intermetallic NiAl, b) ceramic Al_2O_3 powder.

The powder mixture prepared for technological experiments contained 20% volume fraction of Al_2O_3 and 80% of NiAl. This composition was taken expecting that properties of the composite will differ appreciably from those of pure NiAl, but its advantageous properties will be preserved.

The manufacturing process consisted of three main stages: powder mixing (only for composite material), powder compaction and sintering. The purpose of powder mixing was to get uniform distribution of Al_2O_3 ceramic phase in NiAl intermetallic matrix. Non-uniform distribution leads to formation of large agglomerated ceramic particles, which is disadvantageous for composite mechanical properties. The process of powder mixing was performed in a Pulverisette 6 planetary mill (Fig. 3.3) in an air atmosphere with the following mixing process parameters: rotational speed of 100 rpm and ball to powder ratio of 5:1 with 1 hour mixing time. The mixing conditions were chosen after earlier experiments of author [80, 81]. The evaluation of distribution of ceramic reinforcement in the intermetallic matrix has been performed by the analysis of microstructure images.

The second stage, powder compaction, consists in filling a mold with the mixed powder and pressing it to form a green body (an unsintered specimen). Applied pressure improves particle rearrangement and bulk density and reduces porosity. These factors are favourable for subsequent sintering, since the diffusion path during sintering process are reduced, and as a consequence of that, a lower temperature and shorter sintering time are required. In the current research investigation the powder has been compacted on high-temperature press HP50-7010 Thermal Technology (Fig. 3.4) just before the sintering process. The high-pressure sintering equipment consists of a hydraulic press and a special thermal chamber. The machine allows a smooth increase of temperature with simultaneous increase of pressure. The powder material was placed in a graphite heater with an internal diameter of 13 mm shielded with a special foil, which minimizes the unfavorable influence of the graphite, and then in a special mold, providing electrical contact and isostatic sintering conditions.

The powder mixtures were pressure sintered in an argon protective atmosphere. The temperature and pressure profiles during sintering process are presented in Fig. 3.5. Temperature was increased up to the sintering temperature T_s with the heating rate of 15°C/min for all the examined cases. The specimens were kept at T_s during the interval (sintering time) t_s and cooled naturally to the room temperature. In the case of sintering time $t_s = 0$ min, the specimens were heated to the sintering temperature and immediately cooled down. The pressure was applied from the beginning of sintering process to the end of the thermal cycle. The specimens were manufactured at different combinations of

Figure 3.3. Planetary mill–Pulverisette 6.

Figure 3.4. Astro Thermal Technology, Model HP50-7010.

the following process parameter values: sintering temperature T_s – 1300°, 1350° and 1400°C, sintering time t_s – 0, 10 and 30 min and external pressure p – 5 and 30 MPa.
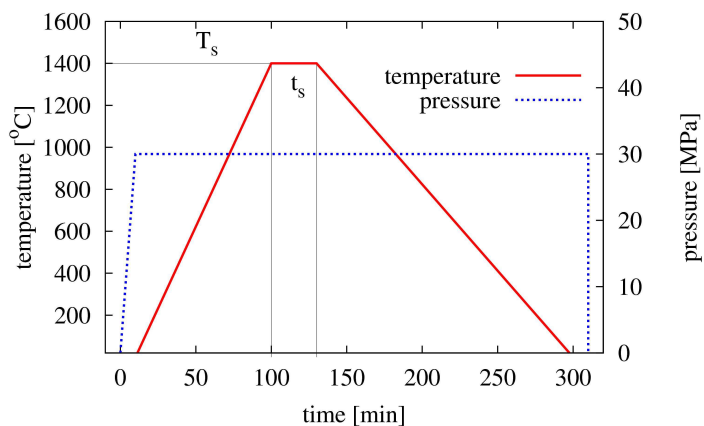
Figure 3.5. Temperature and pressure profiles for the sintering process with $T_s = 1400°C$, $t_s = 30$ min and $p = 30$ MPa.

Density measurements

The sintered cylindrical specimens are shown in Fig. 3.6. The sintering degree was assessed by the relative density, ρ_{rel}, defined as the ratio of the measured bulk (apparent) density ρ and the theoretical density ρ_{theo} for the fully dense material:

$$\rho_{\text{rel}} = \frac{\rho}{\rho_{\text{theo}}}. \tag{3.1}$$

The bulk density of the sintered materials was measured using the hydrostatic method based on the Archimedes' principle [106, 107], which is an effective tool to cope with open and closed types of porosity [108, 109]. The following method requires the specimen to be fully impregnated with a fluid of known density, from which the total open pore volume is calculated [110]. In order to achieve adequate penetration of the sample by fluid, the whole system is boiled for several minutes. Evaluation of the bulk density of a specimen with an arbitrary porosity is based on the measurements of the mass of the dry specimen, m_{s}, the mass of the specimen saturated with a well penetrating liquid (water) m_{n}, and the mass of the liquid saturated specimen suspended in the fluid, m_{w}. Then, the bulk density ρ of the specimen with all kind of porosity is calculated from the following formula [106, 107]:

$$\rho = \frac{m_{\text{s}}}{m_{\text{n}} - m_{\text{w}}} \rho_{\text{f}}, \tag{3.2}$$

where ρ_{f} is the density of the fluid at the measurement temperature.

Figure 3.6. Sintered $NiAl/Al_2O_3$ specimens.

Determination of elastic properties by ultrasonic technique

Elastic properties have been determined using a methodology based on measurements of ultrasonic wave propagation. Ultrasonic techniques have been applied successfully to determine elastic properties of sintered materials including metal-ceramic composites by other research groups [100, 101, 111]. Due to the composite microstructure characterized by intermetallic and ceramic particles randomly oriented and distributed in the material volume, elastic isotropy has been assumed for the investigated composite so its elastic properties can be described in terms of two independent elastic constants, the Young's modulus, E, and Poisson's ratio, ν.

To determine the two elastic constants of isotropic material, two ultrasonic velocities have to be measured, namely the velocity of a longitudinal wave, V_L, and the velocity of a transverse wave, V_T. From the elastic waves theory two following expressions for the elastic moduli of isotropic solid medium, E and ν can be deduced [112]:

$$E = \rho \frac{\left(3V_\mathrm{L}^2 V_\mathrm{T}^2 - 4V_\mathrm{T}^4\right)}{\left(V_\mathrm{L}^2 - V_\mathrm{T}^2\right)}, \tag{3.3}$$

$$\nu = \frac{\left(\frac{1}{2}V_\mathrm{L}^2 - V_\mathrm{T}^2\right)}{\left(V_\mathrm{L}^2 - V_\mathrm{T}^2\right)}, \tag{3.4}$$

where ρ – bulk density, V_L – velocity of longitudinal ultrasonic waves, V_T – velocity of shear ultrasonic waves.

For measurements of ultrasonic velocities in the intermetallic, ceramic and composite specimens the pulse-echo contact technique was employed (Fig. 3.7). In this commonly used technique, the short pulse of ultrasonic energy is introduced to the specimen by the ultrasonic probe coupled to its surface. The pulse undergoes multiple reflections between specimen faces producing successive ultrasonic echoes detected by the probe (Fig. 3.8). The time difference between two successive echoes is exactly the time ultrasonic wave travels through the double sample thickness, L_u. Hence, the ultrasonic wave velocity, V_uw can be calculated from the formula:

$$V_\mathrm{uw} = \frac{2L_\mathrm{u}}{\Delta t_{1-2}}, \tag{3.5}$$

where L_u – thickness of the tested specimen, Δt_{1-2} – time difference between the first and second multiple echoes. The same measurement configuration, shown in Fig. 3.7, can be used for longitudinal and shear waves.
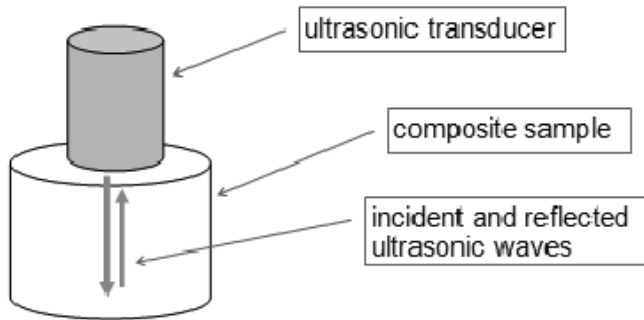
Figure 3.7. Scheme of measurements of ultrasonic wave velocities in specimen with pulse echo technique.

Specimens considered in current ultrasonic study were cylindrical shape with diameter $d_{\mathrm{sp}} = 13$ mm and height $h_{\mathrm{sp}} = 6\text{--}9$ mm. Generation and detection of ultrasonic pulses were performed with ultrasonic flaw detector Panametrics Epoch 4 remotely controlled by a PC with proprietary software for accurate measurements of time-of-flight of ultrasonic pulses. The nominal frequencies of ultrasonic transducers were 10 MHz for longitudinal and 5 MHz for shear waves, respectively. Due to this frequency selection the wavelengths of both types of waves generated in the material were very similar (velocity of the shear waves is roughly half of the longitudinal one) and generally in the range 0.4–0.7 mm. Comparing these wavelengths with the particle sizes in the studied specimens ($d_{\mathrm{NiAl}}^{\mathrm{avg}} = 9.71$ µm and $d_{\mathrm{Al_2O_3}}^{\mathrm{avg}} = 2.28$ µm) it can be assumed that the tested materials were nearly homogenous for the probing ultrasonic waves and elasticity constants determined from ultrasonic measurements were true macroscopic values averaged over hundreds of particles.

To provide acoustic coupling between ultrasonic transducers and specimen faces the glycerin was used for longitudinal and high viscosity resin for transverse waves. The typical view of registered ultrasonic waveforms for higher density (less attenuating) specimens is shown in Fig. 3.8.

A detailed description of the ultrasonic measurements used in the determination of the elastic constant of the sintered NiAl, Al_2O_3, NiAl/Al_2O_3 composite materials was introduced by the Author in [81].

Indirect tensile strength test

Intermetallic-ceramic composites belong to the class of quasi-brittle materials and tend to be weaker in tension than in compression. The tensile strength has been investigated in the present paper as a property characterizing strength
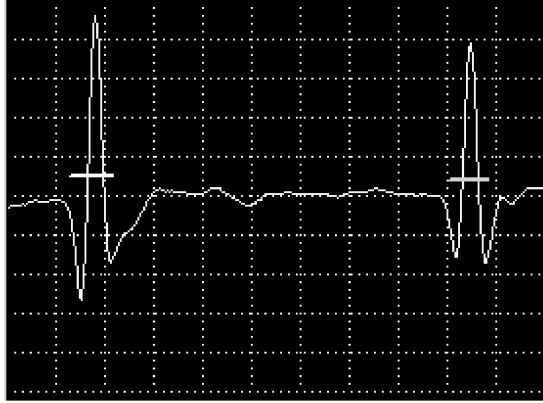
Figure 3.8. Waveforms of two multiple echoes registered on the specimen using 10 MHz longitudinal waves transducer. The time-of-flight between 1st and 2nd echo is measured between signal zero crossing points on the rising edges of peaks designated by the measurements gates.

of the $NiAl/Al_2O_3$ composite materials. A Brazilian-type splitting test has been employed to determine the tensile strength. The Brazilian test or the indirect tensile strength is a standard testing method to determine the tensile strength of intact rocks [113, 114], however, it can be adapted for other brittle materials such as ceramics [115–118].

The Brazilian test consists in compression of a disk-shaped specimen along a diameter until failure induced by tensile stresses perpendicular to the loading direction. The crack starts at the center of the specimen where the tension has maximum level and propagates along the diameter parallel to the loading direction. A formula derived from the theory of elasticity allows to calculate the tensile strength as function of the peak compressive force. The main advantage of the Brazilian test is the simplicity of the specimen preparation and of the testing procedure.

In the present work, composite specimens with diameter $d_{br} = 12$ mm and height $h_{br} = 6$ mm were used in the testing procedure to determine the tensile strength for different sintering parameters. The Brazilian test was performed using hydraulic MTS 810 test machine. The tests were conducted under displacement control at 0.005 mm/s relative velocity. The CCD camera was used for in-situ observation of the specimen surface. The tests were performed using flat platens from hardened steel. No swivel head or interlayers between the loading platens and specimens were used. In order to ensure a proper load transmission between the loading platens and the specimens, the specimens were machined to obtain a nearly ideal cylindrical shape. Figure 3.9a presents an image of

a NiAl/Al$_2$O$_3$ composite specimen during the test and a fractured specimen after the test is shown in Fig. 3.9b.

a)

b)
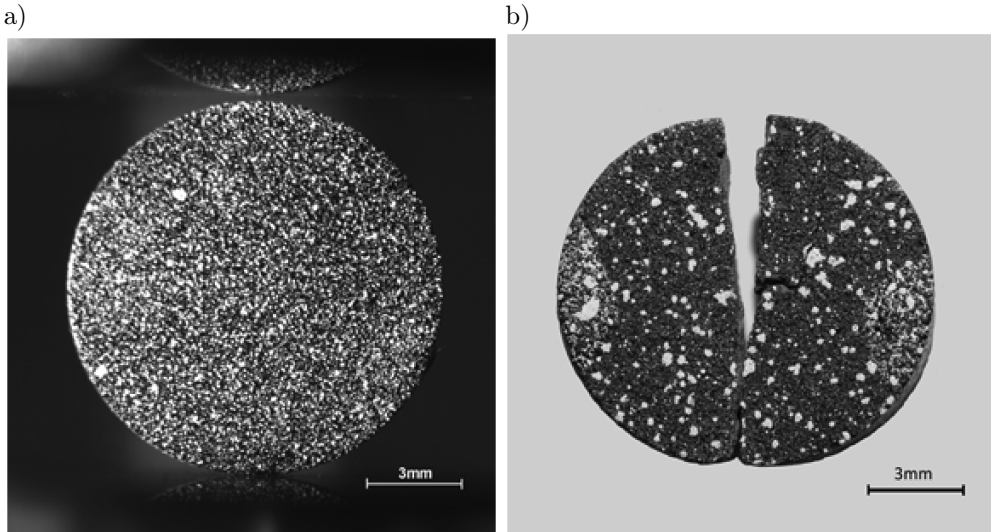
Figure 3.9. Images of NiAl/Al$_2$O$_3$ composite specimens in indirect tensile test: a) before specimen fracture, b) fractured specimen.

The compression force vs. time curves have been registered at each test. The tensile strength σ_{BTS} has been calculated as equal to the tensile stresses at the specimen center corresponding to the force at the failure point, P_{f}, using the following theoretical formula, cf. [113, 114]:

$$\sigma_{\mathrm{BTS}} = \frac{2P_{\mathrm{f}}}{\pi h_{\mathrm{br}} d_{\mathrm{br}}}. \tag{3.6}$$

3.3 Experimental results

3.3.1 Density evolution

Results of density measurements of NiAl, Al$_2$O$_3$ and NiAl/Al$_2$O$_3$ composite specimens sintered at different combination of sintering process parameters are given in Table 3.2. Density evolution curves for different combinations of temperature and pressure for ceramic and intermetallic materials are plotted, respectively in Fig. 3.10a and 3.10b. The relative density – sintering time curves of NiAl/Al$_2$O$_3$ are presented in Fig. 3.11 together with corresponding images of the composite microstructure.

Table 3.2. Evolution of bulk density ρ and relative density $\rho_{\rm rel}$ of hot-pressed NiAl, Al$_2$O$_3$ and NiAl/Al$_2$O$_3$ specimens manufactured at different combination of sintering process parameters.

Sintering process parameters			Al$_2$O$_3$		NiAl		NiAl/Al$_2$O$_3$	
$T_{\rm s}$[°C]	$t_{\rm s}$ [min]	p [MPa]	ρ [g/cm^3]	$\rho_{\rm rel}$	ρ [g/cm^3]	$\rho_{\rm rel}$	ρ [g/cm^3]	$\rho_{\rm rel}$
1300	0	5	2.58	0.65	4.66	0.79	3.86	0.70
1350	0	5	2.93	0.74	4.75	0.80	4.02	0.73
1400	0	5	3.32	0.84	5.24	0.89	4.11	0.74
1300	10	5	2.77	0.70	4.88	0.82	4.01	0.73
1350	10	5	3.13	0.79	4.97	0.84	4.16	0.75
1400	10	5	3.38	0.85	5.33	0.90	4.28	0.78
1300	30	5	3.34	0.84	4.90	0.83	4.10	0.74
1350	30	5	3.61	0.91	5.13	0.87	4.42	0.80
1400	30	5	3.82	0.96	5.45	0.92	4.92	0.89
1300	0	30	3.45	0.87	5.25	0.89	4.99	0.90
1350	0	30	3.56	0.90	5.35	0.91	5.24	0.95
1400	0	30	3.86	0.97	5.42	0.92	5.27	0.95
1300	10	30	3.58	0.90	5.43	0.92	5.03	0.91
1350	10	30	3.85	0.97	5.52	0.93	5.35	0.97
1400	10	30	3.88	0.98	5.78	0.98	5.37	0.97
1300	30	30	3.80	0.96	5.52	0.93	5.44	0.99
1350	30	30	3.93	0.99	5.73	0.97	5.50	1
1400	30	30	3.97	1	5.86	0.99	5.51	1

(theoretical density: NiAl – 5.91 g/cm^3, Al$_2$O$_3$ – 3.97 g/cm^3, NiAl/20%Al$_2$O$_3$ – 5.52 g/cm^3)
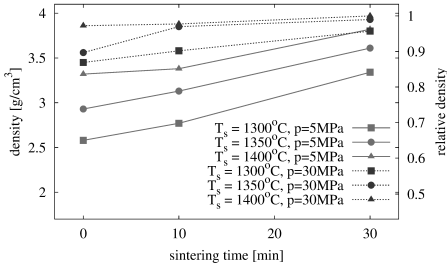
a)   b)
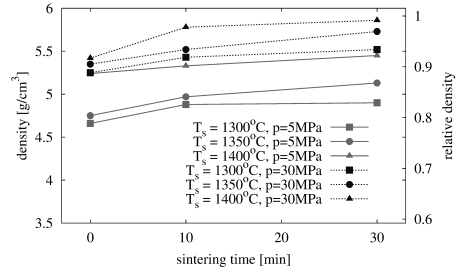
Figure 3.10. Density evolution of: a) pure Al$_2$O$_3$, b) pure NiAl powders manufactured at the different combination of sintering process parameters.

Presented results indicate the general tendency showing the increase of density in the function of combination of applied sintering process parameters. It can be deduced from the observation of density measurements that in the selected range of sintering process parameters almost fully dense materials were obtained. Furthermore, it can be noticed that all the three technological parameters have a strong influence on the degree of material densification and they effect the material properties differently.

a)

b)

c)
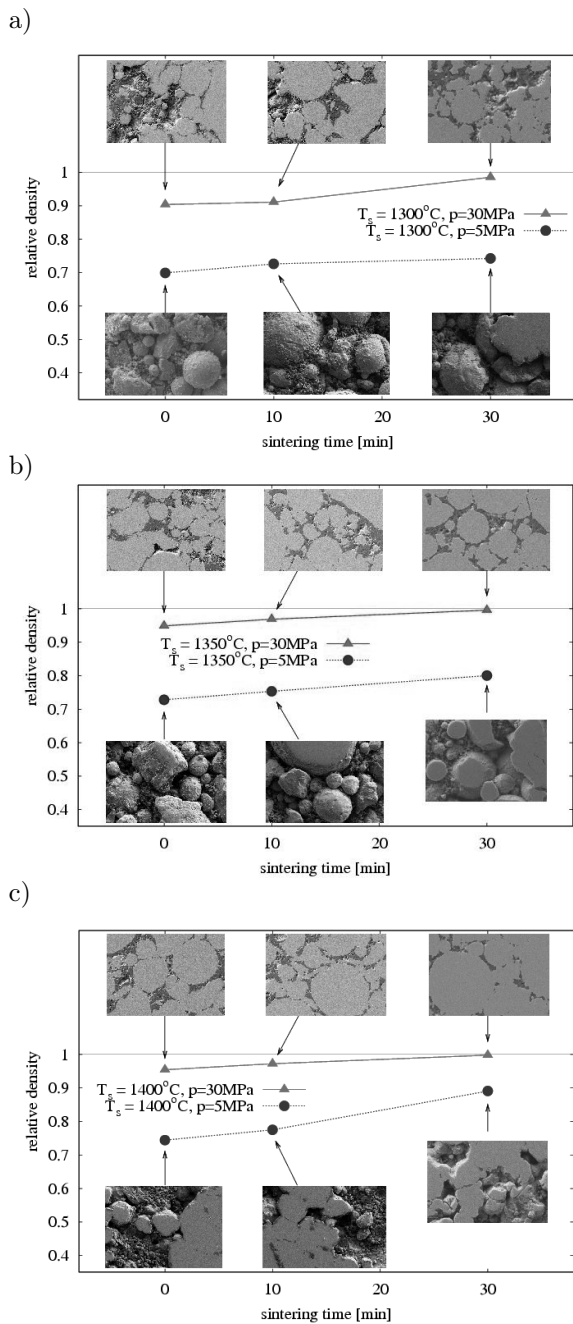
Figure 3.11. Density evolution results of NiAl/Al$_2$O$_3$ composite sintering with pressure 5 and 30 MPa at sintering temperature of: a) $T_s = 1300^\circ$C, b) $T_s = 1350^\circ$C, c) $T_s = 1400^\circ$C.

The results confirm quite an obvious effect of sintering time on the densification. As it can be expected the density increases with time of the sintering process. Density growth is relatively slight, although it can be seen that it is slower when the bulk density approaches the full density.

The results also show significant increase of the density of all three types of material with an increase of compaction pressure. Greater pressure corresponds to a higher density of the sintered material. At the low pressure (5 MPa) the highest relative density of three considered material achieved pure Al_2O_3, almost 96%. Increase of pressure to 30 MPa results in much higher degree of densification even at lower temperatures. Effect of compacting pressure on densification can be explained by easier particle regrouping process at the early stage, intensification of diffusion processes under pressure, activation of diffusion flows and finally, easier pore elimination at the final stage of sintering.

Sintering is a thermally activated process so the temperature plays an important role in it [22, 95]. Sintering temperature is dependent on physicochemical properties of sintered powders, particle size and shape. Naturally, it is assumed that the sintering temperature of a unary systems is 0.6–0.8 of the material melting point. In case of multiphase materials, estimation of sintering temperature is more complicated. It is related to volume fractions of components, their solubility and wettabillity, and the surface energy connected with the global geometry of particles and specific surface area, etc. Depending on the sintering temperature different mass transport mechanisms (surface/grain boundary/volume diffusion, evaporation-condensation, viscous flow) are dominant, e.g., surface diffusion dominates the low-temperature sintering. Mass transport mechanism is an important factor in densification of sintered material.

It can be seen from Table 3.2 that for the constant sintering pressure, when the sintering temperature increases from 1300°C to 1350°C and 1400°C, the density remarkably increases. When the sintering process was performed below 1300°C the specimen material had no integrity indicating the sintering does not occur.

3.3.2 Microstructure evolution

Sintering of Al_2O_3 powder

At the initial stage of Al_2O_3 sintering, intergranular contacts are created, which is a precondition for the transport of the mass between particles. Contacts with the biggest surface areas possible are formed through a proper dispergation of the initial powders or the application of external force. The concentration gradient of lattice vacancies at the contact points of particles and, more specifically, between the free particle surface and the contact surface, i.e. the nucleus of the future neck, is the driving force of the sintering process. This can be observed in Fig. 3.12a. The intermediate phase of aluminium oxide's sintering begins with the changes in particle boundaries and the size of pores which are targeted at taking cylindrical shapes. This stage ends once pore shrinkage has taken place (Fig. 3.12b).

a)   b)
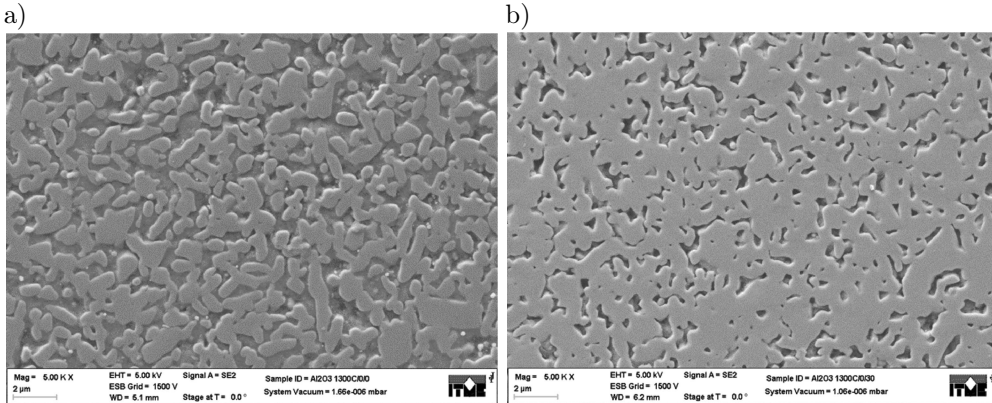
Figure 3.12. SEM images of sintered aluminium oxide at different conditions: a) $T_s = 1300°C, t_s = 0$ min and $p = 5$ MPa, b) $T_s = 1300°C, t_s = 0$ min and $p = 30$ MPa.

There are two alternative final stages of sintering which begins with a significant reduction of the pore volume. The first one takes place under conditions enabling pores to eventually locate in the corners of three or four particles (Fig. 3.13), whereas the second one occurs when a fast discontinuous growth of particles precedes the movements of pores aimed at finding energetically suitable areas and closing them inside crystallites described by Pampuch et al. [119]. This phenomenon was not observed in the studied case.

Any geometrical changes in the shape and dimensions of aluminium oxide particles are a result of diffusive processes. On the other hand, diffusive transfer of ions is directly related to the movement of vacancies which are agglomerated

a)   b)   c)
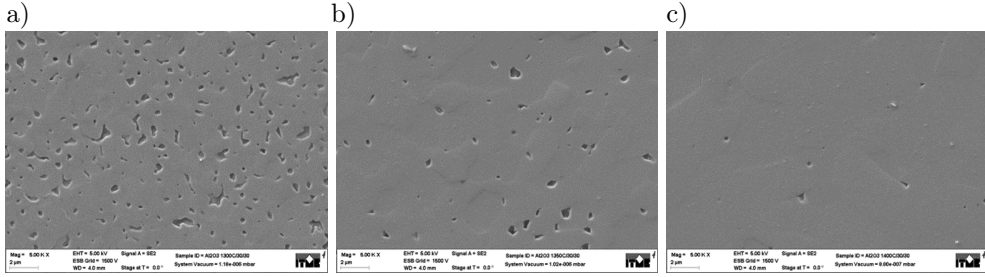
Figure 3.13. SEM images of sintered aluminium oxide at different conditions: a) $T_s = 1300°C, t_s = 30$ min and $p = 30$ MPa, b) $T_s = 1350°C, t_s = 30$ min and $p = 30$ MPa, c) $T_s = 1400°C, t_s = 30$ min and $p = 30$ MPa.

on the pore surface move towards grain boundaries and subsequently migrate towards them. As a result of these changes, the material with a negligible number of pores is eventually thickened.

Sintering of NiAl powder

During the sintering process, NiAl particulate is converted into a polycrystalline material. The evolution of microstructure during sintering is shown in Fig. 3.14 and 3.15.

a)   b)
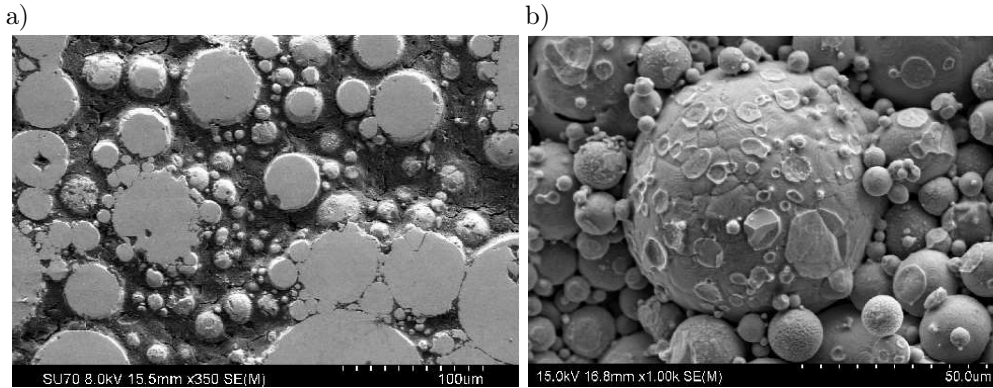
Figure 3.14. SEM images of area of: a) a surface, b) a fracture of NiAl material sintered at conditions of $T_s = 1300°C, t_s = 10$ min and $p = 5$ MPa.

At the initial stage (Fig. 3.14), diffusion bonds are formed between particles. The main driving force of sintering is the reduction of the total surface energy of the system and applied external loading. When the sintering process is continued (Fig. 3.15a) the necks between particles grow due to the mass transport, which is supported by external force.

a)   b)

SU70 8.0kV 15.6mm x350 SE(M)   100um   SU70 8.0kV 15.2mm x300 SE(M)   100um
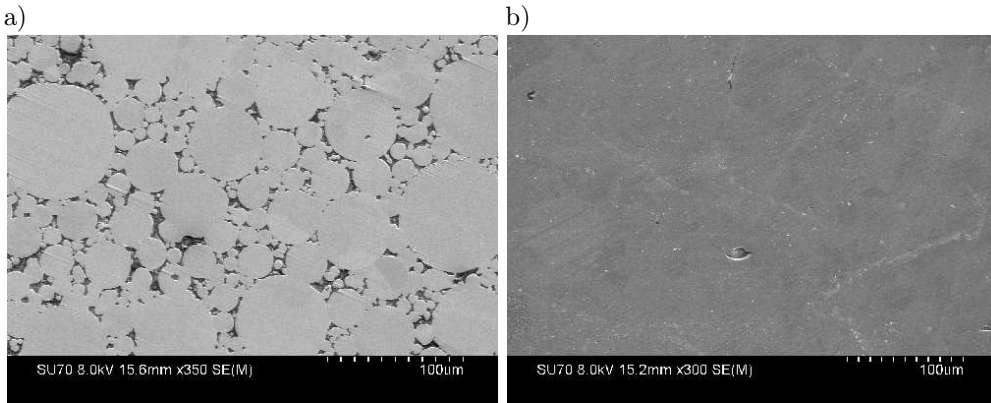
Figure 3.15. SEM images of NiAl material sintered at different conditions: a) $T_{\mathrm{s}} = 1400^{\circ}\mathrm{C}, t_{\mathrm{s}} = 10$ min and $p = 5$ MPa, b) $T_{\mathrm{s}} = 1400^{\circ}\mathrm{C}, t_{\mathrm{s}} = 30$ min and $p = 30$ MPa.

Usually the surface and grain boundary diffusion are dominant mass transport mechanisms in case of sintering. As a result of the stresses in the neck and the surface tension, the particles are attracted to each other, which leads to the shrinkage of the system. The described processes, shrinkage and mass transport are inextricably linked to the total reduction of material porosity (Fig. 3.15b).

Sintering of mixture of NiAl and Al$_2$O$_3$ powders

A closer insight into microstructure development of NiAl/Al$_2$O$_3$ material is provided by the SEM images in Figs. 3.16–3.20 showing microstructure details from the initial- to final-stage sintering.

In densification process during sintering it can be distinguished the following stages: a initial stage characterized by an increase of contact number of particles, particle rearrangement, necks formation; an intermediate stage with the necks growth and pore rounding; and a final stage involved the pores elimination [20, 120]. Duration and intensity of each stage can differ for different materials and various technological conditions of sintering process. Before starting the sintering process, the particles have to be in contact. The movement of particles occurs in the direction of the punch displacement due to the applied external load. Beginning of sintering process results in enlargement of particles contact surfaces and decrease of pores. The forming of first slight necks between intermetallic particles is shown in Fig. 3.16.

One can notice that the behaviour of ceramic particles is affected at this stage of sintering. Individual aluminium oxide particles are located on the surface of intermetallic particles. The bonds are rather weak, the aluminium oxide particles
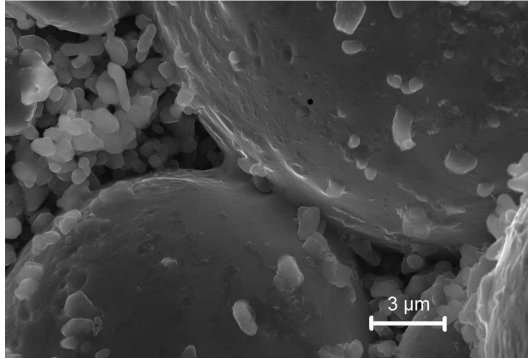
Figure 3.16. Formation of necks between NiAl particles at the initial stage of composite sintering ($T_s = 1400°C, t_s = 30$ min and $p = 5$ MPa).

are mechanically pressed into the NiAl, and some deformation of NiAl surfaces is visible. The great amount of ceramic particles is placed at triangle contacts of NiAl, where they form agglomerates and sintering of them starts.

The intermediate stage is the most important for densification and determining the properties of sintered materials. It is characterized by simultaneous pore rounding, densification and grain growth [22]. This stage of sintering is controlled by the diffusion processes. As it can be seen in Fig. 3.17a, with the increase of temperature the necks are growing and the more compact structure is formed. There are visible particle systems, which consist of two or more particles. The average distance between the adjacent particles decreases and the size of necks is enlarging. The ceramic particles are also connected between themselves. The rise of temperature to 1400°C results in sintering of Al_2O_3 particles (Fig. 3.17b).

a)   b)
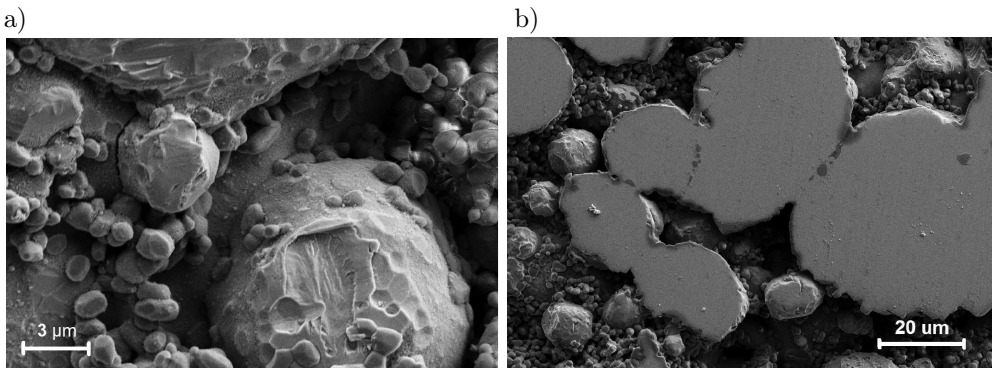
Figure 3.17. Intermediate stage of NiAl/Al_2O_3 composite material sintering: a) $T_s = 1350°C$, $t_s = 30$ min, $p = 5$ MPa, b) $T_s = 1400°C$, $t_s = 30$ min, $p = 5$ MPa.

At this stage it can be observed bonding ceramic reinforcement with NiAl matrix too. In some cases they appear in the neck on particle boundary of sintered NiAl particles (Fig. 3.18). At the beginning of this stage the pore volume amounts to over 20% of the total volume. Finally, it is decreasing to a few percent. Pores with an irregular shape (Fig. 3.19) may become channel pores, which is a typical effect occurring at intermediate stage of ceramic sintering. They form the network which is limited by the surfaces of three adjacent particles and node, where the four channels meet. Enlargement of neck size leads to progressive decrease of amount of pores.

a)
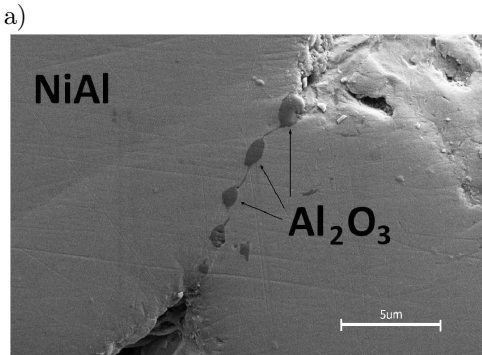
Figure 3.18. Al_2O_3 distribution on the particle boundary of intermetallic particles.

b)
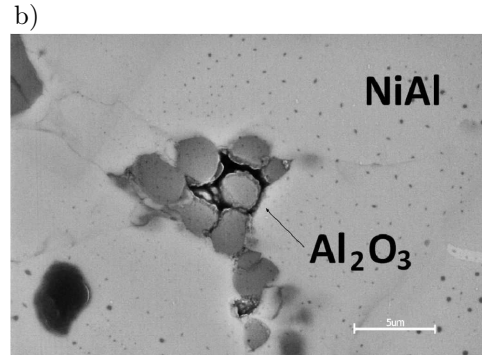
Figure 3.19. Pores in NiAl-Al_2O_3 composite structure ($T_s = 1400°C$, $t_s = 30$ min, $p = 5$ MPa).

The final sintering stage is characterized by the pore elimination from the composite structure. Compared with the initial and intermediate stages, final-stage sintering is relatively slow process. A complex interaction between particles, pores and particle boundaries is decisive for the final densification. According to the literature these interaction can take three forms. Pores retard particle growth to a point, causing the particle boundary to bow and pull against a slow-moving pore. Pores can be dragged by the moving particle boundaries, or the particle boundaries can break away from the pores, leaving them isolated in the particle interior [22]. Some porosity exists between the ceramic particles even after the process ending (Fig. 3.20a). In our case it can be observed some structure discontinuities at the area of metal-ceramic interface, which can have an significant effect on the materials properties. It should be underlined that finally almost fully dense materials with low amount of porosity (less than 1%) have been obtained (Fig. 3.20b).

a)   b)
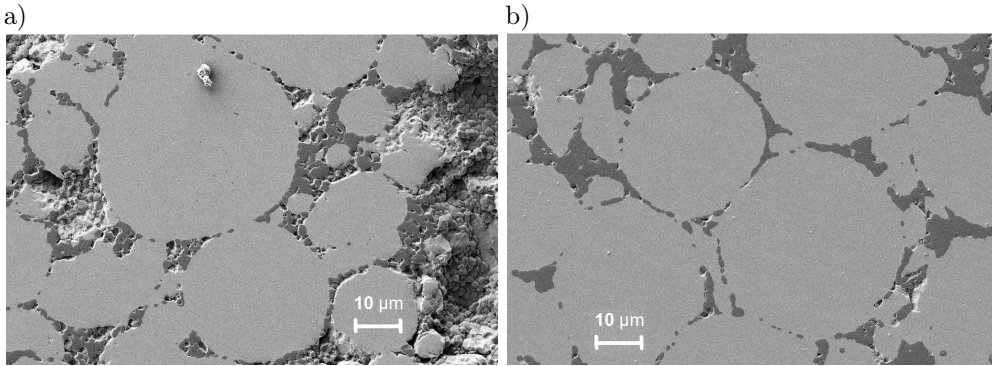
Figure 3.20. Final stage of sintering – pores elimination: a) $T_{\mathrm{s}} = 1400°\mathrm{C}$, $t_{\mathrm{s}} = 0$ min, $p = 30$ MPa, b) $T_{\mathrm{s}} = 1400°\mathrm{C}$, $t_{\mathrm{s}} = 10$ min, $p = 30$ MPa.

3.3.3 Elastic properties evolution

The elastic constants of the obtained sintered samples were determined by the measurements of ultrasonic velocities described in Subsec. 3.2. Table 3.3 presents detailed results of measurements of the Young's modulus E and Poisson's ratio ν of the pure ceramic Al_2O_3, pure intermetallic NiAl and NiAl/Al_2O_3 composite specimens sintered in different conditions.

Based on the presented values, the relations between elastic moduli and the relative density ρ_{rel} for three considered materials were illustrated in Fig. 3.21. In all cases, the substantial increase of the Young's modulus with the relative density can be seen. For example, for pure ceramics, the difference between the maximum and minimum value of E equals 78%. The change of the Poisson's ratio is less pronounced. Only in case of NiAl material, a slight increase of Poisson's ratio can be observed with the increase in density. The growth of the Young's modulus of Al_2O_3 and NiAl during the material's densification is similar. Additionally, in case of the Poisson's ratio, its growth for the intermetallic material is more significant than for ceramics.

The values of elastic constants of the NiAl/Al_2O_3 composite apparently depend on the values of elastic constants of its constituent phases with respect to the volume content. Due to the intermetallic and ceramic phase content in the analyzed composite material, i.e., 80% of NiAl and 20% of Al_2O_3, the value of NiAl/Al_2O_3 elastic constants should be close to the intermetallic one. Particularly at low relative density, $\rho_{\mathrm{rel}} < 0.95$, this trend is confirmed regardless of the sintering process parameters – the results of the composite Young's modulus are fairly similar to the Young's modulus of NiAl (Fig. 3.21a). The explanation of this homogeneity of results can be found in the section devoted

Table 3.3. Evolution of Young's modulus E and Poisson's ratio ν of hot-pressed Al_2O_3, NiAl and NiAl/Al_2O_3 specimens determined by ultrasonic measurements.

Sintering process parameters			Al_2O_3		NiAl		NiAl/Al_2O_3	
$T_s[^\circ C]$	t_s [min]	p [MPa]	E [GPa]	ν	E [GPa]	ν	E [GPa]	ν
1300	0	5	88	0.221	70	0.283	44	0.258
1350	0	5	136	0.221	81	0.288	53	0.242
1400	0	5	238	0.217	127	0.289	56	0.268
1300	10	5	130	0.218	82	0.286	61	0.275
1350	10	5	197	0.219	116	0.282	81	0.277
1400	10	5	235	0.220	135	0.286	85	0.277
1300	30	5	195	0.217	88	0.279	67	0.280
1350	30	5	242	0.230	131	0.291	81	0.259
1400	30	5	323	0.220	149	0.296	117	0.271
1300	0	30	238	0.212	122	0.301	151	0.294
1350	0	30	303	0.227	134	0.297	175	0.292
1400	0	30	397	0.227	153	0.305	195	0.292
1300	10	30	307	0.225	157	0.313	164	0.284
1350	10	30	382	0.231	169	0.307	186	0.291
1400	10	30	400	0.222	176	0.313	208	0.297
1300	30	30	357	0.231	167	0.309	214	0.285
1350	30	30	393	0.230	178	0.313	218	0.287
1400	30	30	404	0.232	183	0.321	219	0.286

a)   b)
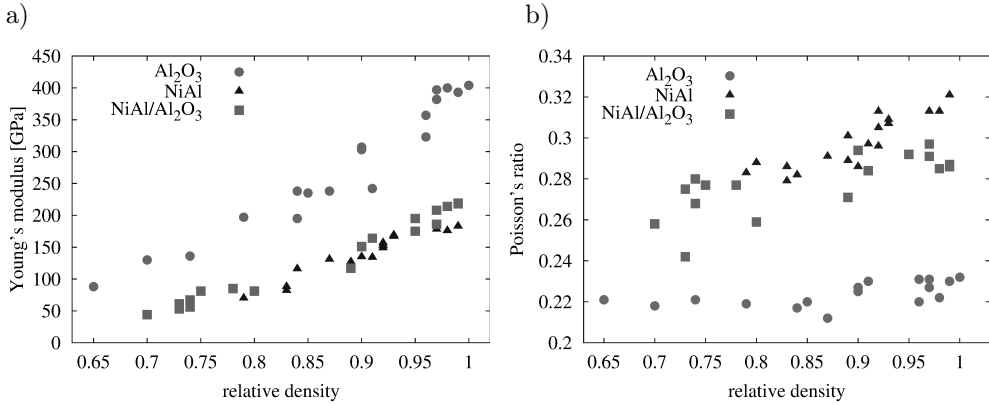
Figure 3.21. Experimental results of: a) Young's modulus, and b) Poisson's ratio of hot-pressed Al_2O_3, NiAl and NiAl/Al_2O_3 specimens as a function of relative density.

to the microstructure. Figure 3.14 and 3.20 shows the microstructure of NiAl and NiAl/Al$_2$O$_3$ samples with relative density close to 0.9. In the first one it can be seen a skeleton with small alumina particles created on the surface of NiAl particles. At low densities, these small ceramic particles located on the NiAl surface have no impact on the stiffness of the composite. In comparison to pure NiAl samples, ceramic particles in composite materials slightly reduce the porosity with no significant effect on the stiffness. For higher relative densities, $\rho_{\mathrm{rel}} > 0.95$, ceramic particles are strongly connected with intermetallic ones in the whole volume of the composite material (Fig. 3.20), which is the major reason for a higher stiffness than in case of pure intermetallic material.

Further analysis concerns the comparison of the experimental results of elastic properties of NiAl/Al$_2$O$_3$ composite material with the theoretical approximations. The theoretical dependence is based on the FEM calculations performed by Roberts and Garboczi [121, 122], who introduced the overlapping spherical pores and overlapping solid spheres models. The relationships for both models can be approximated by fairly simple analytical expressions [122]:

$$E = E_0 \left(\frac{\rho_{\mathrm{rel}} - \overline{\rho}_0}{1 - \overline{\rho}_0} \right)^{\mathrm{c}}, \tag{3.7}$$

$$\nu = \nu_0 + \left(\frac{1 - \rho_{\mathrm{rel}}}{1 - \overline{\rho}_1} \right)(\nu_1 - \nu_0), \tag{3.8}$$

where E and ν are the Young's modulus and Poisson's ratio of a sintered material, respectively, E_0 and ν_0 are the Young's modulus and Poisson's ratio of a fully dense material, and $\overline{\rho}_0$, $\overline{\rho}_1$, c and ν_1 are the constants.

To compare the experimental results and theoretical approximations it was presented the results of ultrasonic measurements on the graph showing dependence of E modulus on the relative material density together with the predictions of both considered models (Fig. 3.22). The constant values used in the calculation of prediction lines of the overlapping spherical pores and the overlapping solid spheres model have been taken from [122] and are given in Table 3.4.

Table 3.4. Constant values of the overlapping spherical pores and the overlapping solid spheres model parameters.

Model/constant	$\overline{\rho}_0$	c	$\overline{\rho}_1$	ν_1
Overlapping spherical pores model	0.182	1.65	0.160	0.221
Overlapping solid spheres model	0.348	2.23	0.528	0.140
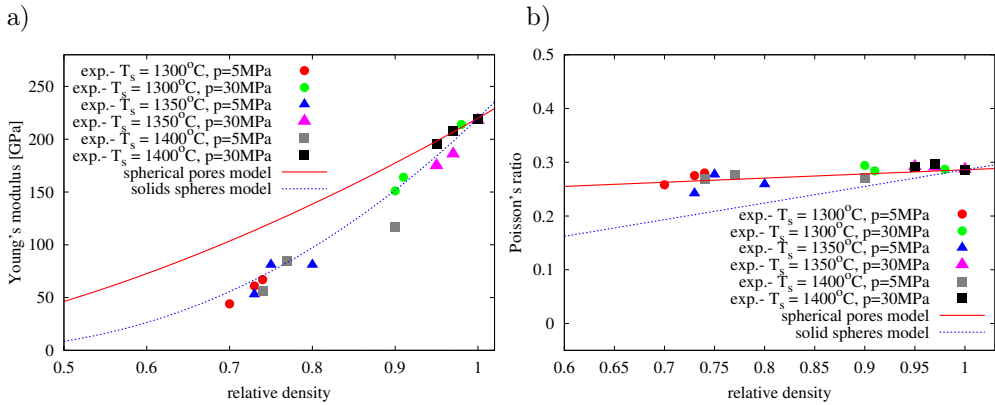
Figure 3.22. Dependence of: a) Young's modulus, b) Poison's ratio on relative density of partially sintered NiAl/Al₂O₃ composite. Comparison of ultrasonic measurements with predictions of theoretical models [122].

It can be seen in Fig. 3.22 that for higher porosities (relative density $\rho_{rel} <$ 0.95), the experimental results clearly follow the predictions of the overlapping solid spheres model. This trend is maintained down to the lowest measured relative densities of about 0.7. This agreement can be explained by a similarity of the microstructure of the NiAl/Al₂O₃ composite material with high porosity (Fig. 3.17) with the geometry of the overlapping solid spheres model shown in Fig. 3.23a.
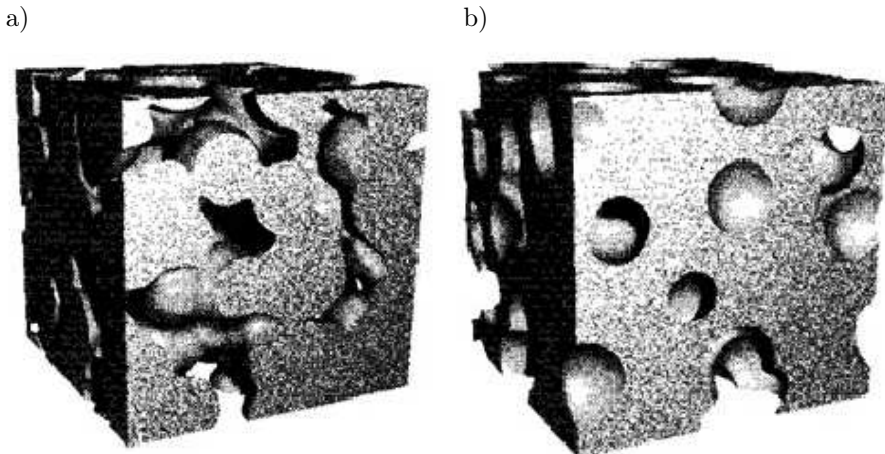
Figure 3.23. Pieces of the models of porous media: a) the overlapping solid spheres, b) the overlapping spherical pores [122].

For small porosities (relative density $\rho_{rel} > 0.95$), prediction lines from both models, the overlapping solid spheres and overlapping spherical pores, are close to each other, and both approximate pretty well experimental points in this range. Theoretically, the overlapping spherical pores model should be more suitable for materials with small porosity. Its morphology (Fig. 3.23b) corresponds to isolated spherical pores in materials with low porosity [121]. This correspondence can also be seen when comparing the geometry in Fig. 3.23b with the images of the microstructure of a nearly fully-dense NiAl/Al$_2$O$_3$ composite (Fig. 3.20) where a small number of spherical pores is visible. A good agreement between the overlapping spherical pores model and experimental results was confirmed in the paper [111], where microstructural observations and experimental verification of sintered alumina were performed.

Fig. 3.22b presents a graph showing relative density dependence of the Poisson's ratio. In this case the experimental results follow predictions of the overlapping spherical pores model in the whole range of measured relative densities. At the same time they deviate considerably from the overlapping solids spheres model what seems to be in contradiction with conclusions drawn from the microstructural analysis and good agreement with this model observed for the Young's modulus. Explanation of this unexpected behaviour of the Poisson's ratio in partially sintered NiAl/Al$_2$O$_3$ composites is not simple. It seems to stem from the inherent weaknesses of the overlapping solids spheres model based on the assumption of random, statistical distribution of solid spheres in the space volume.

Experimental results of Young's modulus of the full-dense NiAl/Al$_2$O$_3$ were also confronted with theoretical models of elastic properties of two-phase porous materials – the Voigt-Reuss and Hashin-Shtrikman (H-S) bounds. Calculations of the Reuss, Voigt and Hashin-Shtrikman limits for E were based on the values of elastic moduli of NiAl and Al$_2$O$_3$ determined from ultrasonic measurements and given in Table 3.3. The Voigt, Reuss and the Hashin-Shtrikman limits for the Young's modulus were calculated following the procedure for two phase polycrystalline composites described in [101, 123]. The value of the theoretical bounds are presented as follows: Voigt-Reuss: 205.5–227.2 GPa and Hashin-Shtrikman: 213.6–217.8 GPa, respectively. The agreement between the measurement results and theoretical calculations is satisfied. The maximum value measured on the samples of NiAl/Al$_2$O$_3$ composite – 219 GPa is well within Voigt-Reuss limits, but slightly above the Hashin-Shtrikman limits. This minor discrepancy may be caused by measurement errors as well as by some statistical fluctuations in the real phase content of the NiAl/Al$_2$O$_3$ specimens.

In addition to the study of relation between density and elastic constants, the analysis of the sintering process parameters impact on Young's modulus has been perfomed. Influence of sintering temperature T_s, sintering time t_s and external pressure p on elastic modulus of the pure ceramic, pure intermetallic and composite specimens is well-illustrated in Fig. 3.24, respectively.

a)   b)

c)
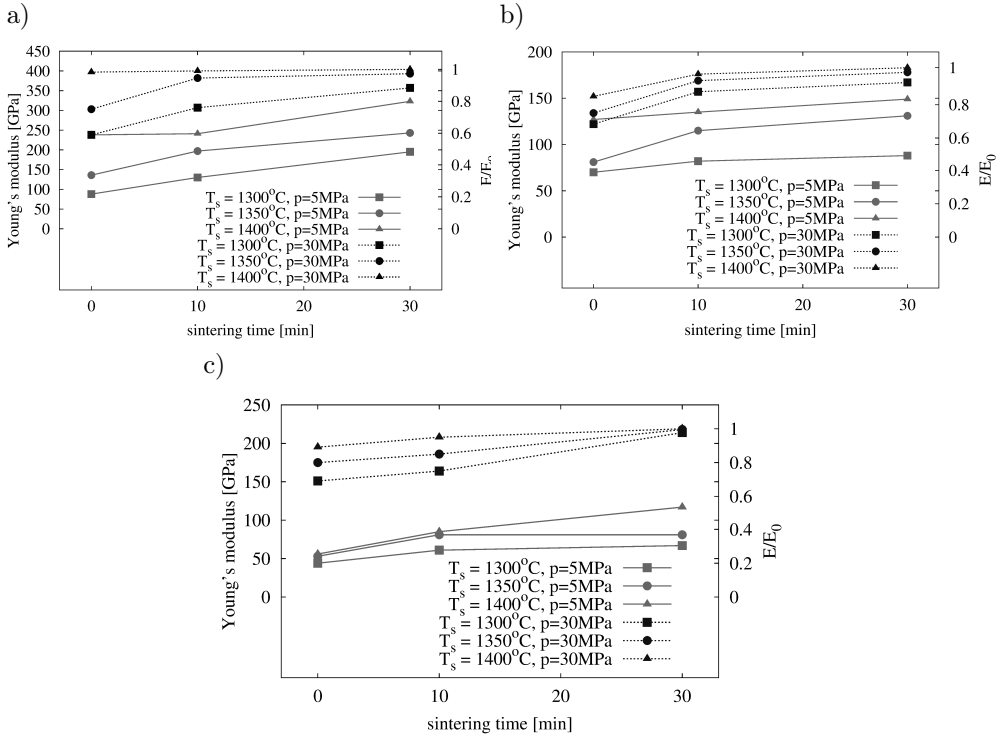
Figure 3.24. Experimental results of Young's modulus of: a) pure alumina, b) pure NiAl, c) NiAl/Al$_2$O$_3$ composite material as a function of sintering time, manufactured in different combination of sintering temperature and pressure.

It is rather obvious that for all three materials the elastic modulus rose when increasing all three sintering process parameters. It can be seen that samples manufactured at theoretically least favorable sintering conditions show low and dissatisfactory values of material stiffness. Specifically, it can be seen in example of alumina specimen sintered at $T_\mathrm{s} = 1300°C$, $t_\mathrm{s} = 0$ min, $p = 5$ MPa, which the Young's modulus stays at the level of 22% of the Young's modulus for fully dense alumina E_0. In general, all materials sintered at low pressure (5 MPa) have a very low Young's modulus, regardless of other sintering process parameters (temperature and time). Obviously, the main reason for such low stiffness

is insufficient material densification; however, the effect of the microstructural features should also be considered. Figures 3.12, 3.14 and 3.16 present the microstructure of pure ceramic, pure intermetallic and composite samples with a low value of E, where high distribution of irregularly shaped pores can be observed. Sintered materials exhibit a decreasing strength (and stiffness) when the pore shape becomes irregular; small spherical pores are preferable. Creating favorable pore configuration depends on the process conditions [22]. Samples manufactured at high pressure (30 MPa) are characterized by the Young's modulus between 87 and 100% of the value for fully dense samples. The importance of sintering pressure as a critical parameter in the manufacturing process can be particularly seen in case of a composite material for which the difference between the Young's modulus for the samples sintered at 5 and 30 MPa is the most significant (Fig. 3.24c). Higher external pressure allows to obtain a material with a low-porosity microstructure and a low number of isolated spherical pores (Fig. 3.20).

3.3.4 Tensile strength evolution

Experimental results of the indirect tensile strength (Brazilian) tests described in Subsec. 3.2 are given in Table 3.5. The experimental examination of tensile strength was held for $NiAl/Al_2O_3$ composite specimens. The results were obtained by single strength measurement for each specimen. Maximum compressive force P_f was directly measured in the tests and the corresponding tensile strength was calculated according to Eq. (3.6).

The results given in Table 3.5 indicate that the tensile strength of $NiAl/Al_2O_3$ composite specimen is closely related to degree of sintering indicated by the relative density. The strength of the sintered material increases with increasing density. It can be clearly seen in Fig. 3.25a in which the tensile strength values determined for all the specimens are plotted as a function of the relative density of the composite.

Experimental results in Fig. 3.25a have been approximated with a curve according to the empirical relationship proposed by Ryshkewitch [124]:

$$\sigma_{\mathrm{mod}} = \sigma_{\mathrm{o}}\exp(-q\theta), \tag{3.9}$$

where σ_{mod} is the strength for a given relative density, σ_0 is the maximum strength for the full dense material, q is a constant, and θ is porosity ($\theta = 1 - \rho_{\mathrm{rel}}$). The curve approximating the experimental results in Fig. 3.25a is obtained taking $q = 11$ in the formula (3.9).

Table 3.5. Experimental results of tensile strength of hot-pressed NiAl/Al$_2$O$_3$ composite determined from indirect tensile test.

Relative density ρ_{rel}	Sintering process parameters			Maximum applied force P_{f} [N]	Tensile strength σ_{BTS} [MPa]
	$T_{\mathrm{s}}[°\mathrm{C}]$	t_{s} [min]	p [MPa]		
0.70	1300	0	5	1124	9.94
0.73	1350	0	5	823	7.28
0.74	1400	0	5	1856	16.41
0.73	1300	10	5	1171	10.36
0.75	1350	10	5	2466	21.81
0.77	1400	10	5	3160	27.95
0.74	1300	30	5	1849	16.35
0.80	1350	30	5	3879	34.31
0.90	1400	30	5	5120	45.29
0.90	1300	0	30	6193	54.78
0.95	1350	0	30	12352	109.27
0.95	1400	0	30	13643	120.69
0.91	1300	10	30	8903	78.75
0.97	1350	10	30	16743	148.11
0.97	1400	10	30	17713	156.69
0.98	1300	30	30	19092	168.89
0.99	1350	30	30	23563	208.44
0.99	1400	30	30	25689	227.25

a)

b)
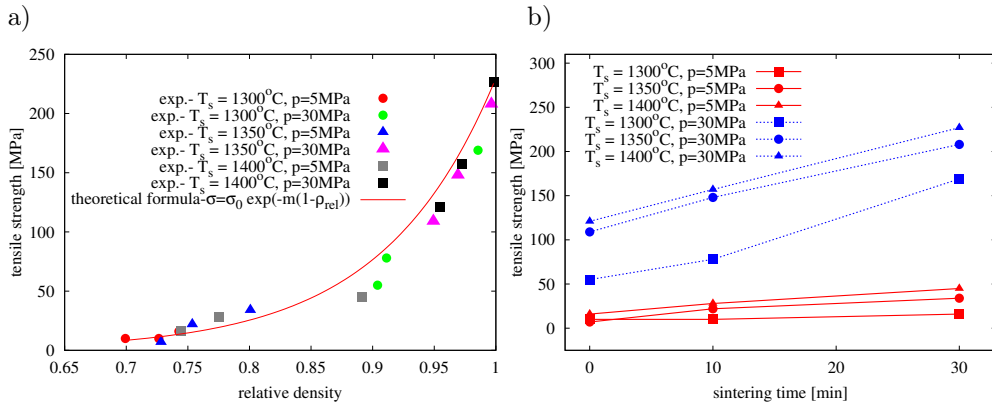
Figure 3.25. Experimental results of tensile strength of NiAl/Al$_2$O$_3$ composite as a function of: a) relative density, b) sintering time for different combination of sintering temperature and pressure.

The Ryshkewitch model has been originally developed to study influence of controlled porosity on the compressive strength of sintered pure alumina, however the analytical form of the fitting curve of the current model can also be suitable for tensile data. It was used to analyse relation between the tensile strength and porosity/density in other papers [125–127] and gave reasonably good correspondence between the model and experimental data.

Similarly, in our case, it can be clearly observed that the experimental data from the tensile tests have the same trend as those analyzed in [124] and follow the analytical curve. The effect of porosity (relative density) on the strength can be explained by microstructure considerations. Firstly, pores reduce the load-bearing cross-sectional area. Secondly, pores cause stress concentration on the interparticle sinter bond (necks), hence at high porosity these bonds determine material strength.

Figure 3.26a shows a fracture surface of the 90% dense $NiAl/Al_2O_3$ specimen sintered in temperature of 1400°C during 30 min with external pressure 5 MPa. It can be seen here some broken intermetallic sinter necks, which create a skeleton body with small alumina particles in the surface of NiAl particles. In low densities, these small ceramic particles located in the NiAl surface do not affect the composite strength, fracture was along sintered NiAl particle contacts. Some Al_2O_3 particles, due to their location between NiAl particles can cause unfavorable stresses during sintering, leading to microcracks, which reduce composite strength.

a)   b)
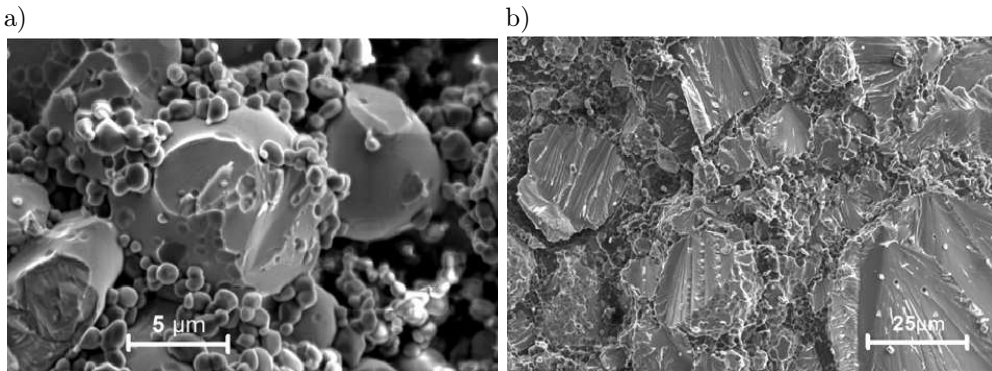
Figure 3.26. Microstructure of fracture surface of $NiAl/Al_2O_3$ composite specimen sintered in a) $T_s = 1400°C$, $t_s = 30$ min, $p = 5$ MPa, b) $T_s = 1400°C$, $t_s = 30$ min, $p = 30$ MPa.

For higher relative densities, close to 1, elimination of pores increases the load-bearing cross-sectional area, which is the major reason of a strength growth. The longer sintering time, the denser, less porous and stronger is the sintered

material. This is confirmed in Fig. 3.25b presenting evolution of tensile strength of NiAl/Al$_2$O$_3$ composite specimen as a function of sintering time for different sintering processes.

The curves in Fig. 3.25b also illustrate the effect of sintering temperature and pressure. With the increase of temperature and pressure, the tensile strength rises. The difference in applied pressure during sintering has a crucial impact on the tensile strength of specimens sintered in $T_s = 1400°C$ and $t_s = 30$ min – the difference in the tensile strength for the specimens sintered under 5 and 30 MPa amounts to 182 MPa. The effect of the sintering temperature and time on the tensile strength is also significant, but it seems smaller than that of the applied pressure. Generally, it can be stated that change of any parameter improving the degree of sintering is favorable to mechanical properties [22].

Observation of the fracture surface of the fully dense NiAl/Al$_2$O$_3$ composite shown in Fig. 3.26b indicates that in a fully sintered composite NiAl sinter bonds have almost equal strength as intermetallic particle. Therefore the fracture in Fig. 3.26b passes through NiAl particles.

Summary

Experimental investigation of powder metallurgy process of pure NiAl, pure Al$_2$O$_3$ and NiAl-Al$_2$O$_3$ composite powders have been performed. Employing the hot-pressing technique specimens have been manufactured at different combinations of sintering process parameters: temperature, pressure and time. The sinterability of the two individual components and the composite material has been compared. The evolution of density, microstructure, elastic constants and mechanical strength during the sintering has been determined in relation to the sintering process parameters.

The results of the performed experimental studies have a theoretical and practical significance enabling a better understanding of the process mechanisms. The knowledge of evolution of material properties of the sintered material could be used to optimize manufacturing process. Appropriate process parameters (temperature, pressure, time) allowing to obtain a material with desired properties could be determined [128].

The results of the present investigation provide valuable information for development of theoretical models of sintering. The density and elastic constants evolution, strictly related to sintering kinetics, are essential in calibration and validation of numerical models [13]. Correlation between experimental and modeling results leads to better understanding of sintering processing of complex systems [129].

4

Numerical model of powder metallurgy process

Introduction

Different approaches used in modeling of powder sintering have been reviewed in Subsec. 1.2. This review has shown that the topic of modeling of powder metallurgy is an important topic of the current world-wide research. The complexity of the process, described in Sec. 2 and shown in the analysis of the own experimental studies in Sec. 3, poses challenges for theoretical and numerical modeling.

This section presents the theoretical formulation of the original thermo-viscoelastic model of a powder metallurgy process developed within the discrete element method (DEM). The presented model is an extension of the viscoelastic model presented earlier in [130]. The standard viscous sintering model used by other authors, cf. [58], has been enriched in [130] by adding a spring connected in series to the viscous rheological element, which allows to account for elastic component of deformation. In the present formulation, thermal expansion has been added to the Maxwell branch.

The section contains brief introduction to the discrete element method as the framework for the sintering model implementation, detailed formulation of the contact model for the compaction and sintering stages and the idea of the algorithm smoothening the transition between the models used in these two stages.

Explicit time integration of the equations of motion and constitutive relationships is presented. The limitations imposed by the conditional stability and possibilities to overcome this drawback by scaling are discussed. Finally, determination of the material model parameters is presented.

The study of algorithm of smooth transition between the compaction and sintering models (Subsec. 4.6), scheme of time integration (Subsec. 4.7) and numerical stability of applied models (Subsec. 4.8) have been presented in [130].

4.1 Introduction to discrete element modeling

The discrete element method (DEM) is a relatively new numerical method based on the discrete model of material. The theoretical concept of the DEM was presented by Cundall in [131] in 1971. Later on, especially in the recent twenty years, together with growing computer capacities, the DEM was rapidly developing [132–145].

In the DEM, the material is represented by a large collection of rigid or deformable discrete elements interacting among one another with contact forces. Discrete elements can be of arbitrary shape [146]. In the present work, spherical particles are used as discrete elements. The DEM formulation employing spherical particles was first introduced by Cundall [131]. It has been commonly accepted that the DEM algorithm must describe finite (large) displacements and rotations of discrete elements, must allow the separation of connected elements and must automatically detect the contact of existing and emerging pairs of discrete element [147] .

A particle interaction model in the DEM can take into account different effects such as:

- elasticity,
- friction,
- damping and viscosity,
- cohesion and adhesion.

Long range forces such as electrostatic or magnetic forces can also be considered. The interaction model in the DEM can be viewed upon as a micromechanical material model. A required macroscopic material behaviour can be obtained by taking an adequate interaction model with appropriate parameters.

Currently, the discrete element method is a widely acceptable method and has become a popular and useful tool for modeling discrete systems, especially in geomechanics. The DEM is an excellent tool for modeling granular materials assuming incohesive and rigid particle interaction [148, 149] or deformable and cohesive interaction [57, 150, 151]. The use of cohesive models allows to model rocks [152–155] or cohesive soils [156, 157]. Possibility of breakage of cohesive binds allows to model initiation and propagation of fractures in materials. Figure 4.1 shows a DEM simulation of a failure of a rock specimen during an uniaxial compressive strength test.
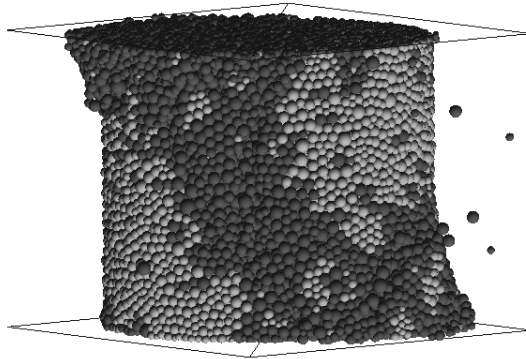
Figure 4.1. Simulation of unconfined compression test – failure mode (particles with broken cohesive bonds are marked with different colour) [152].

DEM is also used for the needs of the construction industry for modeling structural materials such as concrete [158–160] or asphalt [161, 162]. The discrete element method provides a suitable framework for implementation of classical particle models of sintering [59, 64, 65]. Applications of the discrete element method in the field of sintering process have been reviewed in Subsec. 1.2.

4.2 Basic assumptions of the numerical model of powder metallurgy process

The following assumptions has been made for the development of the discrete element model of a powder metallurgy process:

- Powder particles will be represented by spherical discrete elements.
- Particle size and size distribution should be the same as in the real powder.
- Size of model of powder specimen will be scaled down due to the computational limitation.
- Model should be capable to simulate metallurgy process for one-phase and two-phase mixtures of powders.
- The model should allow simulation of all the stages of the process: compaction, sintering and cooling.
- The interaction of powder particles at the compaction stage will take into account elastic deformation, viscous dissipation and friction at the contact point.

- The interaction model for the sintering stage will take into account elastic and inelastic (viscous) deformation.
- Thermal expansion will be taken into account.
- Temperature evolution will be prescribed.
- Uniform temperature distribution will be assumed in the specimen.
- Heat conduction will be neglected.
- Powder particle interaction during cooling will be modeled using cohesive elastic model with damping.
- Powder interaction with a mold will be modeled assuming the frictional contact.
- Plastic deformation and creep will be neglected, both in the compaction and sintering stage.

The discrete element model developed according to the above assumptions has been implemented in the discrete element code DEMpack [163].

4.3 Equations of motion

The translational and rotational motion of discrete elements (Fig. 4.2) is described by means of the Newton-Euler equations of rigid body dynamics. For the i-th spherical particle we have

$$m_i \ddot{\mathbf{u}}_i = \mathbf{F}_i \,, \tag{4.1}$$

$$J_i \dot{\boldsymbol{\omega}}_i = \mathbf{T}_i \,, \tag{4.2}$$

where $\mathbf{u}_i$ is the element centroid displacement in a fixed (inertial) coordinate frame, $\boldsymbol{\omega}_i$ – angular velocity, m_i – element (particle) mass, J_i – moment of inertia, $\mathbf{F}_i$ – resultant force, and $\mathbf{T}_i$ – resultant moment about the central axes. Vectors $\mathbf{F}_i$ and $\mathbf{T}_i$ are sums of all forces and moments applied to the i-th element due to external load, $\mathbf{F}_i^{\text{ext}}$ and $\mathbf{T}_i^{\text{ext}}$, respectively, and contact interactions with neighbouring spheres and boundary surfaces $\mathbf{F}_{ij}^{\text{c}}$, $j = 1, \ldots, n_i^{\text{c}}$, where n_i^{c} are the number of elements being in contact with the i-th discrete element.

$$\mathbf{F}_i = \mathbf{F}_i^{\text{ext}} + \sum_{j=1}^{n_i^{\text{c}}} \mathbf{F}_{ij}^{\text{c}} \,, \tag{4.3}$$

$$\mathbf{T}_i = \mathbf{T}_i^{\text{ext}} + \sum_{j=1}^{n_i^{\text{c}}} \mathbf{s}_{ij}^{\text{c}} \times \mathbf{F}_{ij}^{\text{cont}} \,, \tag{4.4}$$

where $\mathbf{s}_{ij}^{c}$ is the vector connecting the centre of mass of the i-th element with the contact point with the j-th element.
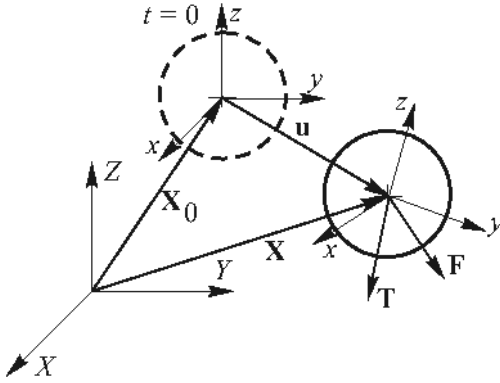
Figure 4.2. Motion of a rigid particle [164].
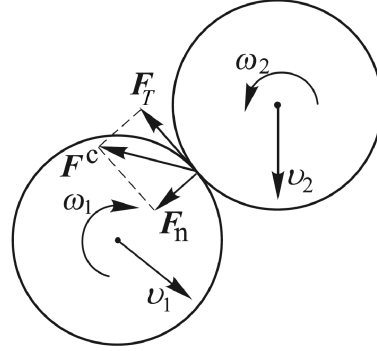
Figure 4.3. Contact interaction between two discrete elements [164].

Contact forces $\mathbf{F}_{ij}^{c}$ are obtained using a constitutive model formulated for the interaction of two particles (Fig. 4.3). In the interaction model, the contact force $\mathbf{F}_{ij}^{c}$ can be decomposed into the normal and tangential components, $(\mathbf{F}_n)_{ij}$ and $(\mathbf{F}_T)_{ij}$, respectively.

$$\mathbf{F}_{ij}^{c} = (\mathbf{F}_n)_{ij} + (\mathbf{F}_T)_{ij} = (F_n)_{ij}\mathbf{n}_i + (\mathbf{F}_T)_{ij}, \tag{4.5}$$

where $\mathbf{n}_i$ is the unit vector normal to the particle surface at the contact point and directed outwards from the particle i.

A typical loop of a discrete element algorithm mainly consists of two stages (Fig. 4.4). In the first stage, the contact forces are computed for the contacting particle pairs. The second stage involves the application of equation of motion for each of the elements to obtain the acceleration of the particles, after the explicit integration the displacement, and consequently new location of the particles.

Equations of motion (4.1) and (4.2) are integrated in time using an explicit central difference type algorithm, the so-called leap-frog method. Time integration of Eq. (4.1) within this algorithm is based on the following finite difference schemes for accelerations and velocities:

$$\ddot{u}_i^n = \frac{\dot{u}_i^{n+1/2} - \dot{u}_i^{n-1/2}}{\Delta t}, \tag{4.6}$$

$$\dot{u}_i^{n+1/2} = \frac{u_i^{n+1} - u_i^n}{\Delta t}, \tag{4.7}$$
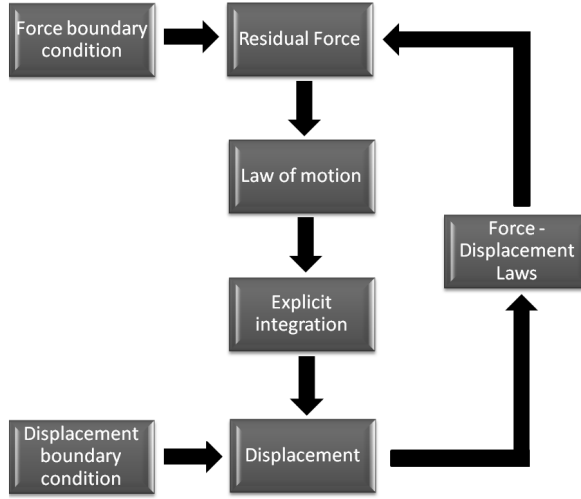
Figure 4.4. Scheme of a loop of discrete element algorithm

where accelerations, $\ddot{u}_i^n$, and positions, u_i^n and u_i^{n+1}, are defined at time instants t^n and t^{n+1} ($t^{n+1} = t^n + \Delta t$), while velocities, $\dot{u}_i^{n-1/2}$ and $\dot{u}_i^{n+1/2}$, are shifted by a half-step. Employing the formulae (4.6) and (4.7) for Eq. (4.1) the following time integration algorithm for the translational motion is obtained:

$$\ddot{u}_i^n = \frac{F_i^n}{m_i}, \tag{4.8}$$

$$\dot{u}_i^{n+1/2} = \dot{u}_i^{n-1/2} + \ddot{u}_i^n \Delta t, \tag{4.9}$$

$$u_i^{n+1} = u_i^n + \dot{u}_i^{n+1/2} \Delta t. \tag{4.10}$$

Analogously, the time integration scheme for the rotational equations of motion is obtained:

$$\dot{\boldsymbol{\omega}}_i^n = \frac{T_i^n}{J_i}, \tag{4.11}$$

$$\boldsymbol{\omega}_i^{n+1/2} = \boldsymbol{\omega}_i^{n-1/2} + \dot{\boldsymbol{\omega}}_i^n \Delta t, \tag{4.12}$$

$$\Delta \boldsymbol{\theta}_i = \boldsymbol{\omega}_i^{n+1/2} \Delta t. \tag{4.13}$$

Equations (4.8)–(4.13) give a new configuration at time instant t^{n+1}.

Below are presented the interaction models for powder compaction and sintering. In further considerations, in order to simplify the notation the indices i and ij of Eqs. (4.1)–(4.5) are omitted.

4.4 Contact interaction model for powder compaction

The first stage of a process of powder metallurgy is powder compaction, where a green body of a particulate material is formed. Powder compaction is modeled using the cohesionless contact model together with friction and an effect of thermal expansion. The rheological scheme of this model is shown in Fig. 4.5.
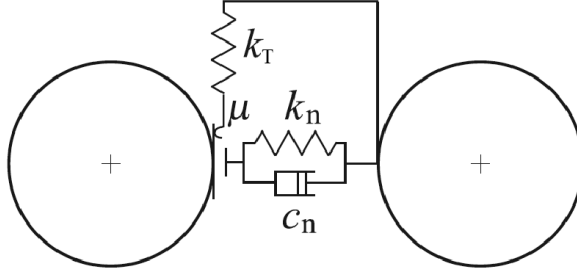
Figure 4.5. Rheological scheme of the contact interaction for powder compaction [164].

The normal contact interaction is represented by the Kelvin-Voigt element consisting of a spring and a dashpot connected in parallel. Additionally, a thermal element is added in series with a spring. The normal contact force F_n is a sum of the elastic force in the spring F_n^e and the viscous component F_n^d

$$F_n = F_n^e + F_n^d. \tag{4.14}$$

The elastic part of the normal contact force F_n^e can be evaluated assuming a linear force–displacement relationship:

$$F_n^e = k_n u_{rn}^e, \tag{4.15}$$

where k_n is the normal contact stiffness, u_{rn}^e is the penetration of the two particles, calculated as

$$u_{rn}^e = d_{ij} - r_i(T) - r_j(T), \tag{4.16}$$

where d_{ij} is the distance of the particle centres, and $r_i(T)$, $r_j(T)$ their radii dependent on the temperature, and given by the following relation:

$$r_a(T) = r_a^0(1 + \alpha \Delta T), \qquad a = i, j, \tag{4.17}$$

where α is the linear coefficient of the thermal expansion, ΔT is the temperature increment, and r_a^0 $(a = i, j)$ is the a-the particle radius at the initial (reference) temperature.

Alternatively, the elastic part of the normal contact force F_n^e can be presented in the form of the Hertz interaction model, which is the most classical nonlinear model used in particle collisions [165]:

$$F_\mathrm{n}^\mathrm{e} = k_\mathrm{n} u_\mathrm{rn}^{\mathrm{e}\ 3/2}. \tag{4.18}$$

From the Hertz theory for an elastic sphere i the normal stiffness can be expressed as [166]

$$k_\mathrm{n} = \frac{4}{3}\overline{E}\sqrt{\overline{r}}, \tag{4.19}$$

where $\overline{E}$ is the effective Young's modulus, which allows to consider two particles with various elastic properties. The effective Young's modulus is given by following relation:

$$\frac{1}{\overline{\overline{E}}} = \frac{1-\nu_i^2}{E_i} + \frac{1-\nu_j^2}{E_j}. \tag{4.20}$$

The effective radius of particle $\overline{r}$ can be expressed as

$$\overline{r} = \frac{2r_i(T)r_j(T)}{r_i(T) + r_j(T)}. \tag{4.21}$$

The viscous component of the normal force is assumed to be a linear function of the normal relative velocity v_rn

$$F_\mathrm{n}^\mathrm{d} = c_\mathrm{n} v_\mathrm{rn}, \tag{4.22}$$

where

$$v_\mathrm{rn} = (\dot{\mathbf{u}}_j - \dot{\mathbf{u}}_i) \cdot \mathbf{n}_i. \tag{4.23}$$

The value of the viscosity coefficient c_n can be taken as a fraction ξ of the critical damping C_{cr} for the system of two rigid bodies with masses m_i and m_j, connected with a spring of the stiffness k_n

$$c_\mathrm{n} = \xi C_\mathrm{cr}, \tag{4.24}$$

where the critical damping can be calculated as, cf. [167]:

$$C_\mathrm{cr} = 2\sqrt{\frac{m_i m_j k_\mathrm{n}}{m_i + m_j}}. \tag{4.25}$$

In the model of compaction no cohesion is allowed, so no tensile normal contact forces are allowed

$$F_\mathrm{n}^\mathrm{e} \leq 0. \tag{4.26}$$

The tangential reaction $\mathbf{F}_\mathrm{T}$ at the contact point is brought about by the friction opposing the relative motion. The relative tangential velocity at the contact point $\mathbf{v}_\mathrm{rT}$ is calculated from the following relationship

$$\mathbf{v}_\mathrm{rT} = \mathbf{v}_\mathrm{r} - \mathbf{v}_\mathrm{r} \cdot \mathbf{n}_i, \tag{4.27}$$

$$\mathbf{v}_\mathrm{r} = (\dot{\mathbf{u}}_j + \boldsymbol{\omega}_j \times \mathbf{s}^c_{ji}) - (\dot{\mathbf{u}}_i + \boldsymbol{\omega}_i \times \mathbf{s}^c_{ij}), \tag{4.28}$$

where $\dot{\mathbf{u}}_i$, $\dot{\mathbf{u}}_j$, and $\boldsymbol{\omega}_i$, $\boldsymbol{\omega}_j$ are the translational and rotational velocities of the particles, and $\mathbf{s}^c_{ij}$ and $\mathbf{s}^c_{ji}$ are the vectors connecting particle centres with contact points.

The regularized Coulomb friction model has been assumed in the current model instead of the standard Coulomb law, which due to possible changes of the direction of sliding velocity would produce non physical oscillations of the friction force. The relationship between the friction force $\|\mathbf{F}_\mathrm{T}\|$ and relative tangential u_rT displacement for the regularized Coulomb model (for a constant normal force F_n) is shown in Fig. 4.6.
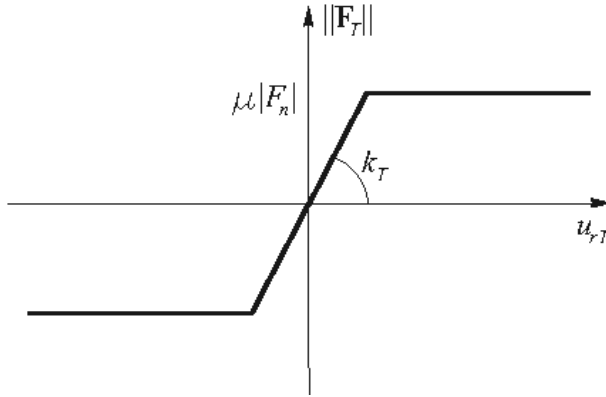
Figure 4.6. Friction force vs. relative tangential displacement for the regularized Coulomb friction model.

4.5 Contact interaction model for sintering

The most important and the most difficult to model stage of powder metallurgy process is sintering. Below, two models of sintering process implemented in the discrete element framework have been presented. The first model is the standard viscous model used by other authors, and the second one is the original thermo-viscoelastic model proposed in this work.

4.5.1 Viscous model of sintering

The viscous model of sintering has been taken from the literature and is based on the classical models developed at particle level [46, 168, 169] and used in previous implementations in the discrete element method, cf. [58, 59, 63]. The model of particle interaction during sintering must take into account cohesion between particles of a sintered material. The particle interaction during sintering is given by the equation derived considering mass transport and stresses at the grain boundary between two sintered particles, cf. [58, 59, 169]:

$$F_{\mathrm{n}} = \frac{\pi a^4}{8 D_{\mathrm{eff}}} v_{\mathrm{rn}} + \pi \gamma_S \left[4r \left(1 - \cos \frac{\Psi}{2} \right) + a \sin \frac{\Psi}{2} \right], \qquad (4.29)$$

where F_{n} is the normal force between two particles, v_{rn} – the normal relative velocity, r – the particle radius, a – the radius of the interparticle boundary, Ψ – the dihedral angle, γ_{S} – the surface energy and D_{eff} – the effective grain boundary diffusion coefficient. The geometrical parameters of the model are defined in Fig. 4.7. Similarly like in the formulation used in [59] the tangential force was not taken into account. This should favour particle rearrangements. The derivation of the Eq. (4.29) with special consideration of the relationship between sintering driving force, sintering stress, grain boundary diffusion and geometrical parameters is given in Appendix A.
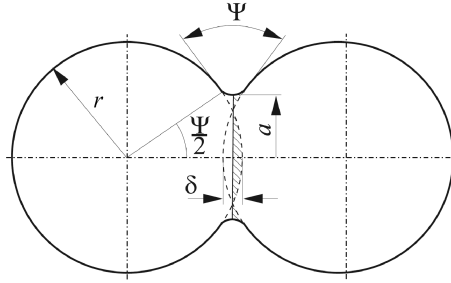
Figure 4.7. Two-particle model of sintering.

In the model of sintering, the initial particle boundary radius a_0 depends on the initial penetration u_{rn}^0, for instance induced by the compaction. From simple geometrical considerations we have

$$a_0 = \sqrt{\frac{r u_{\mathrm{rn}}}{2}}. \qquad (4.30)$$

The growth of the radius of the interparticle boundary is governed by the following evolution law:

$$\dot{a} = -\frac{r v_{\mathrm{rn}}}{a}. \tag{4.31}$$

The particle boundary radius a grows until the sintering process is stopped. Its maximum at the equilibrium state is given by the following geometric relationship:

$$a_{\max} = r \sin \frac{\Psi}{2}. \tag{4.32}$$

The model described by Eq. (4.29) has been derived for identical particles. Following [59] it can be generalized to sintering models of different size particles by replacing the radius r in Eqs. (4.29)–(4.32) with the equivalent particle radius $\bar{r}$ given by the following formula:

$$\bar{r} = \frac{2 r_i r_j}{r_i + r_j}. \tag{4.33}$$

On the right-hand side of Eq. (4.29) there are two terms, the first term has a character of viscous resistance to the particle approaching caused by the sintering attracting force represented by the second term. These force components will be denoted, $F_{\mathrm{n}}^{\mathrm{v}}$ and $F_{\mathrm{n}}^{\mathrm{sint}}$, respectively. Thus, Eq. (4.29) can be rewritten as follows:

$$F_{\mathrm{n}} = F_{\mathrm{n}}^{\mathrm{v}} + F_{\mathrm{n}}^{\mathrm{sint}}, \tag{4.34}$$

where

$$F_{\mathrm{n}}^{\mathrm{v}} = \frac{\pi a^4}{8 D_{\mathrm{eff}}} v_{\mathrm{rn}}, \tag{4.35}$$

$$F_{\mathrm{n}}^{\mathrm{sint}} = \pi \gamma_{\mathrm{S}} \left[4\bar{r} \left(1 - \cos \frac{\Psi}{2} \right) + a \sin \frac{\Psi}{2} \right]. \tag{4.36}$$

This decomposition of the interaction force for free sintering can be represented by the rheological scheme shown in Fig. 4.8.

4.5.2 Thermo-viscoelastic model of sintering

Thermo-viscoelastic model of sintering is introduced as an author's original extension of viscous model. The rheological model of sintering presented in Fig. 4.8 is enriched by adding elastic and thermal component. An addition of elastic part will allow to account better for material properties which are characterized with certain elasticity during sintering, as well. The elastic component will allow to better redistribute forces in the particle assembly with large
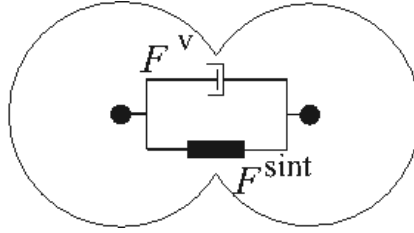
Figure 4.8. Rheological scheme of the viscous model of free sintering.

changes of configuration during sintering. Seeing an analogy of a sintered material with a fluid, whose viscoelastic properties are commonly modeled with the viscoelastic Maxwell model, the elastic component in series with the viscous element is introduced. Furthermore the rheological model includes the thermal component ensuring the thermal effects occurring during temperature evolution, for example thermal expansion or thermal stresses. In this way the rheological scheme presented in Fig. 4.9 is obtained.
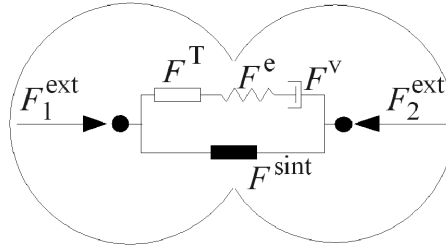
Figure 4.9. Rheological scheme of the thermo-viscoelastic model of sintering under pressure.

For the Maxwell element we have the following relationships for forces and velocities:

$$F_n^v = F_n^e = F_n^T, \tag{4.37}$$

$$v_{rn} = v_{rn}^v + v_{rn}^e + v_{rn}^T. \tag{4.38}$$

Equation (4.37) means that the forces transferred through the spring, viscous and thermal component, F_n^e, F_n^v and F_n^T, respectively, are equal. Equation (4.38) expresses the additive decomposition of the relative normal velocity between particles v_{rn} into the elastic, viscous and thermal parts, v_{rn}^e, v_{rn}^v and v_{rn}^T respectively.

The viscous force is given by Eq. (4.35), which can be rewritten in the form:

$$F_n^v = \eta v_{rn}^v, \tag{4.39}$$

where

$$\eta = \frac{\pi a^4}{8 D_{\text{eff}}}.$$ (4.40)

The elastic interaction of the normal contact force F_{n}^{e} can be presented in the form of the linear relationship:

$$F_{\text{n}}^{\text{e}} = k_{\text{n}} \left(u_{\text{rn}}^{\text{e}} + u_{\text{rn}}^{T} \right),$$ (4.41)

or in the form of the Hertz interaction model:

$$F_{\text{n}}^{\text{e}} = k_{\text{n}} \left(u_{\text{rn}}^{\text{e}} + u_{\text{rn}}^{T} \right)^{3/2}.$$ (4.42)

The second component of the relative normal displacement, u_{rn}^{T}, results from the effect of the linear thermal expansion and is given by relation:

$$u_{\text{rn}}^{T} = r \alpha \Delta T.$$ (4.43)

Substituting Eqs. (4.39) and (4.41) into (4.38) we obtain the evolution equation for the force in the Maxwell system

$$v_{\text{rn}} = \frac{\dot{F}_{\text{n}}^{\text{e}}}{k_{\text{n}}} + \frac{F_{\text{n}}^{\text{v}}}{\eta}.$$ (4.44)

In the case of the application of Hertz model, the Eq. (4.44) takes a form

$$v_{\text{rn}} = \frac{\dot{F}_{\text{n}}^{\text{e}}}{k_{\text{n}}^{\text{eff}}} + \frac{F_{\text{n}}^{\text{v}}}{\eta},$$ (4.45)

where $k_{\text{n}}^{\text{eff}}$ is the effective normal stiffness resulting from the integration of Eq. (4.42), and given by the following expression

$$k_{\text{n}}^{\text{eff}} = \frac{3}{2} k_{\text{n}} \left(\dot{u}_{\text{rn}}^{\text{e}} + \dot{u}_{\text{rn}}^{T} \right).$$ (4.46)

Following Martin et al. [59] the rotational motion of the particles and tangential interaction has been neglected in the present formulation of sintering. This should be favorable for particle rearrangements.

4.6 Transition between Kelvin-Voigt and Maxwell models

In the investigated process, the different material behaviour changing in time is studied. During powder compaction the material has a solid-like behaviour while during sintering it attains fluid-like behaviour. A certain analogy to this change of properties can be seen in solid-liquid transitions occurring during melting [170] or in polymers undergoing the glass transition [171–173].

According to the main characteristics of the material different viscoelastic models have been adopted here for the two types of material behaviour of powder material during the manufacturing process involving pressing and sintering. Granular material during pressing is modeled by the Kelvin-Voigt element (Subsec. 4.4), which is better suited to describe the nature of a solid material. The irreversible flow during sintering is represented better using the model with the nonlinear Maxwell element presented in Subsec. 4.5.2.

Transition from the solid-like to fluid-like behavior and simultaneous change of the model type are associated with a sharp change of viscoelastic properties. In order to smoothen the transition, a gradual smooth change of parameters at a certain time interval $(t_0, t_0 + t_{\mathrm{rel}})$ is introduced, where t_0 is the time when sintering is initiated. At this interval the viscosity coefficient η in the Maxwell element changes according to the following function:

$$\eta = \eta_\infty (1 - \zeta) + \zeta \eta_{\mathrm{teor}}, \tag{4.47}$$

where η_∞ is the viscosity coefficient in the Maxwell element before sintering, η_{teor} is the theoretical viscosity calculated according to the Eq. (4.40), and $\zeta \in \langle 0, 1 \rangle$ is a coefficient ensuring gradual change of η from η_∞ at $t = t_0$ to η_{teor} at $t = t_0 + t_{\mathrm{rel}}$. The smooth transition is obtained by the definition of ζ:

$$\zeta = \frac{1 - \cos \varphi}{2}, \tag{4.48}$$

where

$$\varphi = \frac{t - t_0}{t_{\mathrm{rel}}} \pi, \qquad t \in \langle t_0, t_0 + t_{\mathrm{rel}} \rangle. \tag{4.49}$$

If we assume that the Maxwell element is used before sintering when an elastic material is concerned, its viscosity coefficient would have a very high value. In the model this value is prescribed arbitrarily taking a certain value based on numerical tests.

In order to avoid step-type loading the sintering force is also scaled with a smoothly increasing function from 0 to 1 at the time interval $\langle t_0, t_0 + t_{\mathrm{rel}} \rangle$:

$$F^{\mathrm{sint}} = \zeta F^{\mathrm{sint}}_{\mathrm{teor}}, \tag{4.50}$$

where ζ is defined by Eq. (4.48) and $F_{\text{teor}}^{\text{sint}}$ is evaluated according to Eq. (4.36). If simulation of the process is continued after the condition of equilibrium given by Eq. (4.32) is achieved, a sharp change of properties also occurs. The Maxwell model is being used, but properties are changed by setting a higher value of the viscosity parameter η and setting to zero the sintering force F^{sint}. In order to smoothen the changes of the model parameters, a similar scaling of the viscosity coefficient and the sintering force at a certain time interval after the end of sintering is applied:

$$\eta = \zeta'\eta_\infty + (1 - \zeta')\eta_{\text{teor}}, \tag{4.51}$$

$$F^{\text{sint}} = (1 - \zeta')F_{\text{teor}}^{\text{sint}}, \tag{4.52}$$

with

$$\zeta' = \frac{1 - \cos\varphi'}{2}, \tag{4.53}$$

where

$$\varphi' = \frac{t - t_{\text{end}}}{t_{\text{rel}}}\pi, \qquad t \in \langle t_{\text{end}}, t_{\text{end}} + t_{\text{rel}}\rangle \tag{4.54}$$

and t_{end} is the time when the condition of equilibrium given by Eq. (4.32) is achieved.

4.7 Time integration scheme

Proposed model uses a typical time integration scheme of discrete element modeling – an explicit central difference type algorithm. In order to pass to the next step the forces at this configuration must be evaluated. First step in calculation of force interactions in sintering for both presented models is updating the radius of the interparticle boundary according to the evolution law given by Eq. (4.55), which is considered at the midpoint at time instant $t^{n+1/2}$

$$\dot{a}^{n+1/2} = -\frac{r v_{rn}^{n+1/2}}{a^{n+1/2}}, \tag{4.55}$$

in which the following central difference schemes has been employed:

$$\dot{a}^{n+1/2} = \frac{a_{n+1} - a_n}{\Delta t}, \tag{4.56}$$

$$a^{n+1/2} = \frac{a_{n+1} + a_n}{2}. \tag{4.57}$$

The new radius a_{n+1} can be solved in terms of known parameters as:

$$a^{n+1} = \sqrt{a_n^2 - 2rv_{rn}^{n+1/2}\Delta t}. \tag{4.58}$$

In the convention adopted the relative velocity in sintering process is negative so the second term under square root in Eq. (4.58) is positive.

The viscous part of the interaction force in the viscous model is computed taking Eq. (4.35) at time instant $t^{n+1/2}$

$$(F^v)^{n+1/2} = \eta^{n+1/2}v_{rn}^{n+1/2}. \tag{4.59}$$

Using the midpoint rule

$$(F^v)^{n+1/2} = \frac{(F^v)^{n+1} + (F^v)^n}{2} \tag{4.60}$$

the expression for the viscous resistance at time instance t^{n+1} has been obtained

$$(F^v)^{n+1} = 2\eta^{n+1/2}v_{rn}^{n+1/2} - (F^v)^n. \tag{4.61}$$

For the thermo-viscoelastic sintering model with the linear model of elastic interaction Eq. (4.44) is considered at the time instant $t^{n+1/2}$:

$$v_{rn}^{n+1/2} = \frac{(\dot{F}_n^e)^{n+1/2}}{k_n} + \frac{(F_n^v)^{n+1/2}}{\eta^{n+1/2}}. \tag{4.62}$$

Substituting the following finite difference expressions:

$$(\dot{F}_n^e)^{n+1/2} = \frac{(\dot{F}_n^e)^{n+1} - (\dot{F}_n^e)^n}{\Delta t} = \frac{\Delta F_n^e}{\Delta t}, \tag{4.63}$$

$$(F_n^e)^{n+1/2} = (F_n^e)^n + \frac{\Delta F_n^e}{2} \tag{4.64}$$

into Eq. (4.62) we obtain:

$$v_{rn}^{n+1/2} = \frac{\Delta F_n^e}{k_n\Delta t} + \frac{(F_n^e)^n + \dfrac{\Delta F_n^e}{2}}{\eta^{n+1/2}}. \tag{4.65}$$

From Eq. (4.65) the expression for the incremental and total forces in the Maxwell element is obtained:

$$\Delta F_n^e = \frac{v_{rn}^{n+1/2}\Delta t - \dfrac{(F_n^e)^n\Delta t}{\eta^{n+1/2}}}{\dfrac{1}{k_n} + \dfrac{\Delta t}{2\eta^{n+1/2}}}, \tag{4.66}$$

$$(F_n^{\text{e}})^{n+1} = (F_n^{\text{e}})^n + \Delta F_n^{\text{e}} = \frac{v_{rn}^{n+1/2}\Delta t + (F_n^{\text{e}})^n \left(\dfrac{1}{k_n} - \dfrac{\Delta t}{2\eta^{n+1/2}}\right)}{\dfrac{1}{k_n} + \dfrac{\Delta t}{2\eta^{n+1/2}}}. \tag{4.67}$$

In case of the application of the non-linear Hertz model, we take the Eq. (4.45) and follow the procedure from Eq. (4.63) to (4.67).

The integration scheme given by Eq. (4.67) corresponds to the trapezoidal or two-stage Lobatto IIIA method of integration [174]. Other possible integration methods of the viscoelastic Maxwell model can be found in [174].

4.8 Numerical stability

Explicit time integration scheme given by Eqs. (4.8)–(4.10) is characterized by a high efficiency of the solution at each time step. The equations are decoupled and there is no need to solve a system of algebraic equations or perform iterations. The known drawback of the explicit time integration scheme is its conditional numerical stability which imposes the limitation on the time step Δt, i.e.

$$\Delta t \le \Delta t_{\text{cr}}, \tag{4.68}$$

where Δt_{cr} is the critical time step. For a system of two masses m connected by a spring with the stiffness k the critical time step is given by:

$$\Delta t_{\text{cr}} = \frac{2}{\omega_{\text{max}}}, \tag{4.69}$$

where

$$\omega_{\text{max}} = \sqrt{\frac{2k}{m}} \tag{4.70}$$

is the angular eigenfrequency of the considered system.

The critical time for the system of two masses m connected by a Kelvin element (a spring k in parallel with a damper c) corresponding to two particles during compaction is given by

$$\Delta t_{\text{cr}} = \frac{2}{\omega_{\text{max}}}(\sqrt{1 + \xi^2} - \xi), \tag{4.71}$$

where ξ is the damping ratio introduced in Eq. (4.24).

The critical time step for the system of two masses m connected with a damper with the viscosity η is determined from the following formula:

$$\Delta t_{\mathrm{cr}} = \frac{2m}{\eta}. \tag{4.72}$$

The stability of discrete systems with Maxwell elements has been studied in [175]. The critical step for the system of two masses m connected by a Maxwell element consisting of a spring with the stiffness k and a damper with the viscosity η can be evaluated in a simple way, cf. [176], as the minimum

$$\Delta t_{\mathrm{cr}} = \min\{\tau_{\omega_{\max}}, \tau_{\mathrm{Mr}}\} \tag{4.73}$$

of the critical time step $\tau_{\omega_{\max}}$ resulting from undamped vibrations with the angular frequency $\omega_{\max}$ determined from Eq. (4.69)

$$\tau_{\omega_{\max}} = \frac{2}{\omega_{\max}} \tag{4.74}$$

and the Maxwell relaxation time τ_{Mr} defined as:

$$\tau_{\mathrm{Mr}} = \frac{\eta}{k}. \tag{4.75}$$

Evaluation of the critical time step for a multi-body discrete system requires the consideration of the whole set of differential equations. This is not efficient for large models of discrete elements, therefore simpler methods to calculate the stability limit are necessary [177]. In practice, the critical time step in discrete element models is taken as the minimum of the values obtained for all the connections considered separately and multiplied by a certain safety factor β

$$\Delta t \leq \beta \Delta t_{\mathrm{cr}}, \tag{4.76}$$

where $0 < \beta < 1$. The value of β has been studied by different authors. A good review can be found in [177], where the value close to 0.17 is recommended for a 3D simulation and 0.3 – for a 2D case.

The drawback of time step limitation can be mitigated by scaling of model parameters which is described in the next subsection.

4.9 Scaling of discrete element model parameters

Along with a great potential, such as an ability to model individual particles of a granular system, the DEM has a serious drawback associated with the model size and time step limitation. In general, number of powder particles in a real physical/experimental specimen may achieve even billions, therefore a DE model cannot account for all individual particles contained in the system due to insufficient currently available computer resources. A reduction of the size of the DE model can be achieved by scaling of discrete element model, which employs the so-called "scaling-up" the element sizes (the domain size remains the same) or the "scaling-down" the domain size (particles size remains the same). Furthermore scaling of model parameters can be performed. Scaling can significantly reduce the computation time, but it can be used very cautiously in order to preserve the true physical behaviour of the system.

The principles of model scaling, called *similarity principles*, in the DEM have been discussed in detail in [178]. Similarity principles consider the relationship between the scaled and original model and establish terms of application of scaled model and its accuracy in respect to original one. According to the main idea of the similarity principles, two models (scaled and original) can be named fully similar if the relationship between homogeneous physical quantities is constant at the all corresponding points of models domain. Scaled model can exactly represent the behaviour of the original physical model, when the following three similarity principles are satisfied:

- **geometric** – the ratio of particle radii (r', r) and domain sizes (D'_{m}, D_{m}) of scaled and original model respectively, are constant:

$$\frac{r'}{r} = \frac{D'_{\mathrm{m}}}{D_{\mathrm{m}}} = \alpha_s \tag{4.77}$$

  and the particle packing configurations in both models shall be identical [178];

- **mechanical** – the particle strains (ϵ', ϵ), stresses (σ', σ) and strain energy functions (e', e) are identical [178]:

$$\epsilon' = \epsilon, \qquad \sigma' = \sigma, \qquad e' = e; \tag{4.78}$$

- **dynamic** – all the forces – inertial ($m'\ddot{\mathbf{u}}'$, $m\ddot{\mathbf{u}}$), contact ($F^{\mathrm{c}\prime}$, F^{c}) and external ($F^{\mathrm{ext}\prime}$, F^{ext}) acting on particles shall be in the same ratio [179].

$$\frac{m'\ddot{\mathbf{u}}'}{m\ddot{\mathbf{u}}} = \frac{F^{\mathrm{c}\prime}}{F^{\mathrm{c}}} = \frac{F^{\mathrm{ext}\prime}}{F^{\mathrm{ext}}}. \tag{4.79}$$

In the present work, scaling is employed without full preservation of the similarity principles. First of all, the domain size is scaled down with simultaneous application of the original size of particles and packing configurations. In this case, the principle of geometric similarity (according to Eq. (4.77)) is not satisfied, nevertheless it has been assumed that such reduced geometric model represent correctly the powder metallurgy process. This approach has been applied to avoid the necessity of scaling other model parameters, i.e. relative rates of sintering by the different mechanisms [180], and give an ability to study the phenomenon of sintering process at the original scale, which is commonly performed in a several studies of discrete element modeling of sintering process [59, 63, 65, 69, 70]. From the other hand, given assumption has its limitations - it excludes the modeling of heat transfer (isothermal process) or density distribution of studied domain (specimen).

The DEM simulations in the present work have been performed employing also mass scaling to overcome the efficiency problem due to time step limitation imposed by the stability condition of the explicit time integration scheme. The values of critical time steps are usually relatively small, so simulation with an explicit time integration usually requires the use of large number time steps. Therefore, this approach is most suitable for transient and high-speed problems. Simulation of longer and slow processes such as sintering would be too expensive. A possible way around consists in artificial density or mass scaling in order to increase the critical time step

$$\frac{m'}{m} = \alpha_m, \tag{4.80}$$

where m is the real mass, α_m is the mass scaling factor and m' is the scaled mass. This method is widely used in explicit finite element simulations [181] as well as in the discrete element analyses [182, 183].

In general, scaling of equations describing different physical phenomena is performed in such a way that the similarity between the original and scaled models defined by certain dimensionless numbers is satisfied [184]. It can be noticed that the mass scaling performed according to Eq. (4.80) with other quantities unchanged does not ensure the dynamic similarity governed by the ratio of the inertial to viscous forces. However, it is assumed that inertial effects (inertial terms in equations of motion) in the considered problem are so small that even a large scaling of mass and the resulting increase in the inertial terms will not significantly affect the solution. The value of the scaling factor depends on the problem. It is indicated in [183] that mass can be scaled by factors greater than 10^{10} in quasi-static DEM simulations. Sintering processes are very slow and time steps allowed in explicit simulation are very short because of

small particle inertia [64]. Sintering can be analysed efficiently only employing a scaling procedure in the discrete element model. It has been shown in [64] that the particle inertia in a DEM sintering model can be scaled by several orders of magnitude without affecting particle positions. The DEM solution with mass scaling has been verified there by comparison with the solution obtained assuming the zero inertial terms in the governing equations. Similarly, in this work, mass scaling is used. The effect of scaling and correctness of the solution is verified by comparing the solutions with different mass scaling. The convergence of the scaled solution to the solution with real parameters proves that scaling is acceptable.

4.10 Determination of material parameters of sintering model

In the numerical modeling of materials, the estimation of material model parameters is one of the major tasks and frequently causes many difficulties. From the numerical point of view it is important to identify and select appropriate values of the parameters required to obtain correct results. In the case of modeling of sintering, the material model parameters determination is a problematic issue, because of the complexity of the entire process, which is linked to many kinds of phenomena from mechanics of single atoms to thermodynamics of whole system. Furthermore, the determination of material model parameters seems to be a crucial issue due to its influence on the results of the numerical simulation. An inappropriate evolution of material parameters of sintering model, such as diffusive coefficients, may highly affect the simulation kinetics (densification, shrinkage) and microstructural processes (the growth of the cohesive necks).

In order to satisfy this particular requirement, the literature study of the material parameters of the thermo-viscoelastic model of sintering has been performed. Relations to estimate the values of all required material model parameters were proposed. The analysis concerns the determination of diffusive parameters, as the main mass transport mechanisms of the sintering process assumed for the current model, and surface energy as the sintering driving force of particle attraction.

Diffusive parameters

The values of diffusive parameters directly depend on certain diffusion mechanism, which is considered at the constitutive model of sintering. In the presented thesis, the constitutive model of sintering was obtained from the analysis of the mechanism of the grain boundary diffusion [58], where the effective grain boundary diffusion coefficient D_{eff} is given by the following formula:

$$D_{\text{eff}} = \frac{D_{\text{gb}}\delta\Omega}{k_{\text{B}}T}, \tag{4.81}$$

where D_{gb} is the grain boundary diffusion coefficient with the width δ, Ω is the atomic volume, k_{B} is the Boltzmann constant and T is the temperature.

The atomic volume Ω is a parameter indicating a volume of one gram of a material in normal conditions. The parameter is obtained from the quotient of the atomic mass m_{a} and theoretical density of a material ρ_{theo}:

$$\Omega = \frac{m_{\text{a}}}{\rho_{\text{theo}}}. \tag{4.82}$$

The major diffusive parameter determining the kinetics of sintering process is the grain boundary diffusion coefficient D_{gb} given by the Arrhenius-type equation [185]:

$$D_{\text{gb}} = D_{\text{0gb}}\exp\left[-\frac{\Delta H_{\text{gb}}}{RT}\right], \tag{4.83}$$

where D_{0gb} is the pre-exponential factor of grain boundary diffusion, ΔH_{gb} is the activation enthalpy of grain boundary diffusion, R is the gas constant.

The pre-exponential factor D_{0gb} is not very much different from those of lattice diffusion D_0 [185], which is expressed as:

$$D_0 = D_0{}'\exp\frac{\Delta S}{R}, \tag{4.84}$$

where ΔS is the diffusion entropy (ranges from 1 to several R) and D_0' contains geometric factors, the correlation factor, the lattice parameter squared, and an attempt frequency of the order of the Debye frequency [186]. The form of pre-exponential factor D_0' depends on the diffusion mechanism. During the sintering process, atoms change their location via the vacancy mechanism of self-diffusion, which is the most basic diffusion process for grain boundaries [185]. The pre-exponential factor D_0' in self-diffusion takes form [186]:

$$D_0' = f\nu_{\text{D}}\lambda^2. \tag{4.85}$$

To calculate the parameter D_0', the following parameters have to be determined:

- The Debye frequency ν_{D} is a theoretical maximum frequency of vibration for the atoms that make up the crystal [187]. The Debye frequency in solids usually ranges between $10^{13} - 10^{14}$ Hz and it can be determined from Eq. (4.86):

$$\nu_{\text{D}} = \nu_{\text{s}}\left[\frac{3N_{\text{a}}}{4\Pi V_{\text{u}}}\right]^{1/3}, \tag{4.86}$$

where ν_s is the speed of sound, N_a is the number of atoms in the unit cell and V_u is the volume of unit cell.

- Lattice parameter λ is given by various formula for different types of crystal system. For the most two popular crystal systems: Face-centered cubic FCC (for example cooper – Cu) and Body-centered cubic BCC (intermetallic NiAl), lattice parameters depend on an atomic radius r_{at}, and can be calculated from the following formulas [188]:

$$\text{FCC} - \lambda_{Cu} = \frac{4r_{at}}{\sqrt{2}},$$

$$\text{BCC} - \lambda_{NiAl} = \frac{4r_{at}}{\sqrt{3}}.$$

- Correlation factor f depends on the crystal unit cell. For monovacancies in cubic lattices f is a temperature-independent quantity, which is approximately given by:

$$f \approx 1 - \frac{2}{Z}, \tag{4.87}$$

where Z is the coordination number. According to [189], exact values of correlation factor f are listed in Table 4.1.

Table 4.1. Correlation factors of vacancy-mediated self-diffusion in cubic lattices [186].

Structure	fcc	bcc	sc	Diamond
f	0.7815	0.727	0.653	0.5

Finally, comparing Eqs. (4.83), (4.84) and (4.85), we obtain the relation of grain boundary diffusion coefficient D_{gb} with its all component:

$$D_{gb} = f\nu_D\lambda^2\exp\left[\frac{\Delta S}{R}\right]\exp\left[-\frac{\Delta H_{gb}}{RT}\right]. \tag{4.88}$$

The enthalpy of activation ΔH_{gb} appearing in Eq. (4.88) is defined as a minimum energy needed to create or change the thermodynamic system. It plays a major role in the diffusivity characterization, which is closely related to the type of diffusion. Following Mehrer [185], the relation between the enthalpy of activation of bulk diffusion ΔH, grain boundary diffusion ΔH_{gb} and surface diffusion ΔH_s and their equivalent diffusion coefficients can be stated as follows:

$$\Delta H > \Delta H_{gb} > \Delta H_s, \tag{4.89}$$

$$D \leq D_{gb} \leq D_s. \tag{4.90}$$

Coefficients of grain boundary diffusion (D_{gb}, ΔH_{gb}) lie between those for bulk diffusion (high enthalpy of activation ΔH, low diffusivity D) and surface diffusion (low enthalpy of activation ΔH_s, high diffusivity D_s) [190]. Typically, grain boundary diffusion in metals is four to six orders of magnitude faster than bulk diffusion. For metals, the ratios of activation enthalpies of bulk and grain boundary self-diffusion, $\Delta H_{gb}/\Delta H$, lie between 0.4 and 0.6 [185].

In literature several works concerning determination of the enthalpy of activation of various materials, either for metals [191] and intermetallics [192, 193] can be found. A more comprehensive analysis of grain- and interphase boundary diffusion data for metals were brought by Gust et al. [194, 195]. Studies refering to empirical correlations between grain boundary self-diffusion properties for different crystal systems were derived either by Brown and Ashby [196] or Gust et al. [197] (Table 4.2).

Table 4.2. Empirical correlation between grain boundary self-diffusion for different crystal systems, and the melting temperature T_m [196, 197]. For the grain boundary width the value of $\delta = 0.5$ nm was assumed.

Structure	Brown and Ashby [196]		Gust et al. [197]	
	D_{0gb} [m^{2}s^{-1}]	ΔH_{gb} [Jmol^{-1}]	D_{0gb} [m^{2}s^{-1}]	ΔH_{gb} [Jmol^{-1}]
fcc	$1.89 \cdot 10^{-5}$	$83.0 \cdot T_t[K]$	$1.94 \cdot 10^{-5}$	$74.4 \cdot T_t[K]$
bcc	$0.67 \cdot 10^{-3}$	$97.6 \cdot T_t[K]$	$1.84 \cdot 10^{-5}$	$86.7 \cdot T_t[K]$
hcp	$0.55 \cdot 10^{-4}$	$89.8 \cdot T_t[K]$	$1.94 \cdot 10^{-5}$	$85.4 \cdot T_t[K]$

The grain boundary width δ taken to the presented considerations with the value of 0.5 nm, suggested by Fisher [198], proved to be a good assumption. The following value is consistent with the determinations of δ by a high-resolution electron microscopy and other techniques [199].

Surface energy and dihedral angle

One of the major driving forces for densification during sintering is the change in free energy from the decrease in surface area and lowering of the surface free energy by the replacement of solid-vapour interfaces [200]. The forces must balance at the junction where the surfaces of the pores meet the particle boundary (Fig. 4.10). They are normally represented by the tension in the interface, i.e., the tension in the solid–vapor interface γ_s (surface energy) and the tension in the grain boundary γ_{gb} (grain boundary energy). At the junction the tension in the solid–vapor interface is tangential to that interface, while that in the grain boundary is in the plane of the boundary [3]. The balance of forces leads to

$$\gamma_{\mathrm{gb}} = 2\gamma_{\mathrm{s}} \cos \frac{\Psi}{2}, \tag{4.91}$$

where Ψ is the dihedral angle.

The dihedral angle can be determined only by interfacial energies and is independent of the pressures in the phases [201]. This means that the dihedral angle is constant, irrespectively of the pressure of the vapour phase, where Ψ is larger than 120°, because γ_{s} is usually higher than γ_{gb}. In general, γ_{s} is 2–3 times higher than γ_{gb} and Ψ is around 150°[202].
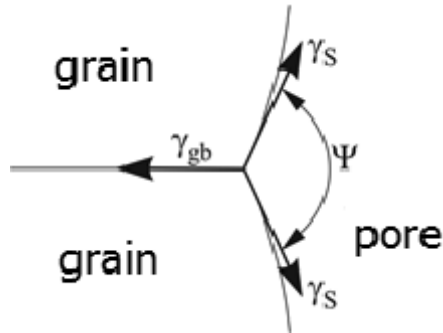
Figure 4.10. The equilibrium state of the pores in polycrystalline solids with the balance of the surface and grain boundary energy.

To determine the value of dihedral angle of the specific material, the surface γ_{s} and grain boundary energy γ_{gb} should be calculated. It should be noticed that the estimation of surface and grain boundary energies can be held for the single particle, thus the final result of the study of surface energy of policrystalline material will be a statistic representation of these parameters.

Generally, the determination of the surface energy is performed via the experimental measurements [203, 204], however there are several models concerning calculations of the surface energy of metals either from first-principles (density functional theory) [205–207] or by semi-empirical methods [208]. Despite serious difficulties and the complexity of many techniques and models, the surface energy can be estimated by at fairly simple relation proposed by Kislyi and Kuzenkova [209], which is based on the Herring's relation [180]

$$\gamma_{\mathrm{s}} \geq \frac{Gb}{4\pi(1-\nu)}, \tag{4.92}$$

where G is the shear modulus, b the Burgers vector and ν the Poisson's ratio.

The second parameter needed to be calculated is the grain boundary energy γ_{gb}. It is dominated by the combination of surface energies due to the force

balance on the junction of particles. The grain boundary energy results from mismatch between atoms across the boundary. Similarly to the surface energy, the grain boundary energy is hard to calculate and generally it can be determined via the experimental, numerical and analytical approaches. The experimental measurements of γ_{gb} are performed using similar techniques as γ_s. The measurement of dihedral angles at triple lines is the most useful and popular method, however in the literature more sophisticated approaches can be found [210]. Theoretical values of grain boundary energy can be computed by the numerical modeling using molecular statics or molecular dynamics [211, 212]. The analytical description of grain boundary energy depends on the type of grain boundary – low or high angle. Although the structure of the low angle grain boundaries is reasonably well understood, much less is known about the structure of the high angle grain boundaries, which are dominant in the policrystalline assembly [213]. The character of the high angle grain boundary is governed by several phenomenona and depends on many factors. Calculation of the energy of such boundary required sophisticated tools, such as the computer modeling, to take into account the specifics of material defects [214, 215]. Based on the literture studies it can be stated that the typical values of grain boundary energies of metals vary from 0.32 Jm^{-2} for Al to 0.87 for Ni Jm^{-2} [216].

Summary

The original numerical model of powder technology process has been formulated and implemented within the discrete element framework. The developed model considers the initial compaction of the powder, further consolidation as the effect of sintering, and finally the cooling stage.

The interaction of powder particles at the compaction stage is represented by the Kelvin-Voigt element, and at the sintering stage – by the Maxwell element combined in parallel with an active element producing sintering driving force. The standard viscous sintering model used by other authors, cf. [58], has been enriched by adding a spring and thermal element connected in series to the viscous rheological element, which allows to account for elastic deformation and thermal expansion. In order to smoothen the transition between the compaction (Kelvin-Voigt model) and sintering stage (Maxwell model), a gradual smooth change of parameters is enabled.

The explicit time integration algorithms of the equations of motion and constitutive relationships have been presented. The conditional stability of the algorithms has been indicated. Possibilities of increasing the computational efficiency by scaling of some model parameters have been discussed.

Additionally, the literature studies of the material parameters of the sintering model have been performed. The aim of the analysis was to determine the relations of sintering material parameters referring to diffusion and surface tension, which highly affect the sintering process kinetics.

The model presented in this section will be used in Sec. 5 to simulate powder metallurgy processes. The numerical model will be verified and validated. The results obtained with this model will be used in the stress analysis performed in Sec. 6.

Numerical simulation
of powder metallurgy process

Introduction

This section presents numerical results of simulation of powder metallurgy and sintering process obtained with the discrete element model described in Sec. 4. First, a simple test of sintering of two copper particles has been carried in order to verify the new viscoelastic model and compare its performance with that of the standard viscous model. The results of the studies on performance and efficiency of two particle models have been presented in [130]. Then, the thermo-viscoelastic model has been applied to simulation of hot pressing processes of pure NiAl, pure Al_2O_3 and NiAl-Al_2O_3 composite materials which were studied experimentally in Sec. 3. A part of the experimental results have been used to tune model parameters and the other part for its validation. Material phenomenon occurring during simulations of powder processing, such as shrinkage of the material, porosity decreasing, interaction and rearrangement of particles, have been analyzed in numerical simulation.

5.1 Simulation of two particle sintering

5.1.1 Simulation of free sintering

Free sintering of two copper particles of 22.5 µm at temperature 1300 K has been simulated using the material model parameters given in Table 5.1 taken from [58].

The problem has been analysed using both the viscous and viscoelastic models presented in Sec. 4. Figure 5.1 shows the particles before and after sintering.

The purpose of this numerical test was to: (i) verify performance of the model for an elementary system, (ii) investigate possibilities to increase efficiency of simulation by mass scaling, (iii) compare results obtained using the viscous

Table 5.1. Material data for copper sintering ($T = 1300$K) according to [58].

Material constant	Parameter value
Diffusion coefficient, $D_{\mathrm{gb}}\delta$	$3.832 \cdot 10^{-19}$ m^3/s
Atomic volume, Ω	$1.18 \cdot 10^{-29}$ m^3
Surface energy γ_s	1.72 J/m^2
Dihedral angle Ψ	146°
Density, ρ_{theo}	8920 kg/m^3

a)   b)
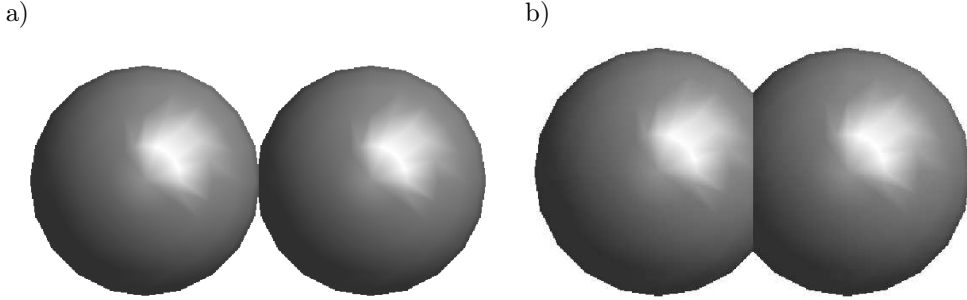
Figure 5.1. Simulation of sintering of two particles: a) initial configuration, b) end of sintering.

and viscoelastic models, (iv) compare efficiency of the viscous and viscoelastic model, and (v) determine macroscopic density evolution assuming a regular particle assembly and compare it with experimental results from [217].

Simulation of free sintering by means of the viscous model

Figures 5.2–5.6 show results obtained using the viscous model. Figure 5.2 presents displacement and velocity curves as functions of time for different mass scaling factors (up to 10^{12}). The displacements plotted in Figs. 5.2a and 5.2b are normalized with respect to the particle diameter. No differences between the solutions in Fig. 5.2a are visible. The differences can be observed in the displacements and velocities in a very short initial stage (Figs. 5.2b and 5.2c). Except for this initial period, the displacements for different mass scaling practically coincide. The displacements at the initial stage are small and not significant when compared to the total displacements during sintering. This proves that mass scaling factors employed in the analysis are acceptable.
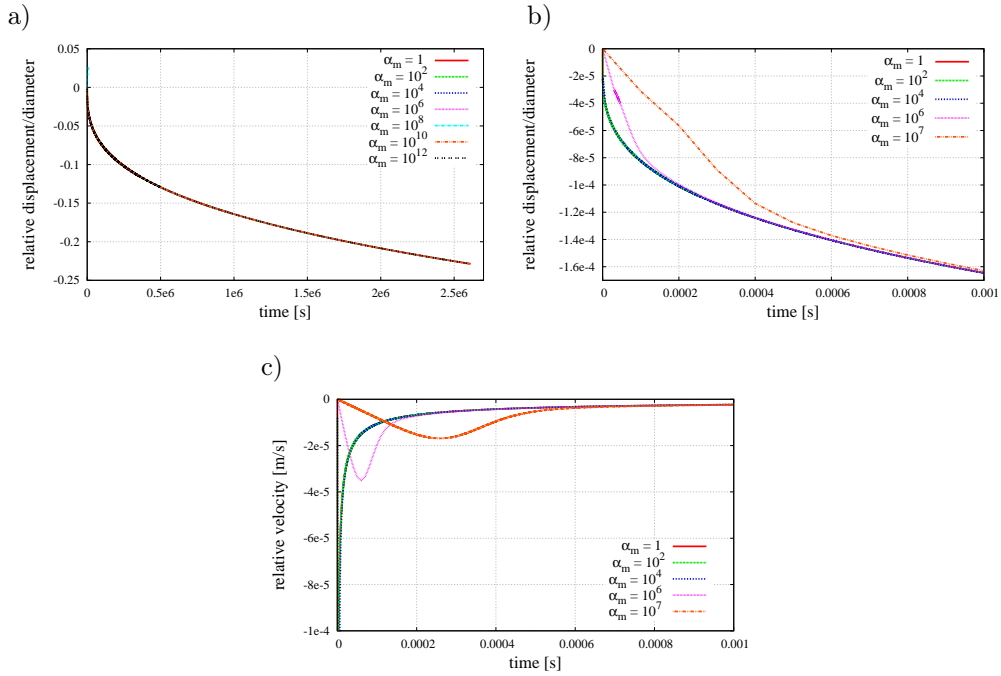
Figure 5.2. Simulation of sintering of two particles using the viscous model: a) relative displacement, b) relative displacement at the initial stage, c) relative velocity at the initial stage – effect of mass scaling.

Figure 5.3 presents evolution of the viscosity coefficient η calculated according to Eq. (4.40). It can be seen that the value of η is growing. This is caused by the growth of the neck. Growth of η will result in larger viscous resistance. The viscous resistance and sintering forces are plotted as functions of time in Figs. 5.4 and 5.5 for the whole sintering process and for the initial stage of sintering, respectively.

It can be observed that initially the sintering force has a higher value and this explains a fast increase of absolute value of relative velocity at this time which is shown in Fig. 5.6. The viscous resistance is growing due to the increase of the velocity and viscosity. When the viscous resistance becomes higher than the sintering driving force, the velocity starts do decrease. Decreasing velocity in turn causes a decrease of the viscous resistance. Finally, the two forces get very close. Then, the resultant force becomes very small which explains a slow rate of the sintering process analysed.
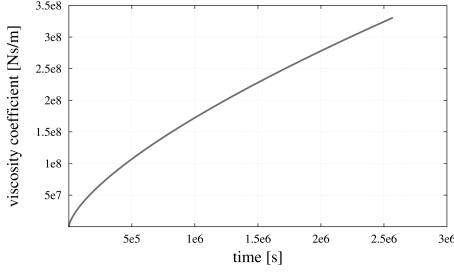
Figure 5.3. Evolution of the viscosity coeffi-
cient at free sintering of two particles of Cu.
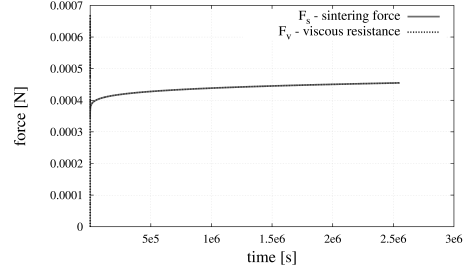
Figure 5.4. Evolution of sintering force and
viscous resistance at free sintering of two
particles of Cu – mass scaling factor 10^{14}.
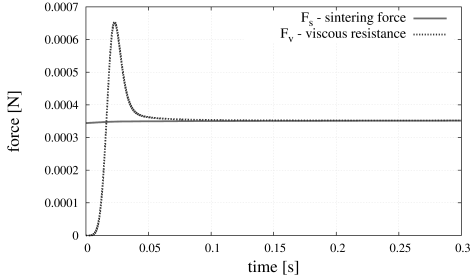
Figure 5.5. Evolution of sintering force and
viscous resistance at the initial stage of free
sintering of two particles of Cu (mass scale
factor 10^{14}).
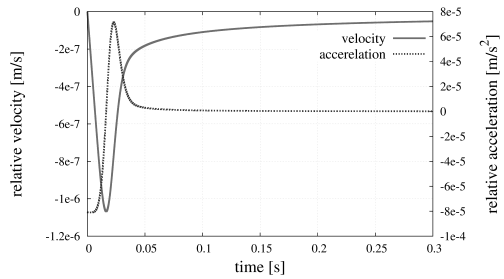
Figure 5.6. Evolution of velocity and acceler-
ation at the initial stage of free sintering of
two particles of Cu (mass scale factor 10^{14}).

The relative displacement plotted in Figs. 5.2a and 5.2b is identical with the
linear strain

$$\epsilon = \frac{\Delta L}{L_0}, \tag{5.1}$$

where L_0 is the initial length of a body subjected to deformation. Let us consider
a regular body-centered cubic (BCC) packing of identical spheres. A represen-
tative cell of the assembly is shown in Fig. 5.7. The average density $\bar{\rho}$ of the
BCC packing is $\pi\sqrt{3}/8 \approx 0.68$ [218].

If such an assembly undergoes free sintering then we have isotropic defor-
mation characterized with the strain ϵ in any direction. The corresponding vol-
umetric strain can be calculated as:

$$\epsilon_{\mathrm{v}} = \frac{\Delta V}{V_0} = \frac{L_0^3(1+e)^3 - L_0^3}{L_0^3} = (1+\epsilon)^3 - 1. \tag{5.2}$$

The relative density during sintering ρ_{rel} can be easily calculated as:

$$\rho_{\mathrm{rel}} = \overline{\rho} \frac{1}{(1 + \epsilon)^3}. \tag{5.3}$$

Using the formula (5.3) the evolution of the relative density during isotropic sintering characterized with linear strain (shrinkage) can be determined (Fig. 5.2a). The result is presented in Fig. 5.8 in comparison with the simulation results from [58] and experimental data from [217]. It can be seen that in a simple way the evolution of the relative density can be obtained which is in quite a good agreement with the reference results.
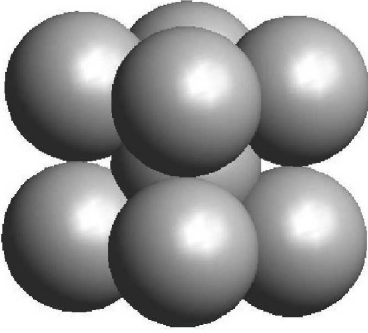
Figure 5.7. BCC sphere packing.
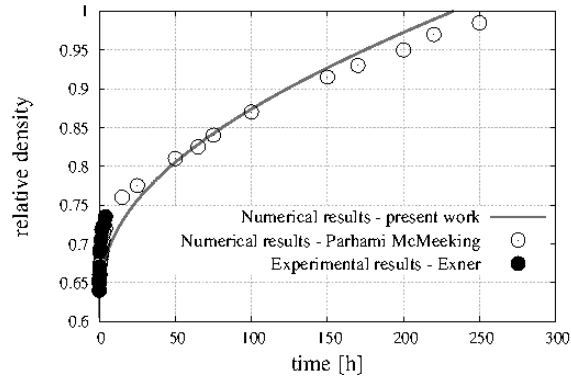
Figure 5.8. Evolution of relative density – comparison with numerical results from [58] and experimental ones from [217].

Simulation of free sintering by means of the viscoelastic model

The problem of sintering of two copper particles defined previously has also been analysed using the viscoelastic model. The set of material data given in Table 5.1 has been completed with the spring stiffness $k_{\mathrm{n}} = 7 \cdot 10^5$ N/m. Taking a cylindrical bar of length and diameter both equal $2r$ as an equivalent element to the considered two-particle system, the Young's modulus E corresponding to the stiffness k_{n} can be determined:

$$E = \frac{2k_{\mathrm{n}}r}{\pi r^2} = \frac{2k_{\mathrm{n}}}{\pi r} = \frac{2 \cdot 7 \cdot 10^5}{\pi \cdot 22.5 \cdot 10^{-6}} \text{ Pa} \approx 2 \cdot 10^{10} \text{ Pa,}$$

which is a reasonable value for copper at elevated temperature [219].

Figures 5.9a and 5.9b show displacement curves as functions of time obtained using the viscous and viscoelastic models for the same mass scaling.

a)   b)
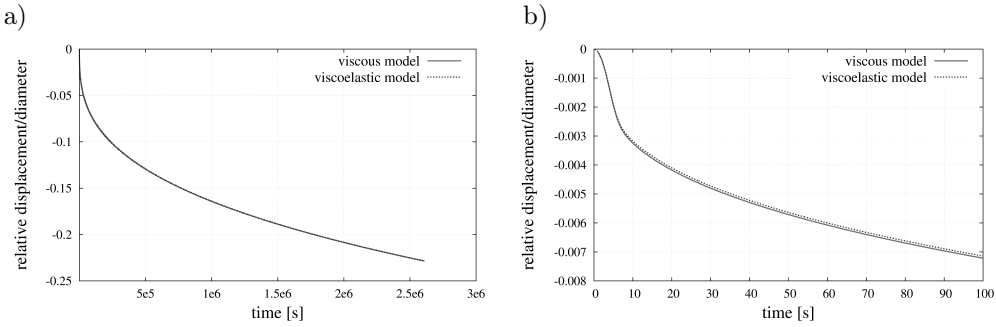
Figure 5.9. Evolution of relative displacement: a) of whole period, b) at the initial stage of free sintering of two particles of Cu (mass scale factor 10^{14}).

It can be seen that the curves from both models practically coincide. It is understandable, because the elastic part of displacements is very small (Figs. 5.10a and 5.10b) while the viscous part in the viscoelastic model should be similar to the displacements in the viscous model.

a)   b)
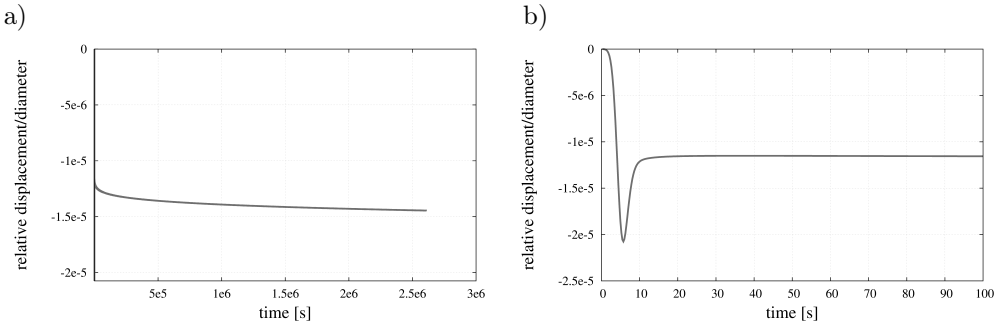
Figure 5.10. Evolution of the relative elastic displacement: a) of whole period, b) at the initial stage of free sintering of two particles of Cu (mass scale factor 10^{14}).

Coincidence of the curves in Figs. 5.9a and 5.9b confirms the correctness of the implementation of the viscoelastic model. The correctness is also verified by the agreement of the curves representing viscous resistance obtained using the two models in Figs. 5.11a and 5.11b.

A large difference between the two models can be seen when the computational efficiency is considered. Simulation using the viscoelastic model requires much less time than that performed by means of the viscous model. Time integration of the viscoelastic model allows the use of much larger time steps, which is illustrated in Fig. 5.12 showing evolution of critical time steps in the two models for mass scaling factors 10^{14} and 10^{16}.

a) b)
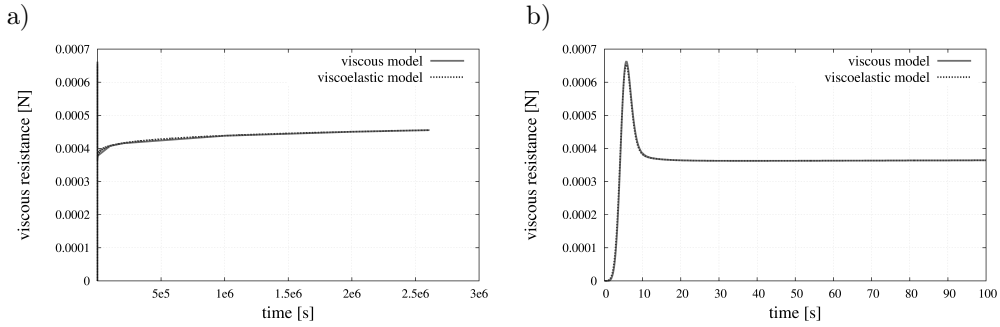
Figure 5.11. Evolution of sintering force and viscous resistance: a) of whole period, b) at the initial stage of free sintering of two particles of Cu (mass scale factor 10^{14}).

a) b)
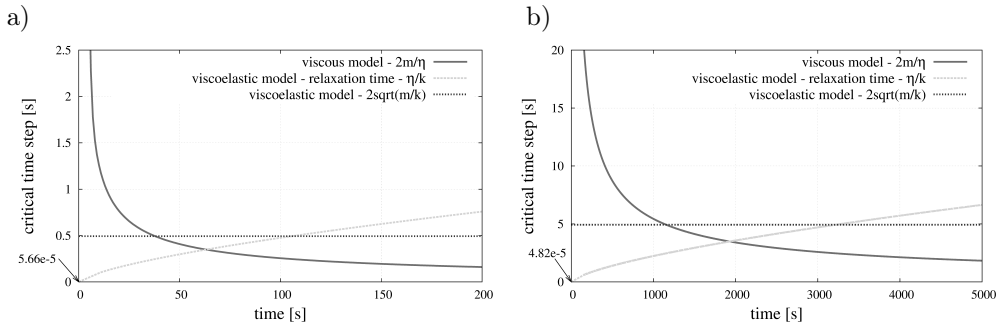
Figure 5.12. Comparison of critical time steps for the viscous and viscoelastic models at the initial stage of free sintering of two particles of Cu: a) mass scale factor 10^{14}, b) mass scale factor 10^{16}.

The process is characterized with variable viscosity therefore the critical time step varies during the simulation. The critical time step for the viscous model estimated according to Eq. (4.72) is compared with time steps limitations for the viscoelastic models used in the formula (4.73). It can be observed that the time integration of the viscous model allows larger time steps in the very beginning, but the critical time step decreases rapidly due to the increase of viscosity, cf. Fig. 5.3. Time integration of the viscoelastic model requires smaller time steps in the initial stage when the time step is limited by the relaxation time of the Maxwell element calculated according to Eq. (4.75).

With the growing relaxation time the critical time step increases until the relaxation time becomes larger than the limitation imposed by the undamped vibrations. From this moment the critical time step is controlled by Eq. (4.70) and it is constant till the end of sintering. The interval when the critical time step in the viscoelastic model is restricted by the relaxation time is short in

comparison with the rest of the process time. Therefore the efficiency of the process depends primarily on the value obtained from Eq. (4.70). As it can be observed this value is larger than the critical time step for the viscous model. This guarantees much better efficiency of the viscoelastic model in comparison with the viscous one. Analysis data for two values of mass scaling factor are summarized in Table 5.2. In both cases number of time steps required for the viscous model and resulting computation times are much larger than respective values for the viscoelastic model. Computation effort at a single step for the viscous model is twice smaller than for the viscoelastic model but this does not compensate much higher number of time steps. This demonstrates clearly advantage offered by the newly developed viscoelastic model.

Table 5.2. Summary of the analysis data for the different mass scaling factors

α_m factor	Model	Sintering time [s]	Number of time steps	Time step length [s]	CPU [s]	CPU/step [s]
10^{14}	viscous	$2.61 \cdot 10^6$	$2.61 \cdot 10^{10}$	$10^{-3} - 10^{-4}$	1355	$5.2 \cdot 10^{-8}$
	viscoelastic	$2.61 \cdot 10^6$	$6.63 \cdot 10^6$	$10^{-5} - 0.4$	0.9	$1.3 \cdot 10^{-7}$
10^{16}	viscous	$2.61 \cdot 10^6$	$2.61 \cdot 10^8$	$10^{-1} - 10^{-2}$	17	$6.5 \cdot 10^{-8}$
	viscoelastic	$2.61 \cdot 10^6$	$9.73 \cdot 10^5$	$4 \cdot 10^{-5} - 4$	0.12	$1.2 \cdot 10^{-7}$

5.1.2 Simulation of sintering under pressure

Two copper particles of 22.5 µm have been assumed to be subject to sintering at temperature 1300 K under the compressive force 0.01 N corresponding to the pressure of 6.3 MPa

$$p = \frac{F}{\pi r^2} = \frac{10^{-2} \text{ N}}{\pi \cdot (22.5 \cdot 10^{-6})^2 \text{ m}^2} = 6.3 \cdot 10^6 \text{ Pa}.$$

The force curve as a function of time is plotted in Fig. 5.13.

The force increases linearly until the steady state value is reached. Sintering starts when the final loading level is achieved. Both viscous and viscoelastic models have been used to simulate this process. The purpose of this numerical test was to verify performance of both model applied to an elementary problem of sintering under pressure. The material model parameters have been taken as given in Table 5.1. The similar as above spring stiffness $k_n = 7 \cdot 10^5$ N/m is taken for the Maxwell element in the viscoelastic model of sintering as well as for the Kelvin-Voigt element employed to model the compression stage preceding sintering. The damping ratio ξ in the Kelvin-Voigt model is assumed to be
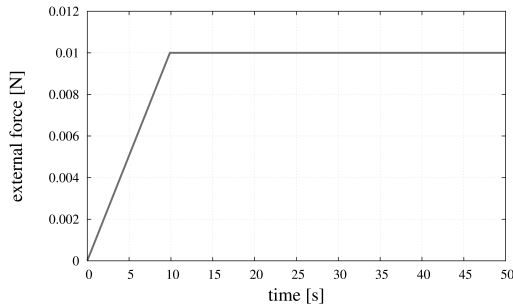
Figure 5.13. Compressive force as a function of time.

0.7 of the critical damping evaluated according to Eq. (4.25). Transition time t_{rel} between the Kelvin-Voigt and Maxwell models has been taken as 10 s. The viscosity in the Maxwell element immediately after transition has been assumed as $\eta_\infty = 10^7$ Ns/m. Results of the analyses are presented in Figs. 5.14 and 5.15. Figures 5.14a and 5.14b show displacement curves as functions of time obtained using the viscous and viscoelastic models for the same mass scaling.

a)

b)
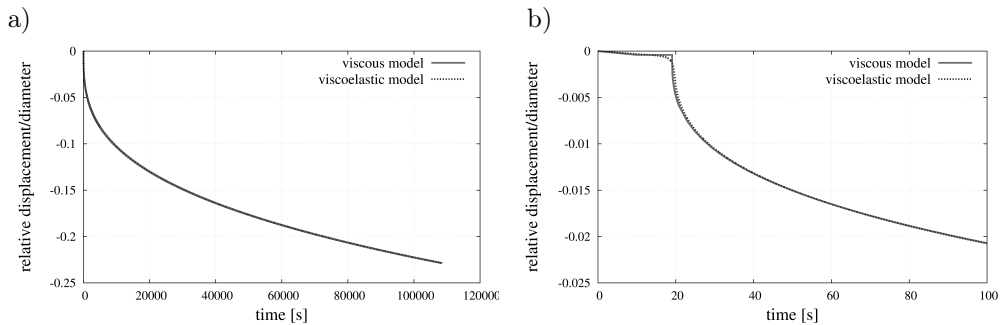
Figure 5.14. Evolution of relative displacement: a) of whole period, b) at the initial stage of sintering under pressure of two particles of Cu (mass scale factor 10^{14}).

It can be seen that the curves from both models practically coincide. Some differences can be observed in the initial stage of sintering. The change of displacements is gradual in the viscoelastic model because smooth transition between the compression and sintering is employed. When the viscous model is assumed this smoothing is not necessary, since no oscillations can occur. Due to smooth initiation of sintering the sintering is slightly delayed when the viscoelastic model is used. In order to have a better correspondence between the two models the beginning of sintering in the viscous model has been shifted by 10 s.

The force components obtained in the viscoelastic model in the initial stage and during the whole process are plotted as a function of time in Figs. 5.15a

a)

b)
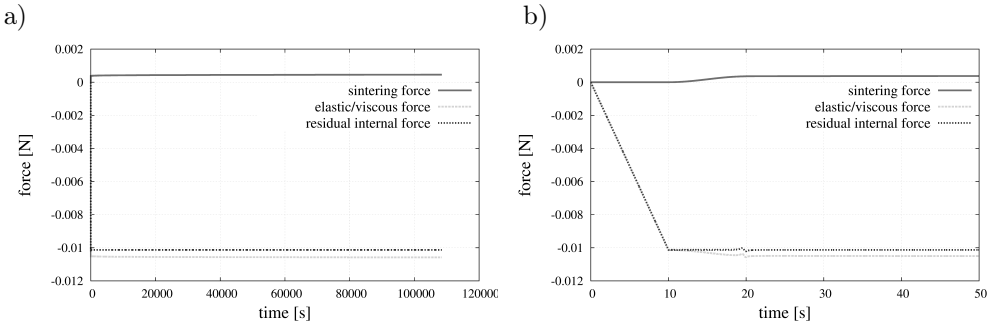
Figure 5.15. Evolution of forces at sintering under pressure of two particles of Cu (mass scale factor 10^{14}): a) of whole period of sintering, b) at the initial stage of sintering.

and 5.15b. The kinetics of the free sintering and sintering under pressure of two copper particles is compared in Fig. 5.16 by the displacement plots. We can see that application of an external force speeds up the sintering process.
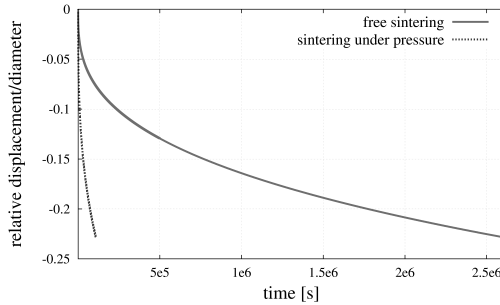
Figure 5.16. Evolution of relative displacement at sintering of two particles of Cu (mass scale factor 10^{14}) – comparison of viscoelastic solutions for free and under pressure sintering.

5.2 Generation of the geometrical model of powder specimen

Further numerical studies involve simulations of the hot pressing processes of pure NiAl, pure Al_2O_3 and NiAl-Al_2O_3 composite materials which were studied experimentally in Sec. 3. Simulations will be performed using a cylindrical specimen smaller than the real one but keeping the real size and size distribution of powder particles.

Discrete element specimens of the one- and two-phase powders with prescribed size distribution filling the cylindrical container have been generated using a specially developed original numerical algorithm presented in Appendix C. The generation algorithm consists of two stages: (i) generation of randomly dis-

tributed in space loose particles with sizes according to powder particle size distribution, (ii) compaction of particles to achieve a densely packed specimen by a dynamic method (under the gravity and prescribed contraction of the boundary surfaces).

The generated specimens of NiAl, Al_2O_3 and 80%NiAl-20%Al_2O_3 composite materials are shown in Fig. 5.17. The intermetallic phase is marked in dark orange, the ceramic phase is grey. The obtained specimens have the following dimensions: NiAl – diameter 0.058 mm, height 0.095 mm, Al_2O_3 – diameter 0.028 mm, height 0.065 mm, composite – diameter 0.057 mm, height 0.13 mm.
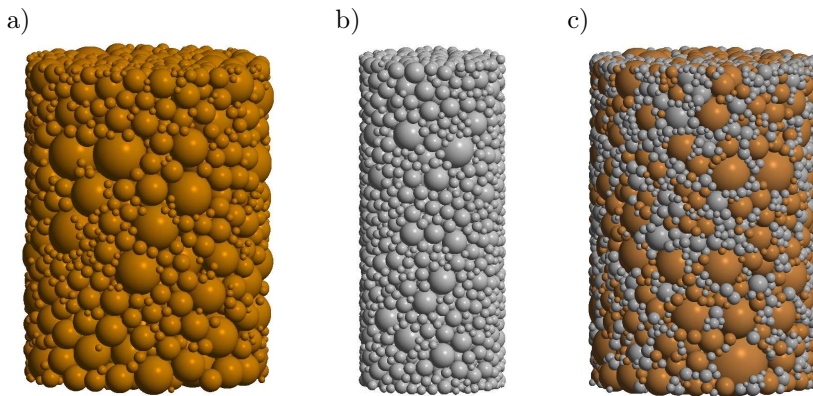
Figure 5.17. Discrete element specimens of a) one-phase NiAl powder, b) one-phase Al_2O_3 powder, c) two-phase 80%NiAl-20%Al_2O_3 powder.

The specimens have been generated using the real particle size distributions of the intermetallic NiAl and ceramic Al_2O_3 powders shown in Figs. 3.2a and 3.2b (Subsec. 3.2), respectively. The particle size distributions in the specimens of the NiAl and Al_2O_3 powders are presented in the form of histograms in Fig. 5.18, and the statistical information of the particle size distributions in all the three specimens is given in Table 5.3.

Table 5.3. Statistical parameters of the particle size distributions in the specimens [µm].

Statistical parameter	One-phase sample		Two-phase sample
	intermetallic NiAl	ceramic Al_2O_3	NiAl-20Al_2O_3
Mean value	3.97	2.48	3.01
Standard deviation	2.50	0.89	1.80
Maximum value	18.61	5.88	18.61
Minimum value	1.50	1.25	1.25
Number of particles	1751	2242	4952

a)   b)
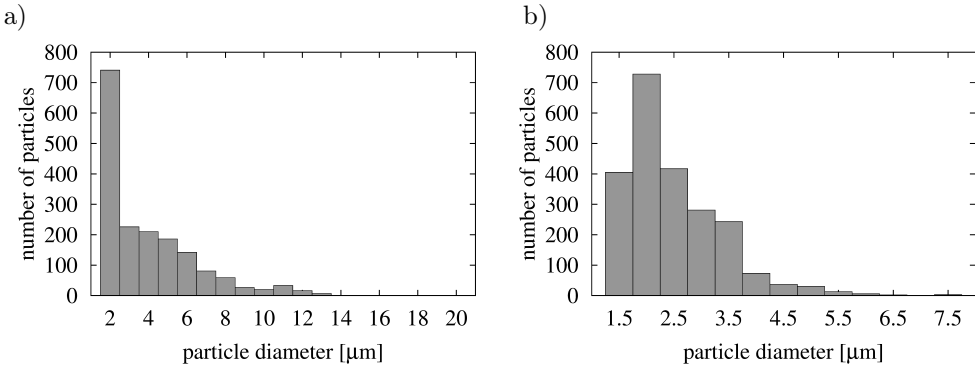
Figure 5.18. Particle size distribution in the specimens of: a) intermetallic NiAl powder, b) ceramic Al_2O_3 powder.

The particle size distributions in the models are slightly different from the particle size distribution of the real powders. Due to a small size of the numerical specimen, the biggest particles of the intermetallic powder ($d_p > 20$ µm) were not considered in the generation. Furthermore, the number of particles with a diameter in the range of 10 and 20 µm has been reduced. Figure 5.19 presents the distribution of the volume fraction of particle size of ceramic Al_2O_3 and intermetallic NiAl powder, which proves that the largest particles, even not so many, occupy much volume in the specimen domain. These assumptions were necessary to create a numerical model which represents sufficiently well the real powder and is suitable for efficient simulation.

a)   b)
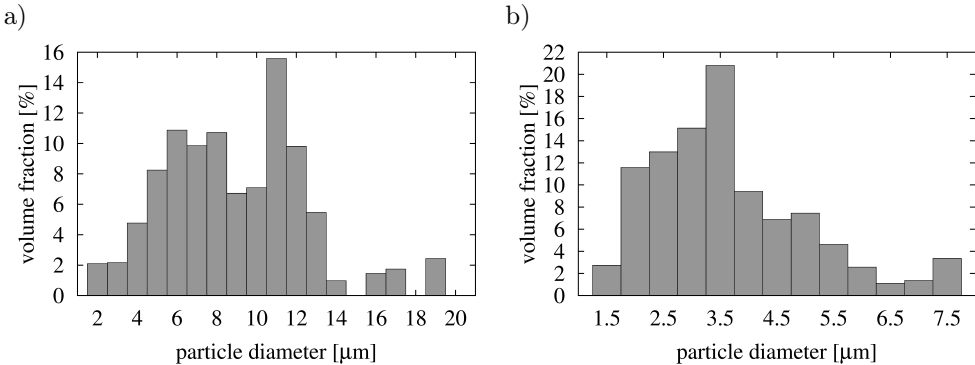
Figure 5.19. The distribution of volume fraction of powder particle size of: a) intermetallic NiAl, b) ceramic Al_2O_3.

The particle size distributions given in Fig. 5.18 have been adopted for each of the phases (intermetallic and ceramic ones) in generation of the composite specimen. The distributions of the number and the volume fractions of particles

corresponding to each phase and the mixture presented in Figs. 5.20 and 5.21, respectively. The histograms in Fig. 5.21 shows that larger particles despite their small number occupy significant volume fraction of the specimen.
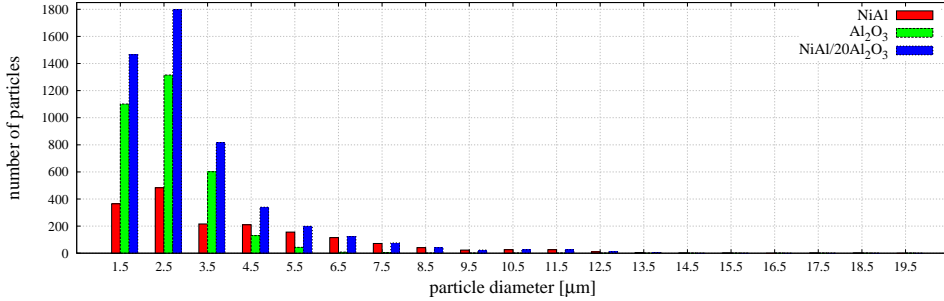
Figure 5.20. The distribution of the number of particle size of NiAl-20%Al$_2$O$_3$ powder mixture with its phases – NiAl and Al$_2$O$_3$.
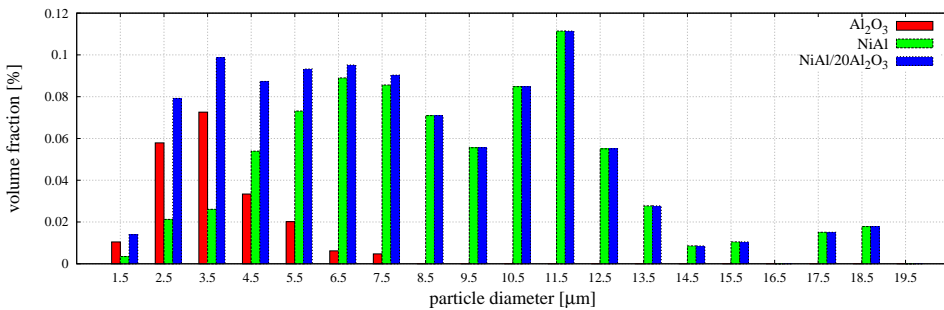
Figure 5.21. The distribution of the volume fraction of particle size of NiAl-20%Al$_2$O$_3$ powder mixture with its phases – NiAl and Al$_2$O$_3$.

5.3 Simulation of powder metallurgy process of one-phase powders

The specimens of one-phase powders, intermetallic NiAl and ceramic Al$_2$O$_3$ ones, whose generation was described in the previous subsection have been used in simulation of the whole manufacturing process. The present subsection shows calibration of the model. Preliminary values of the material model parameters have been determined based on the data from the literature. Then, the parameters have been tuned by adjustment of the numerical density evolution to the experimental data for a selected case of laboratory tests described in Sec. 3.

The particle interaction model is defined by the diffusion parameters (the atomic volume Ω and the pre-exponential factor of the grain boundary diffusion $D_{0\mathrm{gb}}$), the elastic constants (Young's modulus E and Poisson's ratio ν) and the parameters resulting from surface tension (surface energy γ_s and dihedral angle Ψ). The material parameters of sintering model were estimated on the basis of equations presented in the Subsec. 4.10. Furthermore, the selected parameters were confronted with the literature data [192, 220, 221]. Procedure of the evaluation of material model parameters, on the example of NiAl material, has been presented in Appendix B. The estimation of alumina parameters has been performed analogously. The material data of intermetallic and ceramic powders used in the calibration process have been shown in Table 5.4.

Table 5.4. Materials model parameters of contact interaction between NiAl-NiAl and Al_2O_3-Al_2O_3 particles.

Material constant	Parameter value	
	NiAl-NiAl	Al_2O_3-Al_2O_3
Mean atomic volume, Ω [m^3]	$1.20 \cdot 10^{-29}$	$8.47 \cdot 10^{-30}$
Pre-exponential factor of the grain boundary diffusion, $D_{0\mathrm{gb}}$ [m^2/s]	$2.55 \cdot 10^{-5}$	9.751
Activation enthalpy of grain boundary diffusion, ΔH_gb [kJ/mol]	185	389
Grain boundary width, δ [nm]	0.5	0.5
Young's modulus, E [GPa]	183	404
Poisson's ratio, ν	0.34	0.232
Surface energy, γ_s [J/m^2]	1.57	1.28
Dihedral angle, Ψ [°]	147	127
Density, ρ_theo [kg/m^3]	5910	3970
Coefficient of thermal expansion, α [10^{-6} K^{-1}]	11.5	7.4

In the calibration procedure, the activation enthalpy of grain boundary diffusion, ΔH_gb, has been treated as a fitting parameter in a similar way as in [65]. The obtained values of ΔH_gb of intermetallic and ceramic materials are in correspondence with experimental measurements [222–224] and the empirical approximation for BCC materials (NiAl) [196]. Table 5.4 contains the final value of the parameter ΔH_gb obtained in the calibration.

The numerical model for both one-phase powders has been calibrated for the external pressure $p = 30$ MPa, sintering temperature $T_\mathrm{s} = 1400$°C (1673 K) and sintering time $t_\mathrm{s} = 30$ min. The temperature and pressure profiles of the whole process are presented in Fig. 5.22.
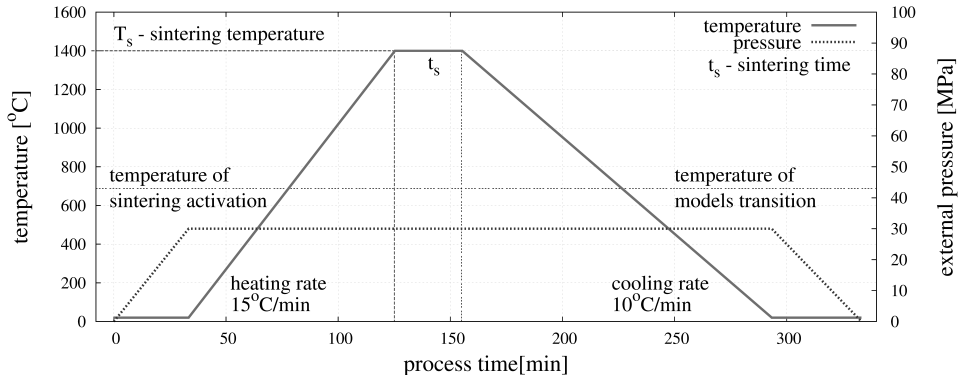
Figure 5.22. Temperature and pressure profiles for the powder metallurgy process of inter-metallic powder at $T_s = 1400°C$, $t_s = 30$ min and $p = 30$ MPa.

Temperature was increased with the heating rate of 15°C/min. Beginning of sintering for NiAl and alumina powders has been assumed at temperature of 683°C and 899°C, respectively. The temperatures corresponding to 0.5 of the melting point have been taken in both cases, assuming as appropriate temperature of grain boundary diffusion activation [79]. Specimens were kept at the sintering temperature, $T_s = 1400°C$, during the sintering time, $t_s = 30$ min, and cooled to the room temperature with the cooling rate of 10°C/min. In order to increase numerical efficiency, the mass of intermetallic and ceramic particles has been algorithmically scaled by factors 10^{17} and 10^{18}, respectively.

The configurations of the NiAl and alumina specimens before and after sintering are shown in Figs. 5.23 and 5.24, respectively. The shrinkage of the specimen during sintering can be clearly noticed.

Volume changes of the NiAl specimen during the whole process are presented in Fig. 5.25. Except for the volume changes represented by the volumetric shrinkage ϕ_V, Fig. 5.25 presents the evolution of the linear shrinkage in x, y and z direction, denoted by ϕ_x, ϕ_y, ϕ_z. The shrinkage parameters has been calculated from the following relationships:

$$\phi_x = \frac{R_x}{R_{0x}}, \qquad \phi_y = \frac{R_y}{R_{0y}}, \qquad \phi_z = \frac{H}{H_0}, \qquad \phi_V = \frac{V}{V_0}, \qquad (5.4)$$

where R_x and R_y are the bulk radii of the geometrical model of the specimen in the x and y direction, R_{0x} and R_{0y} are the initial radii of geometrical model, H and H_0 are the bulk and initial height of the geometrical model, respectively, and V and V_0 are the bulk and initial volume, respectively.

a)   b)
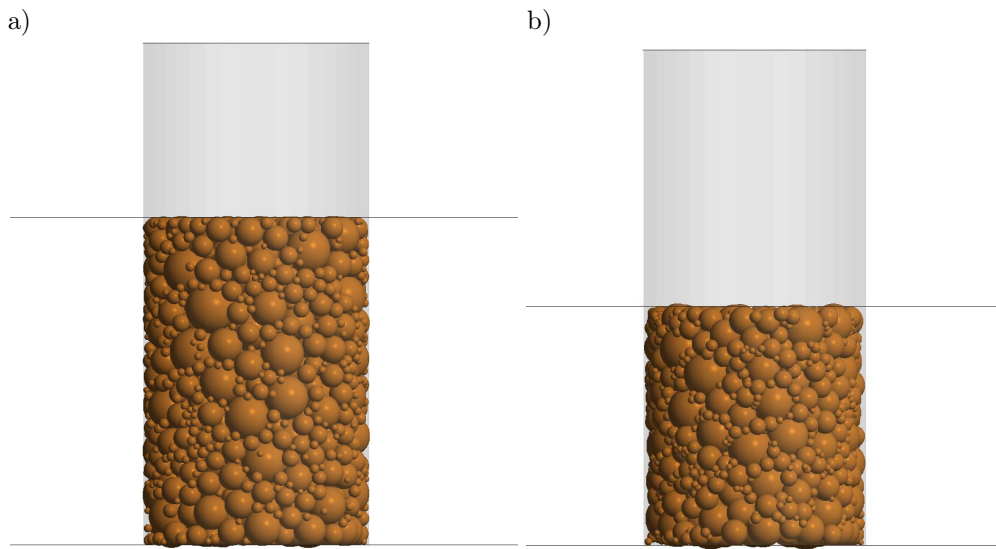
Figure 5.23. Geometry of the NiAl specimen: a) before sintering, b) after sintering.

a)   b)
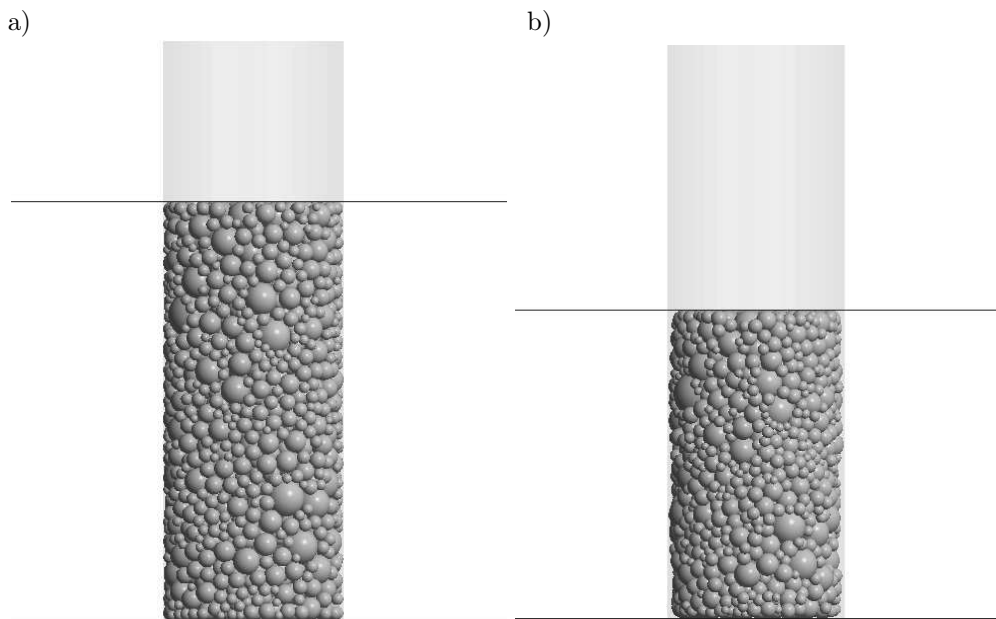
Figure 5.24. The geometrical model of alumina specimen: a) before sintering, b) after sintering.
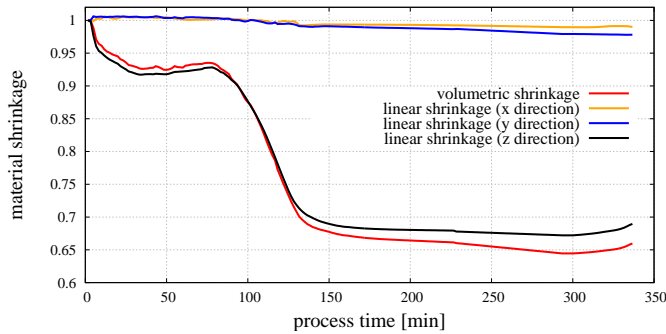
Figure 5.25. Evolution of the volumetric and linear shrinkage of the intermetallic specimen.

The shrinkage of the specimen leads to the increase of the density. The relative density for the whole process was determined using the following equation:

$$\rho_{\mathrm{rel}} = \frac{\rho}{\rho_{\mathrm{theo}}}, \tag{5.5}$$

where ρ is the bulk density, ρ_{theo} is the temperature-dependent theoretical density given by equation:

$$\rho_{\mathrm{theo}} = \frac{\rho_{\mathrm{theo}}^{0}}{(1 + \alpha \Delta T)^{3}}, \tag{5.6}$$

where ρ_{theo}^{0} is the theoretical density at the room-temperature, α is the linear coefficient of the thermal expansion and ΔT is the temperature increment. The bulk density ρ has been determined taking the powder mass and the specimen volume at the considered time.

The numerical model will be calibrated and validated using the experimental density measurements given in Table 3.2. It will be convenient to present the experimental data according to measurement points which can be used for each sintering temperature as it is shown in Fig. 5.26.
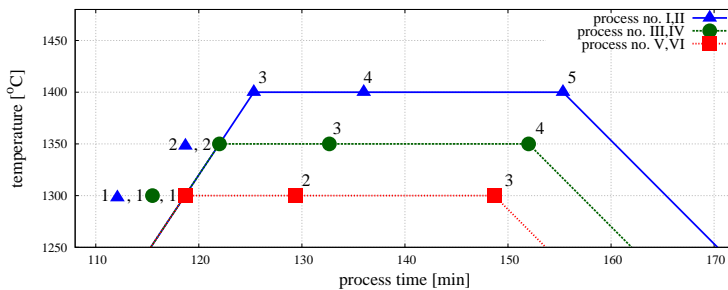
Figure 5.26. Thermal profiles with density measurement points.

The first measurement points from lower temperatures can also be used for processes with higher temperatures. The experimental data for sintering of the NiAl and alumina powders rewritten in this way are shown in Tables 5.5 and 5.6, respectively.

Table 5.5. Experimental density measurements for sintering of the NiAl powder.

No	Process parameters		Density measurement point				
	$T_s[°C]$	p [MPa]	1	2	3	4	5
I	1400	30	5.25 (0.89)	5.35 (0.91)	5.42 (0.92)	5.78 (0.98)	5.86 (0.99)
II	1400	5	4.66 (0.79)	4.75 (0.80)	5.24 (0.89)	5.33 (0.90)	5.45 (0.92)
III	1350	30	5.25 (0.89)	5.35 (0.91)	5.52 (0.93)	5.73 (0.97)	–
IV	1350	5	4.66 (0.79)	4.75 (0.80)	4.97 (0.84)	5.13 (0.87)	–
V	1300	30	5.25 (0.89)	5.43 (0.92)	5.52 (0.93)	–	–
VI	1300	5	4.66 (0.79)	4.88 (0.82)	4.90 (0.83)	–	–

Table 5.6. Experimental density measurements for sintering of the alumina powder.

No	Process parameters		Density measurement point				
	$T_s[°C]$	p [MPa]	1	2	3	4	5
I	1400	30	3.45 (0.87)	3.56 (0.90)	3.86 (0.97)	3.88 (0.98)	3.97 (1)
II	1400	5	2.58 (0.65)	2.93 (0.74)	3.32 (0.84)	3.38 (0.85)	3.61 (0.91)
III	1350	30	3.45 (0.87)	3.56 (0.90)	3.85 (0.97)	3.93 (0.99)	–
IV	1350	5	2.58 (0.65)	2.93 (0.74)	3.13 (0.79)	3.61 (0.91)	–
V	1300	30	3.45 (0.87)	3.58 (0.90)	3.80 (0.96)	–	–
VI	1300	5	2.58 (0.65)	2.77 (0.70)	3.34 (0.84)	–	–

The combinations of the sintering temperature and pressure in Tables 5.5 and 5.6, and in Fig. 5.26 have been associated with processes denoted with roman numbers I–VI. The data for the process I (T_s = 1400°C and p = 30 MPa) for each material have been used in the calibration procedure presented in this subsection. The other five processes will be used to validate the performance of the model which will be presented in Subsec. 5.5

The numerical curves showing evolution of the relative density of NiAl and Al_2O_3 material obtained as a result of the calibration procedure are compared with experimental in Figs. 5.27 and 5.28, respectively. It can be seen that the numerical curves represent quite well density changes in the real process.

Figures 5.27 and 5.28 show the process stages and the models applied in the analysis of these stages. The curves in Figs. 5.27 and 5.28 allow to analyse densification mechanisms during the process. Initially it can be observed a certain increase of relative density under the applied punch loading. During the heating the relative density does not change. When the material is heated the
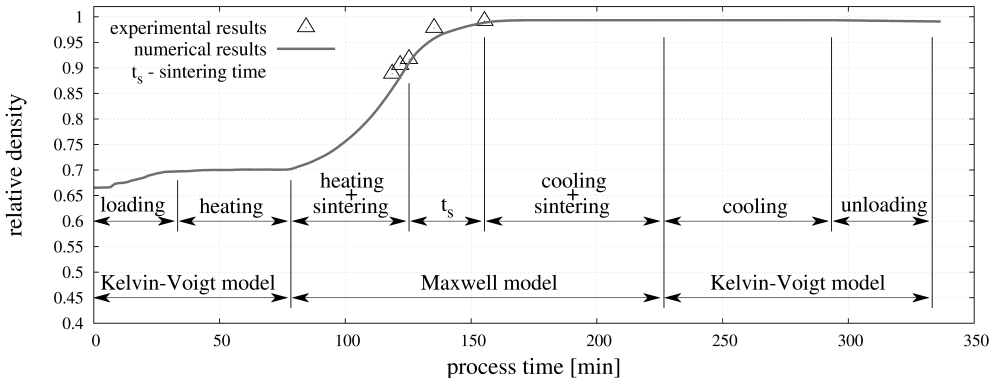
Figure 5.27. Evolution of the relative density of NiAl powder during the whole process.
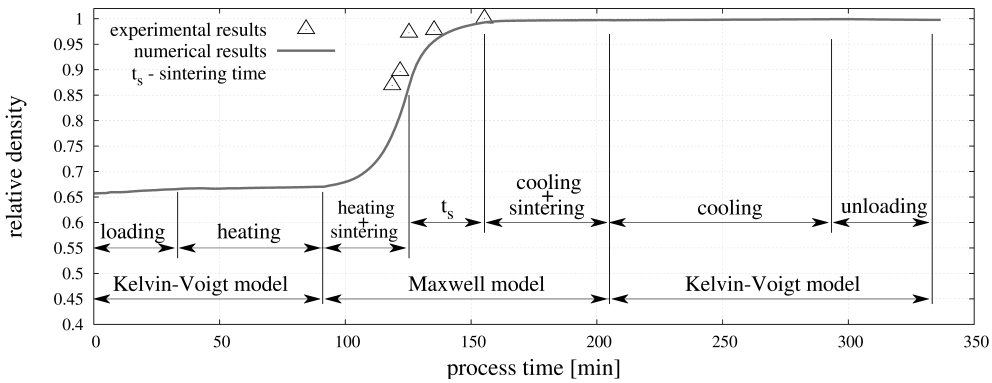
Figure 5.28. Evolution of the relative density of alumina powder during the whole process.

volume of the specimen grows as it can be observed in Fig. 5.25, but at the same time the theoretical density increases proportionally so the relative density remains unchanged. After reaching the temperature of sintering activation, densification begins. In the initial stage of sintering the growth of densification is relatively low, because the diffusion processes are limited at low temperature. Figure 5.29 presents the evolution of the diffusion coefficient D_{gb} of NiAl and alumina materials as the functions of temperature. The value of D_{gb} increases with temperature and furthermore lowers the viscosity of particle, which favours the densification. Simultaneously, the growth of temperature reduces the material stiffness, which is favourable for particles penetration and rearrangement. The evolution of the Young's modulus of NiAl and Al_2O_3 materials as the functions of temperature [88, 90] presented in Fig. 5.29 has been implemented in the numerical algorithm.
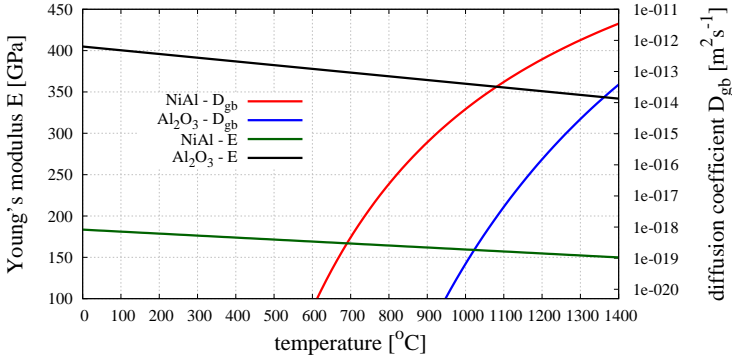
Figure 5.29. Evolution of the Young's modulus and diffusion coefficient of NiAl and alumina materials in the function of temperature.

As the temperature increases, the growth of densification accelerates. This particular effect can be seen in Fig. 5.30, where the dependence of the densification rate and relative density of two materials has been shown. Densification rate $\dot{\rho}_{\mathrm{rel}}$ has been treated as the increment of relative density $\Delta\rho_{\mathrm{rel}}$ in certain increment of time Δt:

$$\dot{\rho}_{\mathrm{rel}} = \frac{\mathrm{d}\rho_{\mathrm{rel}}}{\mathrm{d}t} = \frac{\Delta\rho_{\mathrm{rel}}}{\Delta t}. \tag{5.7}$$
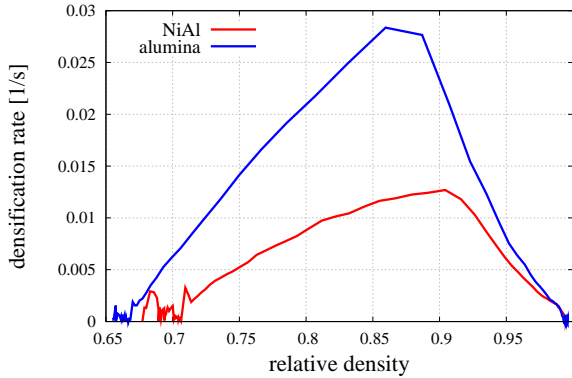
Figure 5.30. Dependence of the densification rate in the function of relative density.

It can be seen in Fig. 5.30 that from the value of relative density corresponding to the transition of models and activation of sintering ($\rho_{\mathrm{rel}} = 0.705$ – NiAl, $\rho_{\mathrm{rel}} = 0.675$ – alumina), the materials densification increases with a near linear rate, which is typical for the intermediate stage of sintering. The highest densification rate can be seen near the value 0.90 of the relative density, while the sintering temperature $T_{\mathrm{s}} = 1400°\mathrm{C}$ is achieved. In this particular moment the

viscosity and stiffness of discrete elements are at their lowest levels. After this point, during the sintering time $t_s = 30$ min, the material is compacted with a constantly decreasing rate. This can be seen in Figs. 5.27, 5.28 and 5.25, where the relative density and the volumetric shrinkage are gradually stabilized. This effect is characteristic for the final stage of sintering - the penetration of particles is blocked by a high viscosity of material. The value of η calculated according to Eq. (4.40) rises because of the increase of the neck radius, which results in a higher value of the viscous resistance. Furthermore, the neck radius a of most particle connections reaches the maximum value at the equilibrium state a_{max} (given by Eq. 4.32), which signifies the end of sintering. At this point, the relative density of considered materials reaches values very close to 1 ($\rho_{rel} = 0.993$ – NiAl, $\rho_{rel} = 0.998$ – alumina), which means that an almost fully dense material has been obtained. As the material is cooled, the relative density may slightly increase due the impact of mass transport mechanism of particles, which have not achieved the equilibrium state yet. After reach the temperature of sintering activation/deactivation the relative density is constant, even though the dimensions and volume of the material decrease due to the thermal expansion effect. All the changes of the specimen volume and material density obtained in the analysis agree very well with the changes observed in a real process.

5.4 Simulation of powder metallurgy process of two-phase powder

Simulations of powder metallurgy process of two-phase powder have been performed in order to evaluate the material model parameters allowing to fit the numerical results of the composite relative density to the experimental data. Modeling of two-phase powders mixtures requires taking into account interactions between different materials. The three types of material interaction in the investigated composite: NiAl-NiAl, Al_2O_3-Al_2O_3 and NiAl-Al_2O_3 are shown schematically in Fig. 5.31.

a) b) c)
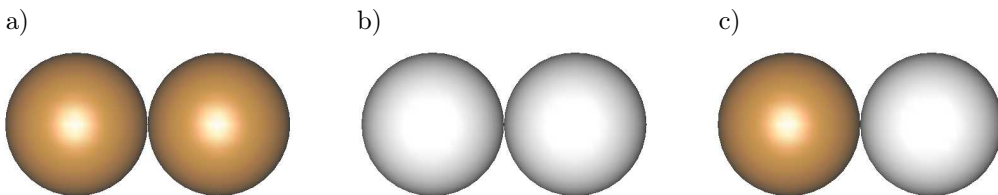
Figure 5.31. Three types of material interaction in the two-phase NiAl–Al_2O_3 powder: a) NiAl-NiAl, b) Al_2O_3-Al_2O_3, c) NiAl-Al_2O_3.

The materials parameters of sintering model for the NiAl-NiAl and Al_2O_3-Al_2O_3 interaction have been established in Subsec. 5.3. Now, the model of sintering of the two-phase powder should be completed with the parameters for the NiAl-Al_2O_3 interaction. Beforehand, however, let us analyse the character of the NiAl-Al_2O_3 bond.

The NiAl-Al_2O_3 interfaces in composites sintered at different process parameters were examined in [82]. Couplings between ceramic particles and NiAl were created in sintering performed at 1300°C. Nevertheless, at first they were observable only at some points. With the increase of the sintering temperature, a full and permanent bond has been achieved. The interface was relatively clean with no additional phases that could have been formed during the sintering process. It indicates a good quality of the sintered samples, since the formation of the transition phase resulting from the reaction between both phases would have weakened the interface. It was confirmed in the microanalysis performed using a TEM EDS detector that along the marked line across the interface there were changes in the content of Ni, O and Al, which did not indicate the presence of any transition phases (Fig. 5.32). The TEM analyses proved that the bond at the NiAl-Al_2O_3 interface was quite strong and had an adhesive character. The contrast change at the interface also suggested that no diffusive type interface layer was formed.

a)

b)
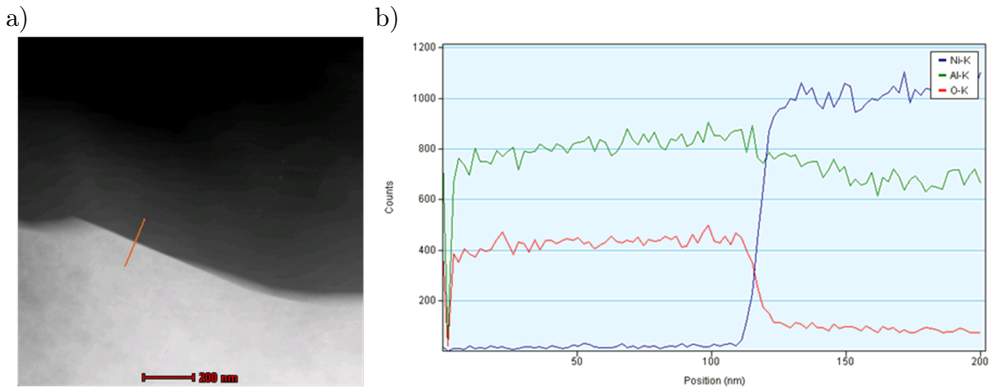
Figure 5.32. Scanning transmission electron micrograph (a) and changes of the content of Al, O and Ni along the marked line (b) [82].

Adhesive character of the contact bond between the intermetallic and ceramic particles should be taken into account in the formulation of the discrete element model of sintering. Thermo-viscoelastic model, presented in Subsec. 4.5.2, assumes the cohesion between interacting discrete elements and good penetration of the particles resulting from the diffusive character of the contact bond.

In the case of NiAl-Al$_2$O$_3$ interface, the penetration of the particles depends mainly on the viscosity of a material and applied external pressure. Due to this fact, it has been assumed that the sintering driving force F^{sint}, given by Eq. (4.36), will be neglected in the model of interaction between the NiAl and Al$_2$O$_3$ particles during sintering.

The material model parameters for the contact interaction of NiAl and Al$_2$O$_3$ particles have been estimated as follows: the mean atomic volume Ω has been evaluated similarly as it is described in Appendix B, the grain boundary width δ the same as for the NiAl, the effective Young's modulus $\overline{E}$ from Eq. (4.20). The material data of mixed contact interaction used in the calibration process have been shown in Table 5.7. The diffusive parameters (the pre-exponential factor of the grain boundary diffusion $D_{0\text{gb}}$ and the activation enthalpy of grain boundary diffusion ΔH_{gb}) estimated in Subsec. 4.10, will be employed as the fitting parameters in a similar way as in the case of calibration of the sintering model of one-phase powder (Subsec. 5.3). The material parameters of sintering model of the NiAl-Al$_2$O$_3$ interaction, evaluated in the way described above and tuned in the calibration procedure, are shown in Table 5.7.

Table 5.7. Materials model parameters of contact interaction between NiAl and Al$_2$O$_3$ particles.

Material constant	Parameter value
Mean atomic volume, Ω [m^3]	$9.01 \cdot 10^{-30}$
Pre-exponential factor of the grain boundary diffusion, $D_{0\text{gb}}$ [m^2/s]	$3 \cdot 10^{-2}$
Activation enthalpy of grain boundary diffusion, ΔH_{gb} [kJ/mol]	280
Grain boundary width, δ [nm]	0.5
Effective Young's modulus, $\overline{E}$ [GPa]	279

Similarly as calibration of the models for pure NiAl and Al$_2$O$_3$ powders, the numerical model of composite has been calibrated for following sintering process parameters: external pressure $p = 30$ MPa, sintering temperature $T_{\text{s}} = 1400°$C (1673 K) and sintering time $t_{\text{s}} = 30$ min. The experimental data for this case are shown in Table 5.8 as the measurements for the process no. I. Table 5.8 contains the results of the density measurements for sintering of the NiAl-Al$_2$O$_3$ composite presented earlier in Table 3.2 and rewritten according to the measurement points defined in in Fig. 5.26. The results for the processes II-VI will be used later for validation of the numerical model.

Table 5.8. Experimental density measurements for sintering of the NiAl-Al$_2$O$_3$ powder.

No	Process parameters		Density measurement point				
	$T_s[^\circ C]$	p [MPa]	1	2	3	4	5
I	1400	30	4.99 (0.90)	5.24 (0.95)	5.27 (0.95)	5.37 (0.97)	5.51 (1)
II	1400	5	3.86 (0.70)	4.02 (0.73)	4.11 (0.74)	4.28 (0.78)	4.92 (0.89)
III	1350	30	4.99 (0.90)	5.24 (0.95)	5.35 (0.97)	5.50 (1)	–
IV	1350	5	3.86 (0.70)	4.02 (0.73)	4.16 (0.75)	4.42 (0.80)	–
V	1300	30	4.99 (0.90)	5.03 (0.91)	5.44 (0.99)	–	–
VI	1300	5	3.86 (0.70)	4.01 (0.73)	4.10 (0.74)	–	–

The simulation has been performed using the specimen composed of 4952 discrete elements shown in Fig. 5.17c. The geometries of the specimen before and after sintering are shown in Fig. 5.33. The resulting shrinkage of the material can be clearly observed.
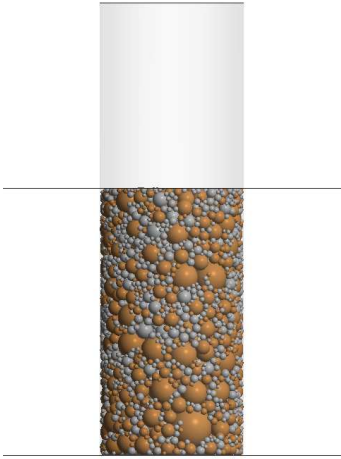
a)   b)
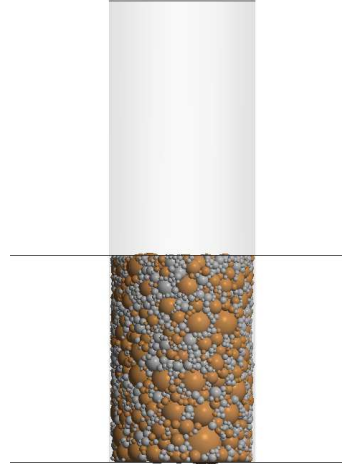
Figure 5.33. Geometrical model of NiAl-20Al$_2$O$_3$ specimen: a) before, b) after sintering.

The numerical and experimental evolution of the relative density of the sintered NiAl-20%Al$_2$O$_3$ specimen has been plotted in Fig. 5.34 together with the temperature profile. The temperature profile is the same as those presented in Fig. 5.22. The relative density of the composite has been evaluated from Eq. (5.5), where the temperature-dependent theoretical density of the composite ρ_{theo} is given by following relation:

$$\rho_{theo} = \frac{V_{mat}\rho_{theo}^{0,m}}{(1 + \alpha_{mat}\Delta T)^3} + \frac{V_{reinf}\rho_{theo}^{0,r}}{(1 + \alpha_{reinf}\Delta T)^3}, \tag{5.8}$$

where $\rho_{\text{theo}}^{0,\text{m}}$ and $\rho_{\text{theo}}^{0,\text{r}}$ are the theoretical densities of the composite matrix (NiAl) and reinforcement (Al$_2$O$_3$) at room-temperature, α_{mat} and α_{reinf} are the linear thermal expansion coefficients of the matrix and reinforcement, V_{mat} and V_{reinf} are the volume fractions of each phase, ΔT is the temperature increment. Values of the theoretical densities and the linear coefficients of the thermal expansion of NiAl and alumina materials are given in Table 5.4. Figure 5.34 shows a very good agreement of the numerical and experimental results which confirms that the material parameters of sintering model have been determined properly.
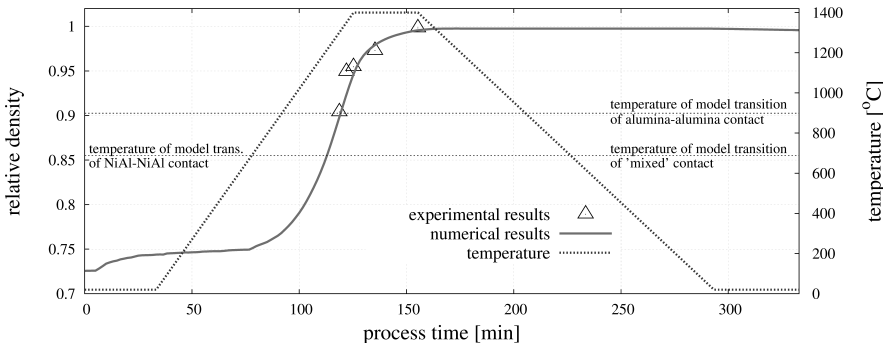
Figure 5.34. Evolution of the relative density of the mixture of NiAl-Al$_2$O$_3$ powder.

The character of the curve representing the evolution of the relative density of the composite obtained in the simulation is similar to the evolution curves for the pure intermetallic and pure ceramic powder plotted in Figs. 5.27 and 5.28, respectively. Similarly, an initial compaction related to the application of the external pressure of 30 MPa can be observed. The value of the relative density does not change until the temperature of sintering activation of intermetallic particles is achieved ($T = 683$°C). At this point, the sintering model is activated. In the initial stage of sintering the densification rate is quite low, but a gradual growth of temperature and the activation of sintering of ceramic particles ($T = 899$°C) accelerated the densification process.

Figure 5.35a presents a comparison of the relative density evolution of the pure NiAl, pure alumina and mixture of the NiAl/Al$_2$O$_3$ powders sintered in $T_{\text{s}} = 1400$°C and $p = 30$ MPa. The sintering of the intermetallic powder is characterized by a long densification with a relatively low rate, while alumina achieves a high relative density in a short time with a high rate. Comparison of the densification rate as a function of the relative density of all the studied powders has been made in Fig. 5.35b. It has to be mentioned that the composite material started the sintering stage from the highest relative density due to

relatively high diversity and a privileged distribution of the particle size, which reduces the porosity. Pure powders started the whole process from a lower relative density, and only the intermetallic powder has been compacted during compression due to a relatively low Young's modulus. As in the case of pure powders, the composite material indicates the highest densification rate at the intermediate stage of sintering and gradually slows down after reach the sintering temperature. While the sintering stage is finished, the relative density of composite material achieved value very close to 1, which refers to the obtainment of almost fully dense material. The graphical presentation of fully sintered $NiAl/Al_2O_3$ material can be seen in Fig. 5.33b.

a)   b)
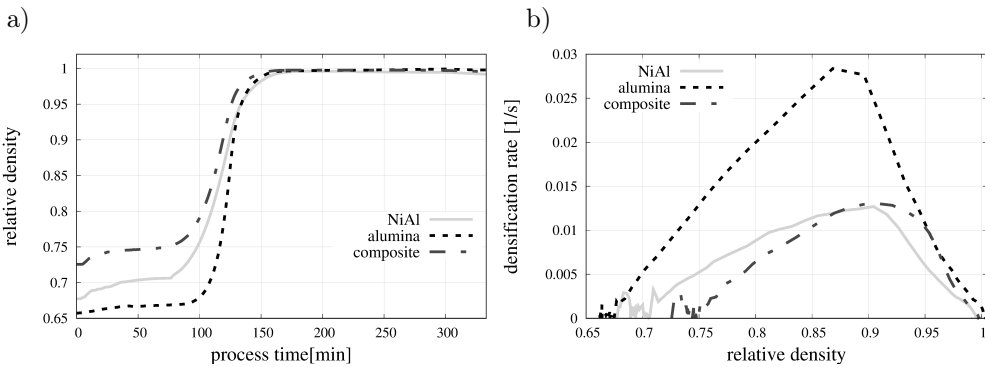
Figure 5.35. Comparison of: a) relative density evolution, b) densification rate of pure NiAl, pure alumina and mixture of $NiAl/Al_2O_3$ powder sintered in $T_s = 1400°C$ and $p = 30$ MPa.

5.5 Simulation of powder metallurgy process at different process parameters

The material model parameters given in Tables 5.4 and 5.7 determined in the calibration procedures in the previous subsections for one set of process parameters (process no. I) have been employed in simulation of powder metallurgy processes with different combinations of parameters (sintering temperature T_s, external pressure p) defined in Tables 5.5, 5.6 and 5.8 as processes no II–VI. The sintering time was the same for all the analyses ($t_s = 30$ min). The simulations of powder metallurgy processes have been performed for all the investigated powders: the one-phase intermetallic NiAl and ceramic Al_2O_3 powders and the two-phase $NiAl/20\%Al_2O_3$. The purpose of this subsection has been to validate the numerical model by comparing numerical and experimental results for different sets of sintering process parameters. Furthermore, the influence of applied

process parameters on the sintering kinetics has been studied. Numerical simulations have employed the same geometrical models of the initial dense specimens as in the calibration.

Evolution of the relative density for the pure NiAl and alumina powders for all the processes is presented in Figs. 5.36 and 5.37, respectively.
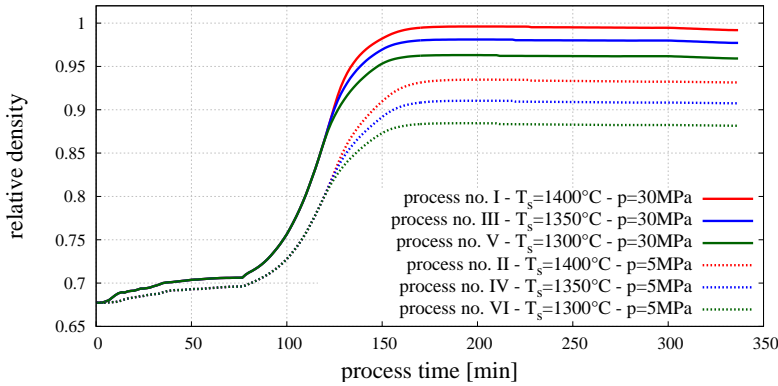
Figure 5.36. Evolution of the relative density of the intermetallic material for different sintering process parameters.
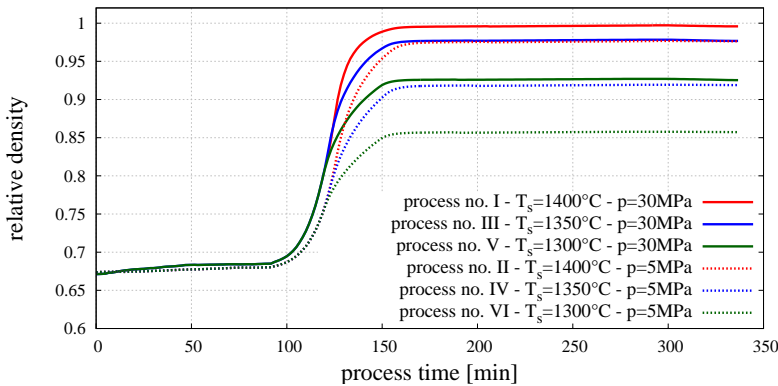
Figure 5.37. Evolution of the relative density of the alumina for different sintering process parameters.

The results show the correct performance of the numerical model. Comparison of the plots corresponding to a different pressure and the same temperature allows to assess an influence of the pressure. It can be seen, that generally, a higher external pressure gives a higher green density and faster and higher densification during sintering, however this effect is larger for the intermetallic specimen than for the alumina specimen. It can be explained by the higher

stiffness of the alumina which reduced the effect of the external pressure by blocking the particles penetration and rearrangement at the compaction and sintering stage.

The curves in Figs. 5.36 and 5.37 allow to asses the influence of the sintering temperature T_s on the densification of the one-phase powders. An increase of densification for the higher sintering temperature, which is proper result of numerical simulations, can be seen. The temperature affects the diffusion parameters, the effective diffusion coefficient of the grain boundary D_{eff} and the diffusion coefficient for vacancy transport in the grain boundary D_{gb}, which are one of the major indicators of sintering kinetics. The higher sintering temperature is, the lower the viscosity of the material is, which results in a higher diffusion rate and easier particle penetration. Influence of sintering temperature T_s on the NiAl material densification is smaller than that of the external pressure, especially in the case of the external pressure of 30 MPa, where the differences of the relative density after 30 min of sintering at temperature $T_s = 1300°C$ and $1400°C$ are about 3%. In case of the specimens sintered at the pressure of 5 MPa at the same sintering temperature, differences are approximately 4%. The effect of the sintering temperature on the alumina powder densification is more significant. The numerical results of the processes no. I and V (or II and VI) show a substantial gap between the relative density of the materials sintered at $T_s = 1300°C$ and $1400°C$. The sintering temperature $T_s = 1300°C$ seems to be insufficient for the alumina.

Evolution of the relative density for the composite material for all the processes is shown in Fig. 5.38. The densification of the composite material is similar
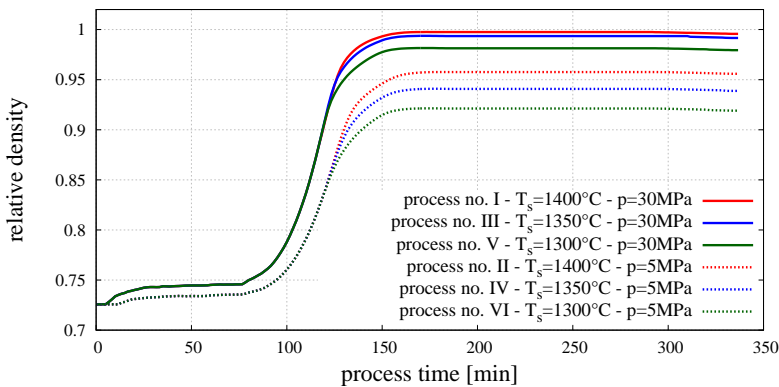
Figure 5.38. Evolution of the relative density of the composite NiAl-Al$_2$O$_3$ for different sintering process parameters.

to that of the NiAl material for the given process parameters, cf. Fig. 5.36. The main and obvious reason of this fact is the phase composition of composite – 80% NiAl and 20% Al_2O_3, where the major part of the material is composed of the intermetallic. As in the case of NiAl sintering, a significant influence of the applied pressure on the composite density during the sintering stage can be seen. The results show an importance of the external pressure to achieve an efficient manufacturing process of composite material irrespectively of the sintering temperatures.

The relative density evolution obtained in the numerical simulation has been confronted with experimental measurements in Fig. 5.39 – for NiAl sintering, Fig. 5.40 – alumina sintering, and Fig. 5.41 – for $NiAl/Al_2O_3$ composite sintering. These graphs show the sintering stage only, excluding the compaction and cooling stages.

A reasonably good correspondence between the numerical results and experimental data can be observed in most cases, especially in the case of NiAl sintering. The curves representing the numerical results pass through or close to the experimental points.

Comparison of the numerical and experimental results for the alumina show more differences. In particular, the lack of adjustment can be seen at the beginning of the sintering process, where the mismatch between numerical and experimental results achieves 0.1 of the relative density. This particular fault seems to be related to the shape of the powder particles. In Sec. 3 the morphology of alumina powder and evolution of microstructure during the sintering process was shown. In the initial stage of sintering the powder particles appear to have non-ideal spherical shapes with intergranular contacts between particles. Due to this heterogeneity of alumina microstructure, the real sintered material cannot obtain a relatively high densification. However, the intermediate stage of aluminium oxide's sintering begins with the changes in particle boundaries and the shape of pores. Hence, the shapes of powder particles correspond much more to the form of discrete elements, which is reflected by a better agreement of results.

Comparison of the numerical and experimental results for the alumina show more differences. In particular, the lack of adjustment can be seen at the beginning of the sintering process, where the mismatch between numerical and experimental results achieves 0.1 of the relative density. This particular fault seems to be related to the shape of the powder particles. In Sec. 3 the morphology of alumina powder and evolution of microstructure during the sintering process was shown. In the initial stage of sintering the powder particles appear to have non-ideal spherical shapes with intergranular contacts between particles.

a)

b)

c)
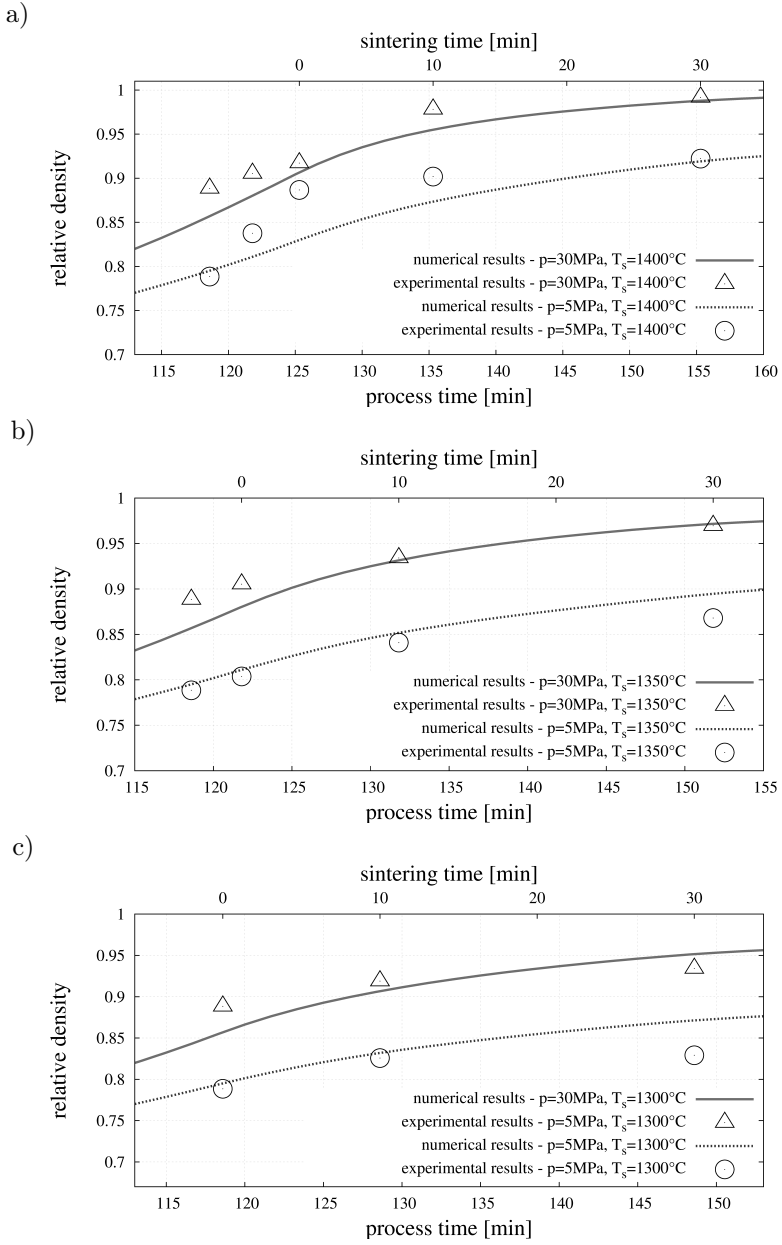
Figure 5.39. Density evolution – numerical and experimental results of pure NiAl sintering with pressure 5 and 30 MPa and sintering temperature of: a) $T_\mathrm{s} = 1400°\mathrm{C}$, b) $T_\mathrm{s} = 1350°\mathrm{C}$, c) $T_\mathrm{s} = 1300°\mathrm{C}$.

a)

b)

c)
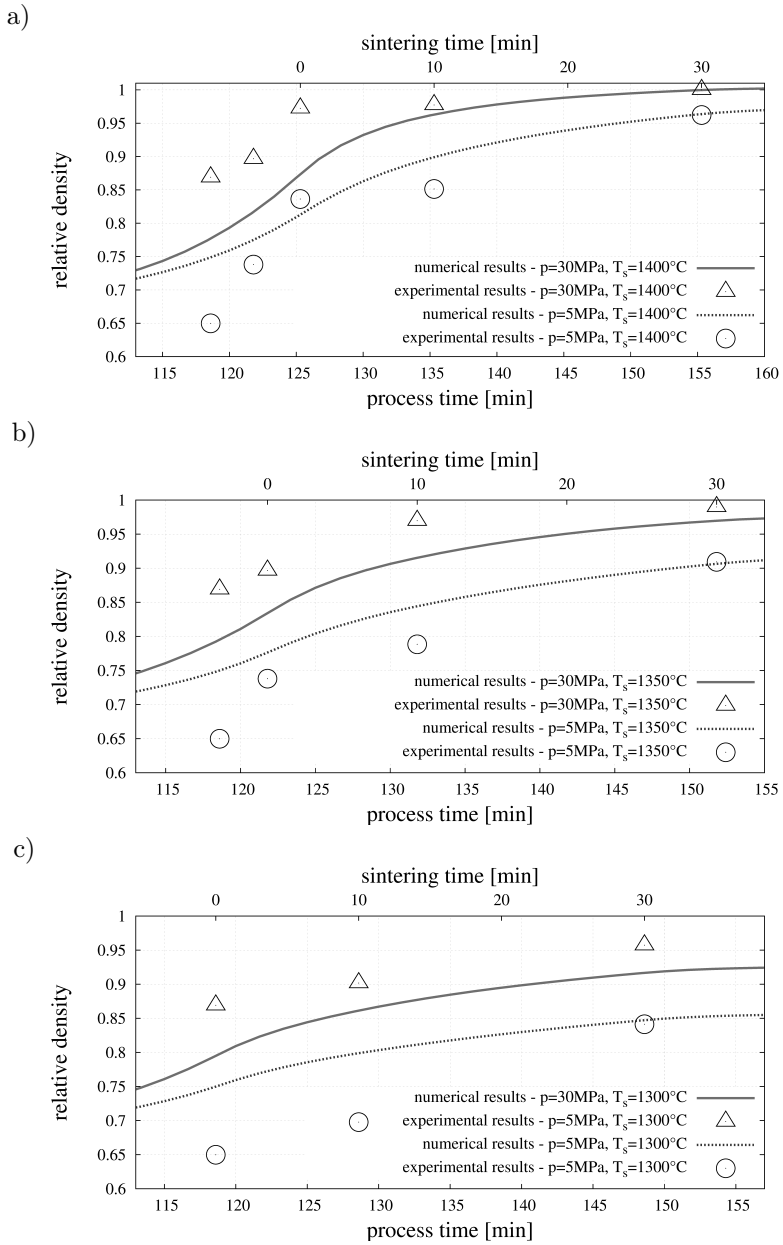
Figure 5.40. Density evolution – numerical and experimental results of pure alumina sintering for pressure 5 and 30 MPa and sintering temperature of: a) $T_s = 1400°C$, b) $T_s = 1350°C$, c) $T_s = 1300°C$.

a)

b)

c)
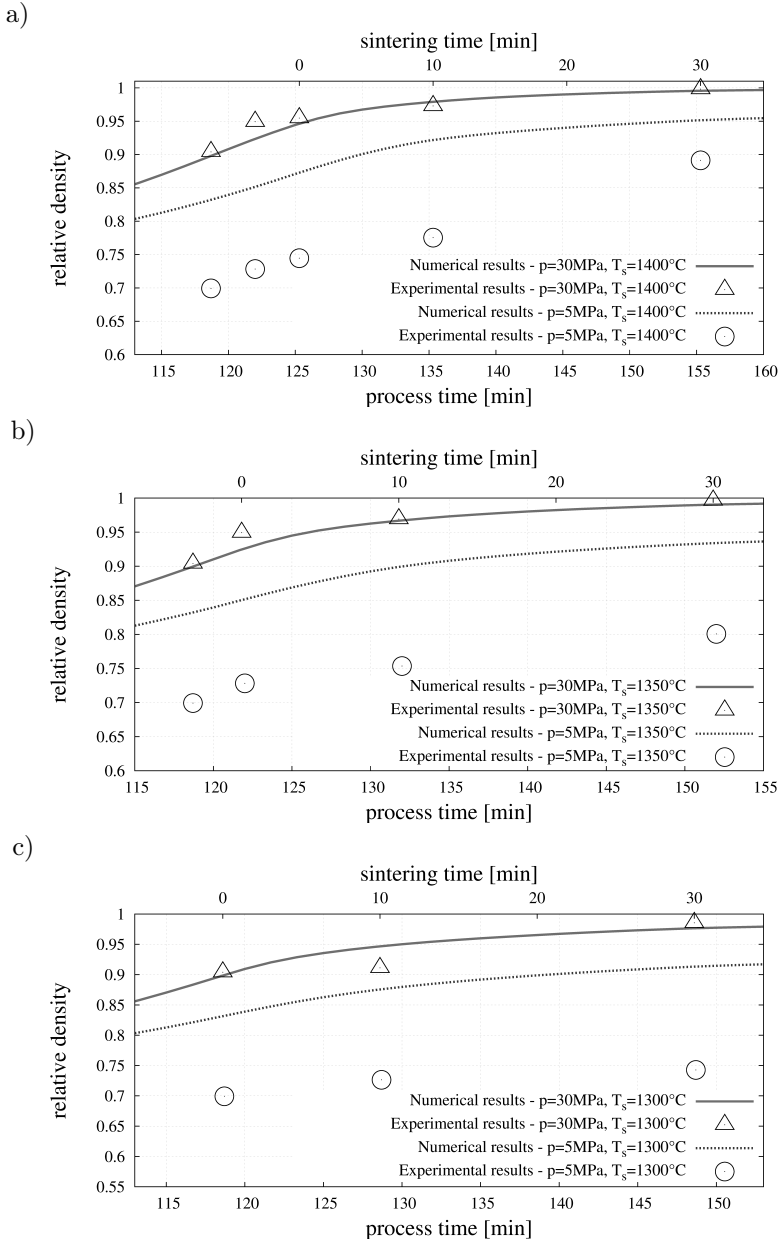
Figure 5.41. Density evolution – numerical and experimental results of composite NiAl-Al$_2$O$_3$ powder sintering for pressure 5 and 30 MPa and sintering temperature of: a) $T_s = 1400°$C, b) $T_s = 1350°$C, c) $T_s = 1300°$C.

Due to this heterogeneity of alumina microstructure, the real sintered material cannot obtain a relatively high densification. However, the intermediate stage of aluminium oxide's sintering begins with the changes in particle boundaries and the shape of pores. Hence, the shapes of powder particles correspond much more to the form of discrete elements, which is reflected by a better agreement of results.

The comparison of a numerical and an experimental results of composite relative density brought a number of conclusions. First of all, the numerical representations of all composite sintering processes with external pressure of 30 MPa are nearly ideal to experiments results – numerical lines highly cover the experimental density points showing a really good correspondence. Second fact of a current analysis refers to the failure of the agreement between composite numerical and experimental results obtained from sintering in 5 MPa of external pressure. This mismatch seems to be caused by two reasons. Just like in case of pure alumina powder, at the beginning of sintering process the powder particles of Al_2O_3 are characterized by a non-ideal spherical shapes, whereas discrete elements are implemented to be ideally spherical. It is rather obvious that spherical particles affect the decrease of porosity, thus the numerical simulations indicates higher degree of densification relative to experimental specimens with non-spherical particles of alumina powder. At the intermediate and the final stage the agreement between composite numerical and experimental results have not be improved contrary to a pure alumina powder sintering. This effect can be explained by a not fully representative adhesive model of the contact between NiAl and Al_2O_3 discrete elements, which has been based on the viscoelastic sintering model. The penetration of 'mixed' contact particles depends on the applied external pressure and the material viscous resistance. This material property is calculated from Eq. (4.40) and concerned the diffusion-dependent viscosity, which seems to be unsuitable for adhesive interaction. Inconsistency of numerical and experimental results shows the importance of an application of proper model of particle adhesion with its all specific features.

Summary

A number of numerical simulations have been performed in order to verify, calibrate and validate the discrete element model of powder metallurgy and sintering. Firstly, two particle sintering has been simulated in order to assess the performance of the newly developed viscoelastic model in comparison to the standard viscous model. While general agreement in the results has been observed it has been found out that the new model offers much better numerical

efficiency since it enables the use of much larger time steps in the explicit time integration of equations of motion. This is an important advantage of the newly developed model.

Afterwards, the model has been used to simulate the real powder metallurgy process with its all stages. In order to represent the actual microstructure of the sintered material, initially dense specimens have been generated by a special original algorithm which allows to obtain particle size distribution equivalent to the particle size distribution in the real powders. The model has been calibrated using the experimental results for a selected case of the pressure and sintering temperature, and then validated with the experimental results of the processes with other sintering process parameters. A very agreement between numerical and experimental results has been obtained for the intermetallic and partially for the alumina material. Validation for the composite material was not quite satisfactory. This shows a necessity of further investigations to improve the results. Despite observed deficiencies it can be stated that the model validation was successful. The results prove a correct performance of the numerical model. The model represents correctly phenomena occurring during the powder metallurgy process, such as the density and volume changes and its dependence on the sintering process parameters. This particular achievement makes the numerical model effective and suitable tool to analysis and optimization of powder metallurgy processes.

Analysis of stresses during and after powder metallurgy process

Introduction

Macroscopic deformation and microstructural changes during sintering occur under a complex state of stresses induced by sintering driving forces, applied pressure and temperature changes. Some of the most frequent defects in sintered materials such as cracks and shape distortions are associated with stresses during and after the sintering process. Degradation of composite materials manufactured by powder metallurgy due to progressive growth of microcracks (Fig. 6.1a) is caused by a concentration of residual stress in the material after powder metallurgy process.

a)   b)
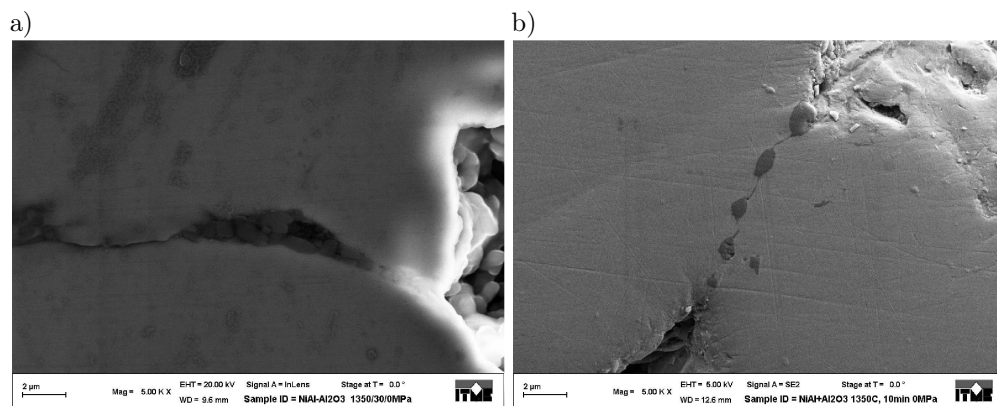
Figure 6.1. SEM images of NiAl/Al$_2$O$_3$ composite: a) material failure on the particle boundary area, b) ceramic distribution on the particle boundary of intermetallic particles.

Residual stresses are mainly induced by the difference in thermal expansion of the two interacting phases during the cooling stage. Residual stresses are accumulated in the areas of cohesive necks and interfaces. Location of the small

particle reinforcements in a cohesive connection between the bigger matrix particles (Fig. 6.1b) and irregular shape of the pores can contribute to concentration of thermal stress [225]. This shows that determination of the stresses in the sintered composite material is an important practical problem. Knowledge of the stresses would be useful in optimization of the material and manufacturing process aiming at minimization of the danger of microcracking.

The purpose of this section is to demonstrate possibilities of stress analysis using the developed model of a powder metallurgy process. Evaluation of microscopic and macroscopic stresses during and after the powder metallurgy process will be presented.

6.1 Determination of stresses in the numerical model

6.1.1 Evaluation of microscopic stress

Microscopic observations of the fractures of the composite microstructures in Figs. 3.26a and 3.26b reveal fractures both in the body of single particles and/or in the cohesive connections between particles, named transgranular and intergranular fracture modes, respectively. This shows the necessity to consider the stresses both in the necks and in the particles.

Microscopic stresses in the cohesive necks

According to the two-particle sintering model presented in Subsec. 4.5.1 and Subsec. 4.5.2, the interaction force between particles is transmitted through the neck described by the circle cross section area with a diameter of a (Fig. 6.2). The total average stress σ in the neck during the sintering is the sum of the stress in the Maxwell element σ^{ev} and the induced by sintering driving force σ^{sint}:

$$\sigma = \sigma^{\mathrm{sint}} + \sigma^{\mathrm{ev}}, \tag{6.1}$$

where

$$\sigma^{\mathrm{sint}} = \frac{F_{\mathrm{n}}^{\mathrm{sint}}}{A_{\mathrm{gb}}}, \tag{6.2}$$

$$\sigma^{\mathrm{ev}} = \frac{F_{\mathrm{n}}^{\mathrm{e}}}{A_{\mathrm{gb}}} = \frac{F_{\mathrm{n}}^{\mathrm{v}}}{A_{\mathrm{gb}}} \tag{6.3}$$

with F^{sint} being the sintering driving force, F^{ev} – the force in the Maxwell element, A_{gb} – the cross-sectional area of the cohesive neck:

$$A_{\mathrm{gb}} = \pi a^2. \tag{6.4}$$

After the sintering process – $\sigma^{\text{sint}} = 0$ – the residual stresses arise from the elastic component of the forces remaining after removing the load.
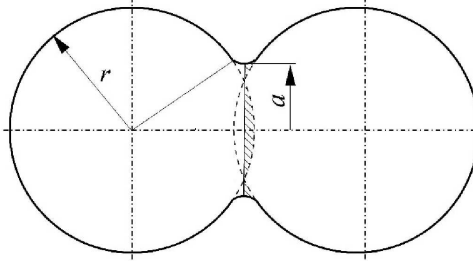
Figure 6.2. Two-particle model of sintering.

Microscopic stresses in the discrete element bodies

Let us consider a particle surrounded by n_c particles as it is shown in Fig. 6.3. The average stress $\boldsymbol{\sigma_p}$ in the considered particle i is given by the following formula, cf. [227]:

$$\boldsymbol{\sigma_p} = \frac{1}{V_p} \sum_{j=1}^{n_i^c} \mathbf{s}_{ij}^c \otimes \mathbf{F}_{ij}^c, \tag{6.5}$$

where V_p is the element volume, $\mathbf{s}_{ij}^c$ — vector connecting the element center with the contact point, $\mathbf{F}_{ij}^c$ – the contact force between the particles i and j, and the symbol $\otimes$ denotes the outer (tensor) product. The contact force $\mathbf{F}_{ij}^c$ and the vector $\mathbf{s}_{ij}^c$ are shown in Fig. 6.3. Since the particle in a general case is not in equilibrium the tensor $\boldsymbol{\sigma_p}$ obtained from Eq. (6.5) can be non-symmetric. It can be symmetrized as follows:

$$\boldsymbol{\sigma_p^{\text{sym}}} = \frac{\boldsymbol{\sigma_p} + \boldsymbol{\sigma_p}^{\text{T}}}{2}. \tag{6.6}$$

Furthermore, the stress tensor $\boldsymbol{\sigma_p^{\text{sym}}}$ can be decomposed into the deviatoric and hydrostatic (mean) stress, $\boldsymbol{\sigma_p^{\text{dev}}}$ and $\boldsymbol{\sigma_p^{\text{hyd}}}$:

$$\boldsymbol{\sigma_p^{\text{sym}}} = \boldsymbol{\sigma_p^{\text{dev}}} + \boldsymbol{\sigma_p^{\text{hyd}}} = \boldsymbol{\sigma_p^{\text{dev}}} + \mathbf{I}\sigma^{\text{m}}, \tag{6.7}$$

where σ^{m} is the mean stress

$$\sigma^{\text{m}} = \frac{\sigma_{xx} + \sigma_{yy} + \sigma_{zz}}{3} \tag{6.8}$$

and $\sigma_{xx}, \sigma_{yy}, \sigma_{zz}$ are the components of the stress tensor. The mean stress given by Eq. (6.8) will be used later as a suitable parameter to characterize if the particle is subjected to tension or compression.
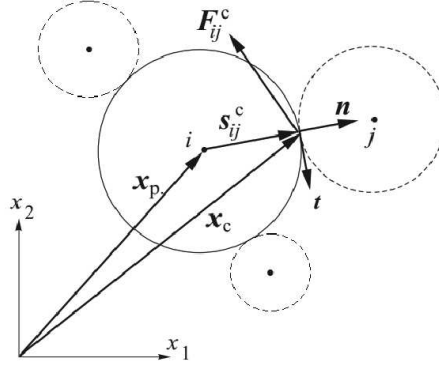
Figure 6.3. Definition of inter-particle interaction [226].

6.1.2 Evaluation of macroscopic stress

Effective macroscopic variables and properties in micromechanical models can be determined by various analytical and numerical homogenization and averaging methods [228–233]. In this work, averaging methods based on the concept of the representative volume element (RVE) will be used [234, 235]. Given constant (averaged) stresses in particles expressed by Eq. (6.5), the average stress in the representative volume element can be calculated as, cf. [227, 236]:

$$\overline{\boldsymbol{\sigma}} = \frac{1}{V_{\mathrm{RVE}}} \sum_{p \in V_{\mathrm{RVE}}} V_p \boldsymbol{\sigma}_{\mathbf{p}} = \frac{1}{V_{\mathrm{RVE}}} \sum_{p \in V_{\mathrm{RVE}}} \sum_{j=1}^{n_i^{p,c}} \mathbf{s}_{ij}^c \otimes \mathbf{F}_{ij}^c. \tag{6.9}$$

The expression (6.9) for the average stress over the representative volume can be written in an alternative equivalent form, cf. [236]:

$$\overline{\boldsymbol{\sigma}} = \frac{1}{V_{\mathrm{RVE}}} \sum_{c=1}^{N_c} \mathbf{L^c} \otimes \mathbf{F^c}, \tag{6.10}$$

in which summation is over all N_c contacts in the representative volume element, $\mathbf{F^c}$ is the total contact force for each contact, V_{RVE} is the volume of RVE, and $\mathbf{L^c}$ is the so-called branch vector connecting the centroids of two particles, for two particles i and j defined as follows:

$$\mathbf{L^c} = \mathbf{x_p^{(i)}} - \mathbf{x_p^{(j)}}. \tag{6.11}$$

Tensor $\overline{\boldsymbol{\sigma}}$ can be symmetrized analogously to Eq. (6.6). Equation (6.10) will be used later in this work to calculate macroscopic stresses taking the whole specimen as the representative volume element.

6.2 Stress analysis results

6.2.1 Evolution of the macroscopic stress

Stress analysis has been performed for manufacturing of the composite specimen NiAl/20%Al$_2$O$_3$ with the following process parameters: sintering temperature $T_s = 1400°$C, sintering time $t_s = 30$ min and external pressure $p = 30$ MPa. The total $\overline{\sigma}$, sintering driving $\overline{\sigma}^{\text{sint}}$ and viscoelastic $\overline{\sigma}^{\text{ev}}$ macroscopic stresses have been calculated from Eq. (6.10) using the corresponding force components, F_n, F_n^{sint} and F_n^{e}, respectively. Figure 6.4 shows the evolution of the total macroscopic stress in the composite specimen during the whole powder metallurgy process. The intervals corresponding to each stage: loading, heating, sintering, cooling and unloading have been shown in order to enable a better understanding of stress changes.
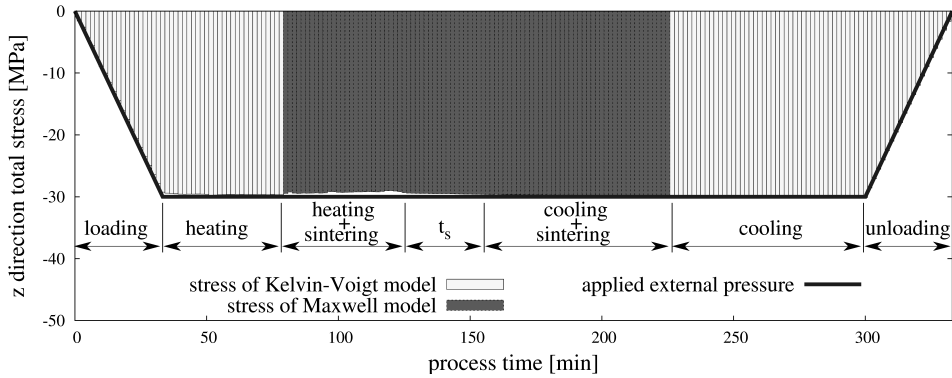
Figure 6.4. Evolution of total macroscopic stress of the hot pressing process in z direction.

The graph presents the evolution of total macroscopic stress in z direction, in which the external pressure was applied. Comparison of the evolution of total macroscopic stress in x, y and z directions, respectively $\overline{\sigma}_{\text{xx}}$, $\overline{\sigma}_{\text{yy}}$ and $\overline{\sigma}_{\text{zz}}$, is presented in Fig. 6.5.

At the beginning of powder metallurgy process, the external pressure is applied and the total macroscopic stress of the composite in z direction arises to reach the value close to 30 MPa over a dozen minutes. At this moment the proceed material is in mechanical equilibrium – the total macroscopic stress is equal to the value of the external pressure. After this point, a very fine variation of total macroscopic stress due to the effect of thermal expansion resulting from the increase of temperature can be seen. As the temperature of sintering activation for each material contact type is reached, the model transition from Kelvin-
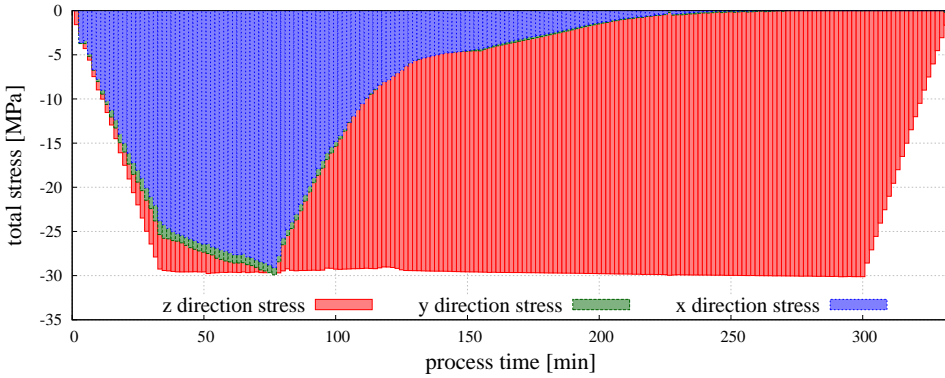
Figure 6.5. Evolution of total macroscopic stress of the hot pressing process in x, y and z direction.

Voigt to Maxwell one takes place and the sintering is started. The beginning of sintering stage is accompanied by appearance of the resultant force of sintering driving stress which acts in parallel with viscoelastic force in the Maxwell branch. The evolution of the sintering driving and viscoelastic stresses in the three normal directions of particle contact is presented in Fig. 6.6a and 6.6b, respectively.

a)

b)
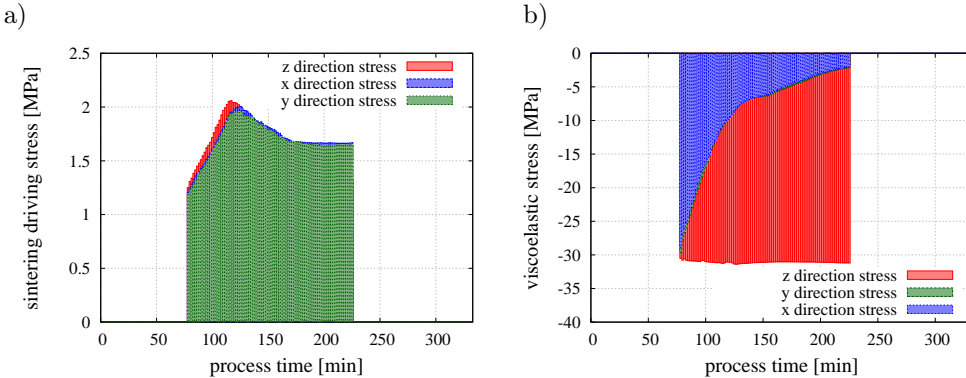
Figure 6.6. Evolution of: a) sintering driving macroscopic stress, b) viscoelastic macroscopic stress of the sintering process in x, y and z direction.

Sintering driving stress in all the directions is equal as it can be expected since the sintering driving stress should be an isotropic field. This confirms the correct performance of the model. Comparing to the magnitude of the external pressure, the value of the sintering driving stress is relatively small. The maximum value of the sintering driving stress, 2.05 MPa, corresponds to 6% of the

value of the applied external pressure. The obtained values are consistent with the literature reports on theoretical and numerical analysis of sintering driving stress [237, 238]. Macroscopic stress resulting from the sintering driving force has a positive value and together with applied external load is responsible for material densification and decreasing of the porosity of the sintered powder. The material resistance is manifested by the viscoelastic macroscopic stress. Evolution of the three principal viscoelastic macroscopic stresses is shown in Fig. 6.6b. It can be seen that before sintering all the three stress components are nearly equal which is expected since the state of hydrostatic compression have been applied. With the progress of sintering the radial stresses gradually decrease nearly to zero due to radial shrinkage of the specimen and finally the state of uniaxial compression is obtained. In the middle and the final stage of sintering the viscoelastic macroscopic stress in z direction stabilizes around the value of 30 MPa, which indicates the balances of material resistance with external pressure and sintering driving stress. The graphical representation of total, viscoelastic and sintering driving macroscopic stress in three main directions for the whole period of simulation is presented in Figs. 6.7.
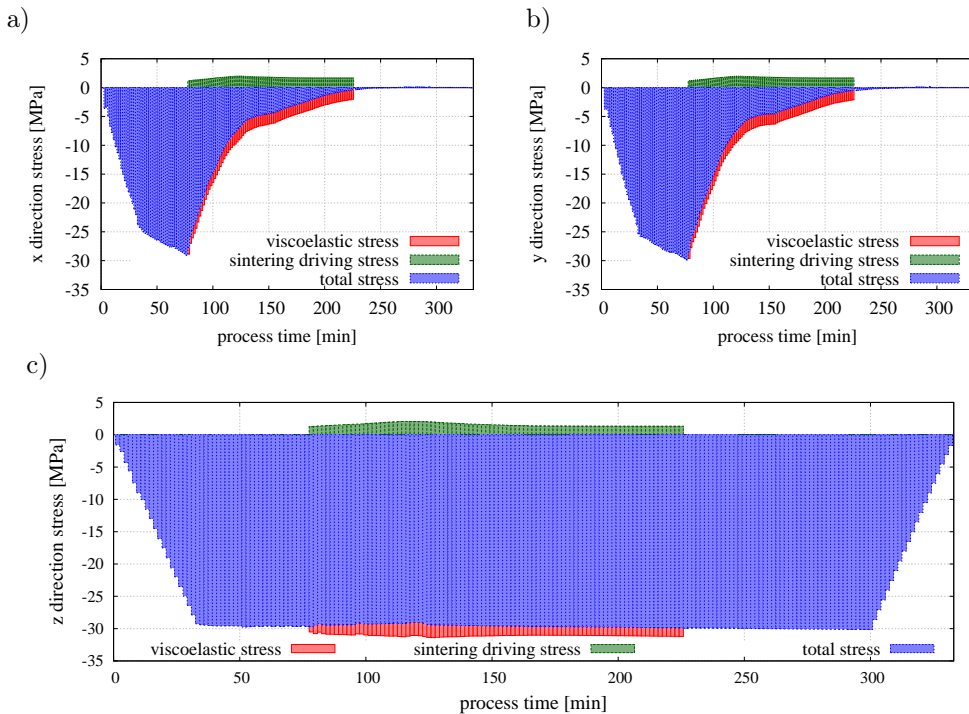
Figure 6.7. Evolution of the total, sintering of the driving and viscoelastic macroscopic stress: a) in x direction, b) in y direction, c) in z direction.

The values of the principal macroscopic stresses at the final stage of sinter-ing (t_s = 30 min) and after unloading are given in Table 6.1. As it is expected the macroscopic stresses after the process are nearly zero. A very small values obtained because the equilibrium of the particles is not perfect. It should be re-marked, however, that zero macroscopic stresses do not signify that microscopic residual stresses are also zero – it only means that microscopic residual stresses are self-equilibrated. Microscopic stress distribution will be investigated below.

Table 6.1. Summary of macroscopic stresses in three main directions at the final stage of sintering and the end of powder metallurgy process [MPa].

Direction/	Final stage of sintering – t_s = 30 min			End of the process
stress	Sintering driving	Viscoelastic	Total	Residual total
XX	1.8	−6.1	−4.3	−0.00006
YY	1.8	−6.3	−4.5	−0.000001
ZZ	1.5	−31.1	−29.6	−0.000075

6.2.2 Microscopic stress in the cohesive bonds

Microscopic stresses in the bonds have been determined in the necks for the problem which was used above for the analysis of macroscopic stresses. The stresses have been determined for all active inter-particle cohesive bonds, thus for those which neck radius a has not achieved the equilibrium state yet. Figure 6.8 presents composite specimen during hot pressing with the network of cohesive bonds represented by beams connecting the centres of interacting particles.
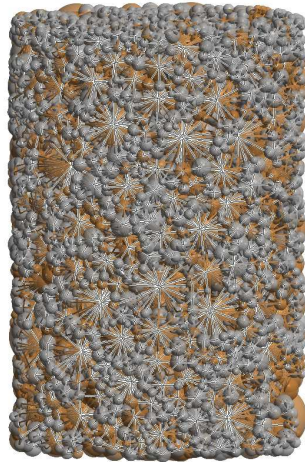
Figure 6.8. Network of particle connections during sintering.

Using Eqs. (6.1), (6.2) and (6.3) the total σ, sintering driving σ^{sint} and viscoelastic σ^{ev} microscopic stresses have been calculated.

Microscopic stresses have been determined at the two special moments of hot pressing process: at the end of sintering time ($t_{\text{s}} = 30$ min) and after cooling and unloading. Figure 6.9 presents the distribution and histogram of sintering driving microscopic stresses in the final stage of sintering (before material cooling). Similarly, Fig. 6.10 shows the results of viscoelastic microscopic stresses.

a)   b)
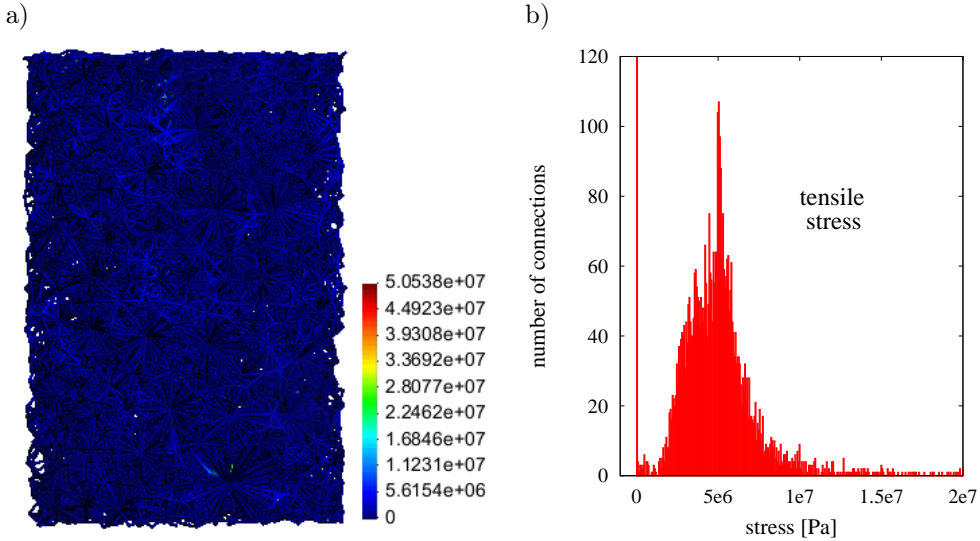
Figure 6.9. The results of sintering driving microscopic stresses at the final stage of sintering: a) distribution in the volume, b) histogram.

As it was presented in the previous paragraph, the value of sintering driving stress is rather insignificant comparing to the total stress. Mean value of the sintering driving microscopic stress is around 2 MPa and the most of connections are in the range from 0 to 10 MPa. Sintering driving microscopic stress affects the attraction of particles, however, in the view of the above, the applied external pressure has a more crucial impact on the powder densification.

Attractive contact interaction resulting from the impact of sintering driving and external force stress is balanced by the viscoelastic resistance of material. Analyzed final stage of sintering is characterized by equilibrium of sintered material, where the motion of particles in the contact is minimum and practically material compaction does not occur. The viscoelastic microscopic stress has both positive and negative value thus it indicates tensile and compressive character of interaction (Fig. 6.10b).

a)   b)
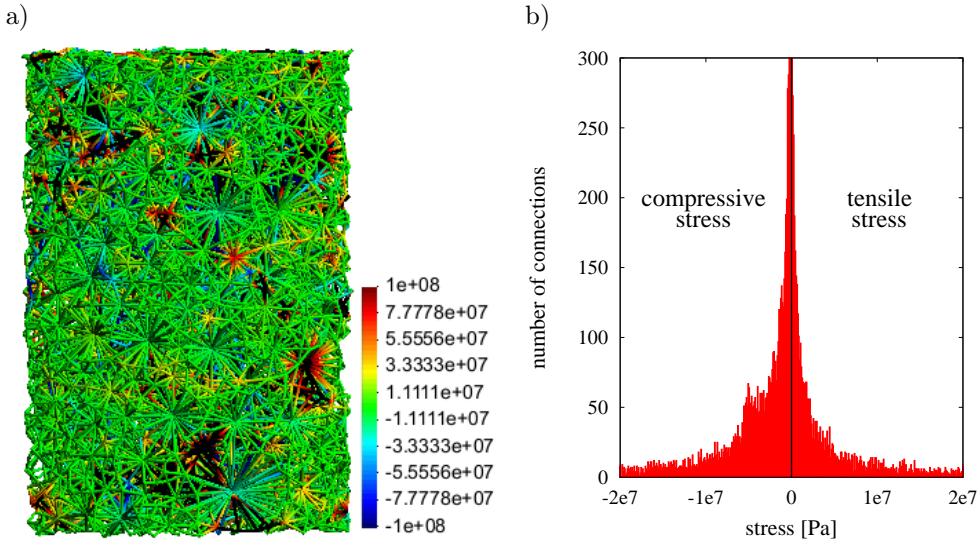
Figure 6.10. The results of viscoelastic microscopic stresses at the final stage of sintering: a) distribution in the volume, b) histogram.

Furthermore, it can be seen the advantage of the compressive stresses (negative values) over the tensile ones (positive), which is related to material resistance from the external pressure application. It should also be noted that in certain locations of the composite specimen, viscoelastic microscopic stresses achieve significant values, both tensile and compressive – even around 52 GPa. Naturally, obtained results of maximum and minimum microscopic stresses are unrealistic and result from no occurrence of cracking model of interacting particles.

Due to the model assumptions and following the Eq. (6.1), viscoelastic stress is the major component of total microscopic stress in the Maxwell element. Figure 6.11 introduces the comparison of histograms of total microscopic stress during (the final stage of sintering) and after hot pressing process (residual stresses). The properties of composite material after the process (after the cooling), comparing to properties during the sintering, are various due to no more effect of temperature and compressive pressure. After the sintering, the specimen is subject to other conditions, what is reflected in the different form of the microscopic stress distribution.

Total microscopic stress (Fig. 6.11a) is the sum of sintering driving stress (Fig. 6.9b) and viscoelastic stress (Fig. 6.10b). It can be seen the combination of tensile stresses (impact of sintering driving and viscoelastic stress) and
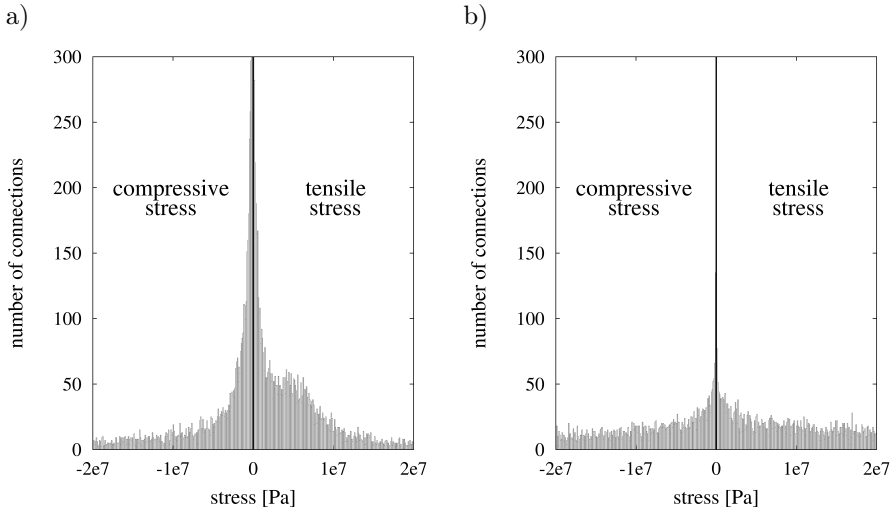
Figure 6.11. Histograms of total microscopic stresses: a) in the final stage of sintering, b) after sintering (residual microscopic stresses).

compressive stresses (impact of viscoelastic stress as the effect of response of the material to applied external force). In the second case (Fig. 6.11b), after the hot pressing the only interaction is the viscoelastic one. Sintering driving stress is deactivated (no temperature effect – sintering driving force equal zero) and the loading of punch is removed (external force equal zero). In this case, the residual microscopic stresses indicate the compressive and tensile character and similar values, which proves that sintered composite specimen occurs in the stress equilibrium.

6.2.3 Microscopic stress in the discrete element bodies

Averaged microscopic stresses in the particle bodies have been evaluated during and after the hot pressing process investigated in the previous subsections. The total microscopic stress in each discrete element was calculated from Eq. (6.5). In order to compare the stresses at specific stages of the hot pressing, the histograms of the microscopic stresses of the whole volume of the $NiAl/Al_2O_3$ specimen have been presented. Figures 6.12 show the stress distributions at the four stages: after loading (before heating), in the final stage of sintering, after cooling (before unloading) and finally after unloading, respectively.

In the first case it can be seen the material response to the external pressure in the form of compressive stresses. The stress distribution is changed after
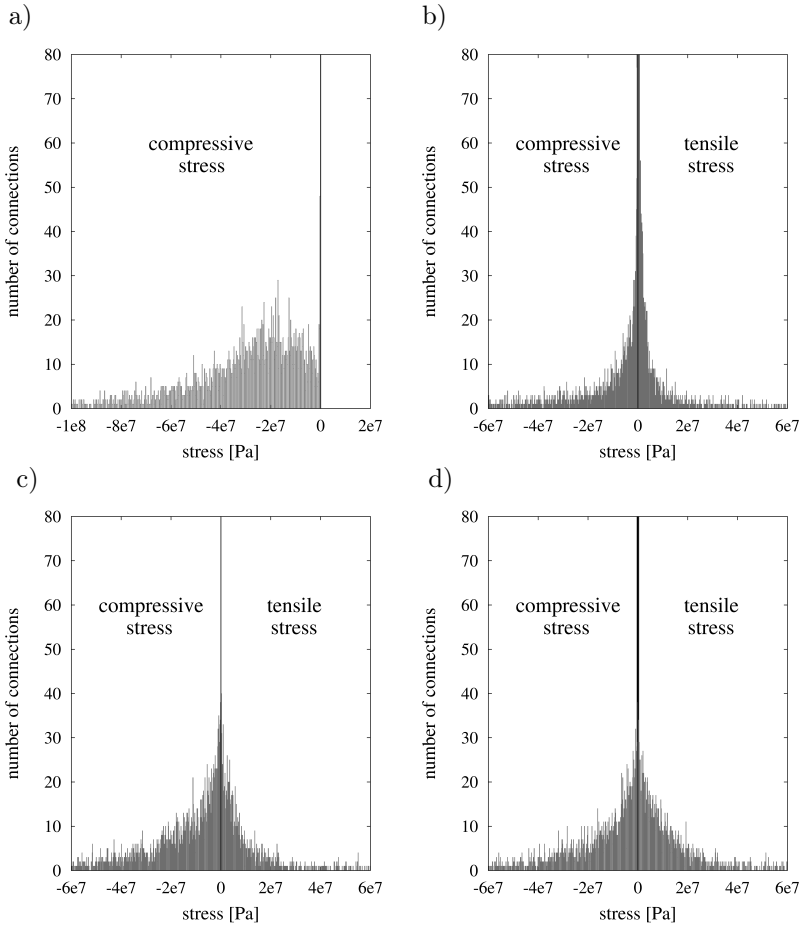
Figure 6.12. Distribution of particle total microscopic stresses: a) after loading, before heating ($t = 33$ min), b) in the final stage of sintering ($t = 155$ min, $t_s = 30$ min), c) after cooling, before unloading ($t = 293$ min), d) after unloading.

sintering activation (Fig. 6.12b). Sintering stage is characterized by occurrence of sintering driving stresses and combination of viscoelastic tensile and compressive stresses. Sintering driving stresses are responsible for discrete element attraction and indicate the tensile character, which can be seen in Fig. 6.9b. The values of sintering driving microscopic stress range from 0 to 10 MPa and are insignificant comparing to the viscoelastic ones. Furthermore, the cohesive particle interaction highly affects the maximum and minimum values of stresses, which was presented in Table 6.2. The graphical distribution of the maximum and minimum values of particle total microscopic stresses can be seen in Fig. 6.13.

Table 6.2. Evolution of maximum and minimum values of averaged particle microscopic stresses [MPa] during the hot pressing process.

Parameter	Hot pressing stages			
	After loading $t = 33$ min	Final stage of sintering $t = 155$ min	After cooling $t = 293$ min	After unloading $t = 330$ min
Max. value	0.2	452.6	532.3	540.6
Min. value	-463.4	-1861.6	-2292.3	-2201.2
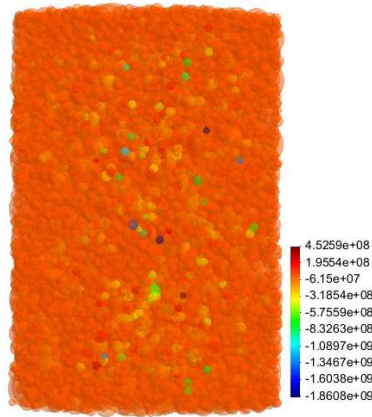
Figure 6.13. Graphical distribution of particle total microscopic stresses in the final stage of sintering.

Presented figure leads to the obvious conclusion that the large local stresses are mostly generated in the smallest particles. The smallest particles are mainly subjected to cracking both during the sintering and cooling. As in the case of neck microscopic stress analysis, particle microscopic stress achieves huge compressive values. Everything points, that the application of the cracking model may decrease these large values of maximum and minimum microscopic stresses and provide more realistic analysis.

As the sintering ends and the specimen is cooled, sintering driving microscopic stress are deactivated and the only particle interaction is the viscoelastic one. This stage of the process is similar to the first considered one (after loading, before cooling), however the sintering has affected the specimen microstructure by creating the cohesive necks. Due to this fact, the both compressive and tensile stress had been generated, however the compressive ones prevail. Moreover, the maximum and minimum value of stress furthermore increased during the cooling stage because of the effect of thermal expansion.

After unloading, in the end of the process, the values of residual microscopic stress indicate the balance between positive (tensile) and negative (compressive) values of microscopic stresses.

Further analysis concerns the microscopic stress determined and analyzed separately for the intermetallic NiAl and ceramic Al_2O_3 particles. The comparison of the results of obtained microscopic stresses of each phase is presented in Table 6.3. Fig. 6.14 presents the histograms of microscopic stress of each phase in the final stage of sintering and after the unloading.

Table 6.3. Statistical parameters of determined discrete element microscopic stresses [MPa] of each phase in NiAl/Al_2O_3 specimen.

Parameter	Final stage of sintering		End of the process	
	NiAl	Al_2O_3	NiAl	Al_2O_3
Mean value	−10.3	−16.1	1.9	−25.3
Standard deviation	51.6	95.7	53.6	110.6
Maximum value	374.2	452.6	540.6	387.4
Minimum value	−814.3	−1861.6	−806.5	−2201.2

a)   b)
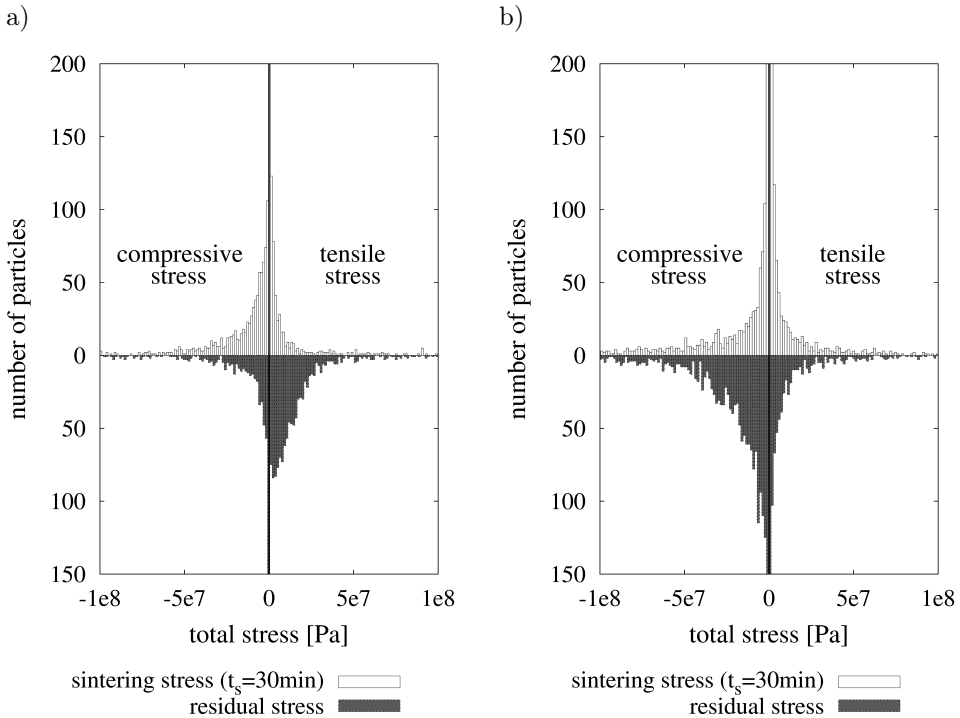
Figure 6.14. The histograms of particle total microscopic stresses in the final stage of sintering and at the end of the process (after cooling) of: a) NiAl, b) alumina particles.

The values of microscopic stresses in the final stage of sintering of both materials, NiAl and Al$_2$O$_3$, are predominantly negative (compressive), which is consistent with the histograms in Fig. 6.14, where compressive stresses predominate. In turn, the state of unloading and after cooling is characterised by different signs of the mean stresses of interacting phases. The mean value of the microscopic stress in the NiAl particles is positive, which indicates the tensile stress in the intermetallic particles. A negative value of the mean value of the microscopic stress in the Al$_2$O$_3$ particles indicates the compressive state of stress. Moreover, the unfavourable impact of thermal residual stresses can be seen in the extreme values. Comparing to the state of stress at the final stage of sintering, the maximum (tensile) stress grows in the case of intermetallic phase and the minimum (compressive) stress increases in the case of alumina particles.

Presented results are in agreement with theoretical predictions regarding the cooling mechanism of the composite material. The differences in the coefficients of thermal expansion of two-phase material produces the effect of compression of the particles with lower ability to shrinkage during the cooling. Ceramic particles shrink harder and slower, whereas the intermetallic ones, with the higher value of coefficient of thermal expansion, deform easier and quicker. Therefore, the intermetallic particles compressed the ceramic particles introducing the large states of stress in the particles contacts. Presented contact interaction between
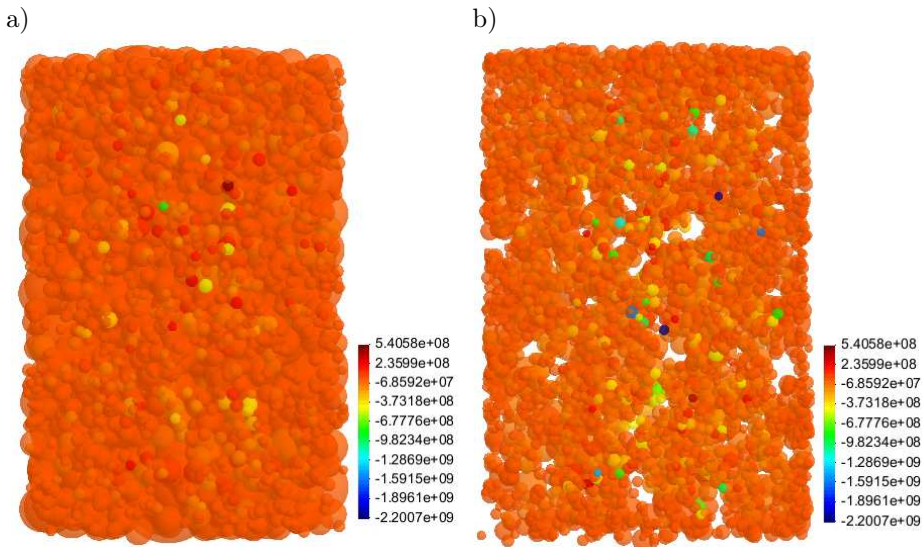
Figure 6.15. Graphical distribution of particle total microscopic stresses at the end of the process (after cooling) of: a) particles of intermetallic NiAl, b) particles of ceramic Al$_2$O$_3$.

the intermetallic and ceramic particles induce the occurrence of state of stress, which can overweight the strength of particles and consequently leads to the formation of the microcracks. Generally, in the ceramic phase of the metal-ceramic composite compressive stresses prevail, but large local tensile stresses may also appear [239]. Ceramic particles are sensitive to microcracking due to the insignificant tensile strength. As it is shown in Fig. 6.15, in spite of the mostly small alumina particles achieves the large values of compressive stresses, the significant tensile stresses can be also found.

Summary

Evaluation of stresses in the discrete element model of a powder metallurgy process has been presented. Stress analysis has been performed for the selected case of manufacturing of the NiAl-Al$_2$O$_3$ composite specimen. The stresses during and after the powder metallurgy process have been investigated at two levels of material scale: micro- and macroscopic ones. Microscopic stresses have been defined as average stresses in the cohesive bonds and in the particle bodies. Averaged macroscopic stresses have been calculated by averaging over the whole specimen treated as the representative volume element. The results were analysed considering different kinds of microscopic stresses: total, viscoelastic and sintering driving. Presented results are in agreement with theoretical predictions referred to the material states during hot pressing process. The knowledge of residual stresses is important for possible design of the material and optimization of the manufacturing process aiming to minimize a risk of possible material defects.

7

Concluding remarks

7.1 Summary

Proposed thesis has presented the numerical and experimental study of powder metallurgy process with the special attention to sintering stage. A summary of the main results and achievements of the thesis is presented as follows:

- Original numerical model of the hot pressing process has been formulated and implemented within the discrete element framework. The presented model represents the initial compaction of the powder and further consolidation as the effect of sintering. The stage of powder compaction has been modeled using the cohesionless contact model with friction, where a spring and a dashpot are connected in parallel (the Kelvin-Voigt system). The thermo-viscoelastic model of sintering has been obtained by adding a spring and thermal element (the Maxwell system) to the two-particle viscous model of sintering commonly used in the literature. The elastic component allows for a better redistribution of forces and stresses in large particle assembly. The thermal element, related to the effect of the thermal expansion, allows to take into account the influence of the temperature evolution during the whole process. The transition between the Kelvin-Voigt and Maxwell models has been characterized by an algorithm ensuring a smooth and numerically stable change. Special procedure of integration of the equations of motion, neck growth equation and evolution of the viscous and elastic forces has been implemented. The proper and stable numerical performance of presented models has been achieved by a precise selection of the time step and the application of the upscaling procedure.

- Literature studies have been carried out to define the relations of material parameters of sintering model and estimate the values of all required parameters. The analysis has concerned the determination of diffusive parameters, as the main mass transport mechanisms of the sintering pro-

cess of the current model, and the determination of surface energy as the sintering driving force of particle attraction.

- Two-particle simulations of the sintering process have been performed to verify the new developed viscoelastic Maxwell model and well-known viscous model. Numerical simulations have been held to assess the efficiency performance of both models. While general agreement in the results has been observed it has been found out that the new model offers much better numerical efficiency since it enables the use of much larger time step in an explicit time integration of equations of motion. This is an important advantage of the newly developed model.

- In order to represent the real microstructure of material powder after mixing, the special algorithm of the generation of the discrete element geometrical model has been implemented. The presented algorithm consists of two stages: the generation of initial loose particles and compaction by dynamics method. The generation of geometrical model has been applied to one-phase powders: intermetallic NiAl and ceramic Al_2O_3, and the mixture of 80% vol. intermetallic NiAl and 20% vol.ceramic Al_2O_3 powders. Obtained geometrical models satisfy all the main requirements of real powder body after mixing, such as the isotropy of material or the real distribution and size of considered powders.

- Several numerical simulations have been performed to calibrate and validate the discrete element model of powder metallurgy. Powder metallurgy investigation has been performed on the example of particulate materials: the intermetallic NiAl, ceramic Al_2O_3 and NiAl-Al_2O_3 composite materials. Satisfactory results of calibration and validation process prove the correct performance of the numerical model. The discrete element modeling of powder metallurgy process has allowed to obtain the numerical representation of sintered specimens in the case of various combination of sintering process parameters. Moreover, the simulations of sintering provide the realistic data during the process. This particular achievement makes the numerical model effective and suitable tool to analysis phenomenon occurring during the powder metallurgy process. In spite of a great potential of the presented model, some particular features of discrete element modeling of sintering have to be taken into account to improve the agreement between experimental and numerical results of two-phase composite material, such as non-trivial particles shape or a suitable adhesive contact model.

- Numerical study of microscopic stress has been introduced at the example of NiAl-Al$_2$O$_3$ composite material. Microscopic stress has been determined and analysed concerning two particular places subject to stress generation: cohesive connection between the powder particles and the whole body of particles. Presented results are in agreement with theoretical predictions referred to the material states during hot pressing process. During the sintering the material is subjected to the applied external pressure and sintering driving stress indicating the combination of tensile stresses (impact of sintering driving and viscoelastic stress) and compressive stresses (impact of viscoelastic stress as the effect of material response to applied external force). In the case of the unloaded and cooled specimen, the compressive and tensile microscopic stresses show similar values, which has evidenced a state of equilibrium in the composite material.

- In order to study the microscopic stress generated at the each phase, the determination of stress of each discrete element was performed separately for the intermetallic NiAl and ceramic Al$_2$O$_3$ particles. Numerical model predicts correctly that ceramic particles are compressed by intermetallic particles during cooling stage due to the various values of the coefficients of thermal expansion. Comparing to the state of stress at sintering stage, the maximum (tensile) stresses grow more in the case of intermetallic phase and the minimum (compressive) stresses increase more in the case of alumina particles.

- Numerical averaging methods have been employed to determine the macroscopic stress of the NiAl-Al$_2$O$_3$ composite material. Macroscopic stresses have been calculated for the whole process including loading, heating, sintering, cooling and unloading. The obtained results have confirmed correct and efficient performance of the proposed numerical model. It has been found out that the macroscopic stresses are consistent with changing sintering process parameters.

- Experimental investigation of hot pressing process of several types of powders have been performed. Pure NiAl, pure Al$_2$O$_3$ and NiAl-Al$_2$O$_3$ composite specimens have been manufactured to provide the essential data for calibration and verification of the numerical model of powder metallurgy. The powders have been sintered and characterized at different combinations of sintering process parameters: temperature, pressure and time, in order to obtain the density vs. time curves.

- Sinterability of the individual two components, NiAl and Al_2O_3, and the NiAl-Al_2O_3 composite material have been compared. The evolution of density, microstructure, elastic constants and mechanical strength during the sintering has been presented, and its dependence on sintering process parameters. The results indicate a various influence of process parameters on the ceramic, intermetallic and composite properties, however the pressure increase seems to have the biggest impact. Increase of external pressure resulted in higher density and better mechanical properties even at lower temperatures. The appropriate selection of sintering process parameters allows to obtain materials with a density close to the theoretical. The presented experimental studies have brought the useful data in the context of the sintering process optimization of NiAl, Al_2O_3 and NiAl-Al_2O_3 powders.

7.2 Original elements of the thesis

The following investigated elements are the original contribution of the present study on the background of the current state of the art presented in Subsecs. 1.2 and 3.1:

- Formulation and implementation of an original thermo-viscoelastic model of a sintering process within the discrete element framework. In relation to discrete element models of sintering process presented in the literature, the new model takes into account a various deformation mechanisms: viscous, elastic and thermal, and demonstrates higher efficiency due to the application of much larger time step during integration.

- Application of discrete element modeling to hot pressing topic. Unlike other discrete element models focused only on the sintering process, presented work shows the results from all stages of hot pressing process, including loading, heating, sintering, cooling and unloading.

- Discrete element modeling of sintering of two-phase composite material. In addition to few cited papers, presented study is a one of the first effort of two-phase sintering simulation concerning more than one type of interparticle material interaction.

- Discrete element analysis of sintering and post-sintering stresses in the micro- and macroscopic scale of two-phase composite material.

- Experimental study of the evolution of material parameters (density, elastic constants, tensile strength) during the sintering process of NiAl/Al_2O_3

powders mixture. All the referred works concerning NiAl/Al$_2$O$_3$ composite have been carried out for materials sintered to the full density. Presented experimental study provides a full understanding of dependence of the macroscopic composite properties on microstructure and evolution of this relationship during manufacturing process.

7.3 Recommendations for future work

Based on the conclusion and numerical results obtained in the proposed thesis, some problems can be solved and improved during the further discrete element analysis applied to the powder metallurgy, hot pressing and sintering processes. The recommended further research would include the following tasks:

- Application of a suitable model of the adhesive particles bond. In the case of presented study of discrete element modeling of NiAl/Al$_2$O$_3$ sintering, the connection between NiAl and Al$_2$O$_3$ particles has been modeled by simplified viscoelastic diffusive model of sintering. Following assumption has brought the inconsistency of numerical and experimental results and has shown the importance of an application of a proper model of particle adhesion with its all specific features.

- Taking into account the irregular shape of the particles. Following requirement is important particularly in the case of sintering of alumina particles characterising by non trivial geometry in the initial stage of sintering. This geometrical feature of particle has reduced the agreement between numerical and experimental results of alumina sintering.

- Application of cracking model of interacting particles. Modeling of composite microscopic stress has shown that both tensile and compressive stress achieved significant and unrealistic values. Implementation of bond breakage or discrete element fracture allows to a substantial reduction of high states of stress during the sintering and cooling.

- Concerning the rotational motion of the particles and tangential interaction during sintering stage.

- Numerical modeling of powder metallurgy and sintering processes at various scales. At sintering, processes at different levels interact with one another, therefore in numerical modeling it should be considered physical phenomena occurring at various scales: atomistic, microscopic and macroscopic one. Modeling at lower scales will provide parametric information to the upper scale while the upper scale models provide boundary con-

ditions for lower scale analysis. Appropriate upscaling and downscaling methods enabling transfer between scales can be very useful and efficient tool to accurate modeling such a complex phenomenon as sintering process.

Moreover, presented results of manufacture process of novel $NiAl/Al_2O_3$ composite indicate the further development of these promising materials. In order to improve mechanical properties of NiAl matrix composites, the form and size of ceramic reinforcement can be modified. For example, the application of nanoscale powder of alumina seems to increase tensile and compressive strength, and contributes to improve the wear resistance.

Derivation of the two-particle model of sintering

Appendix A presents the derivation of the equation of particle force interaction during sintering process (Eq. (4.29)). The following equation considering the relationship between sintering driving force, sintering stress, grain boundary diffusion and geometrical parameters, has been investigated for decades [3, 58, 169, 240, 241].

The viscous and thermo-viscoelastic models of sintering, presented in Subsecs. 4.5.1 and 4.5.2, assume that dominant mechanism of mass transport during a sintering process is a grain boundary diffusion. The simplest description of diffusion process can be presented in the form of Fick's first law, which states that the flux of the diffusing species/atoms J_x (number crossing unit area, normal to the direction of flux, per second) is proportional to the concentration gradient $\mathrm{d}C/\mathrm{d}x$ and occurs in the direction of decreasing concentration (Fig. A.1). Fick's first law (in one dimension) is

$$J_x = -D\frac{\mathrm{d}C}{\mathrm{d}x}. \qquad (A.1)$$
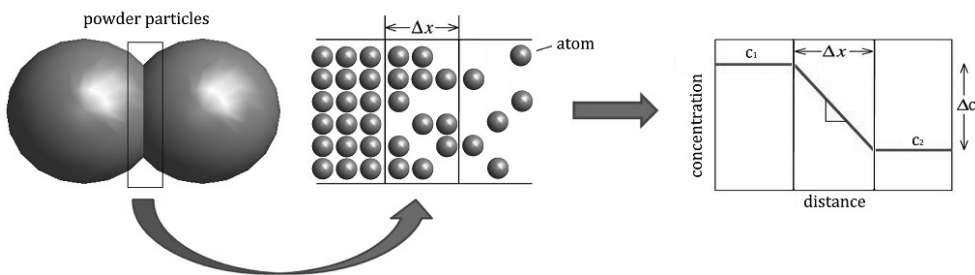
Figure A.1. Schematic of atom/vacancies diffusion during the powder sintering.

The constant of proportionality D, called the diffusion coefficient (or diffusivity), is a material property and is the most useful parameter for characterizing the rate of diffusive mass transport. It is usually a strong function of temperature and is also a function of composition.

Using the relation between chemical potential μ and concentration, the atomic flux equation dependent on a chemical potential gradients of atoms and vacancies – $\mathrm{d}\mu = \mu_\mathrm{a} - \mu_\mathrm{v}$, is given by following equation [3]:

$$J_\mathrm{x} = -\frac{DC}{\Omega \mathrm{k_B} T}\frac{\mathrm{d}\mu}{\mathrm{d}x}, \tag{A.2}$$

where $\mathrm{k_B}$ is the Boltzmann constant, Ω is the atomic volume and T is the absolute temperature.

In the case, where the grain boundary diffusion is the major and dominant mechanism of densification, the grain boundary atomic flux can be expressed as [3]:

$$j_\mathrm{gb}(x) = -\frac{D_{gb}}{\Omega \mathrm{k_B} T}\nabla\mu, \tag{A.3}$$

where D_gb is the diffusivity in the grain boundary.

Material transport in an interface of interacting particles can be written in the terms of stress [169], since

$$\nabla\sigma_\mathrm{n} = \frac{\nabla\mu}{\Omega}, \tag{A.4}$$

where σ_n is the local normal stress.

From Eq. (A.3) and Eq. (A.4), which was integrated with the appropriate geometrical boundary condition and the force balance at the grain boundary, we obtain the expression derived by Jonghe and Rahaman [169], which express the grain boundary flux at the edge of the neck:

$$j_\mathrm{gb}(a) = \frac{4D_\mathrm{gb}\Omega}{a\mathrm{k_B} T}\left[\sigma + \gamma_\mathrm{s} K(a) + 2\frac{\gamma_\mathrm{s}}{a}\sin\left(\frac{\Psi}{2}\right)\right], \tag{A.5}$$

where $j_\mathrm{gb}(a)$ is the volume of material passing out of the grain boundary at $a = x$ through unit area in unit time, σ is the average stress on the neck, γ_s is the energy of the free surface, and $K(a)$ is the sum of the principal curvatures at the edge of the neck. Curvature is defined to be positive when the center of curvature is outside of the particle [240]. It should be noted that the three terms in brackets in Eq. (A.5) will evolve in different ways as the neck grows. The

summed curvature and the term containing the dihedral angle are determined by the geometry and are termed "sintering stress". The average stress on the neck σ depends on the applied pressure, the neck size, the particle size and the particle packing density.

The term $\frac{2\gamma_s}{a}\sin\left(\frac{\Psi}{2}\right)$ is sometimes neglected since the error is small when the neck radius a is large compared to the pore curvature [169]. This would imply that the mean stress, in the absence of an applied stress, is zero. The stress gradient, and thus the local stress, caused by $\gamma_s K(a)$, remains a physically measurable entity.

Relative axial velocity can be described by the rate of approach of one particle toward the other:

$$v_{rn} = 2\dot{\phi}, \tag{A.6}$$

where $\dot{\phi}$ describes the shrinkage rate and can be expressed as

$$\dot{\phi} = \delta\frac{j(a)}{a}, \tag{A.7}$$

where δ is the thickness (width) of the grain boundary, a is the radius of the neck. Combination of Eqs. (A.5)–(A.7), we obtain:

$$v_{rn} = 2\dot{\phi} = 2\delta\frac{j(a)}{a} = \frac{8D_{eff}}{a^2}\left[\sigma + \gamma_s K(a) + 2\frac{\gamma_s}{a}\sin\left(\frac{\Psi}{2}\right)\right], \tag{A.8}$$

where D_{eff} – effective grain boundary diffusion coefficient, which is given by following expression:

$$D_{eff} = \frac{D_{gb}\delta\Omega}{k_B T}. \tag{A.9}$$

Following Parhami and McMeeking [58], $K(a)$ is the sum of the principal free surface curvatures at the edge of the grain boundary and is given by expression:

$$K(a) = -\frac{1}{s} + \frac{1}{a}\sin\frac{\Psi}{2}. \tag{A.10}$$

Coble [241] assumed that the two particles can be modeled as intersecting spheres joined by neck segments with constant s meeting at a dihedral angle Ψ [58]. When s < a < r, preservation of volume to first order gives:

$$\frac{1}{s} = \frac{4r[1 - \cos(\Psi/2)]}{a^2}. \tag{A.11}$$

Substitution of Eq. (A.11) and Eq. (A.10) into Eq. (A.8), gives

$$v_{rn} = \frac{8D_{eff}}{a^2}\sigma - \frac{8D_{eff}\gamma_s}{a^4}\left[4r\left(1 - \cos\left(\frac{\Psi}{2}\right)\right) + a\sin\left(\frac{\Psi}{2}\right)\right]. \tag{A.12}$$

Interparticle stress σ can be expressed as ratio of residual force between particles F_n transmitted through the neck described by the circle cross section area with a diameter of a:

$$\sigma = \frac{F_n}{A_{gb}} = \frac{F_n}{\pi a^2}. \tag{A.13}$$

Substituting Eq. (A.13) into Eq. (A.12) and coverting it, we obtain the equation of the normal force between two particles interacting during sintering:

$$F_n = \frac{\pi a^4}{8D_{eff}} v_{rn} + \pi \gamma_S \left[4r \left(1 - \cos \frac{\Psi}{2} \right) + a \sin \frac{\Psi}{2} \right]. \tag{A.14}$$

Estimation of material parameters of sintering model

Appendix B presents the procedure of the estimation of material parameters of sintering model at the example of intermetallic NiAl material. The material model parameters were calculated on the basis of the equations and relations presented in the Subsec. 4.10. To execute the simulation of the sintering process, the following material parameters must be evaluated:

- **Atomic volume** Ω – depends on the atomic mass m_a and density ρ_{theo} and is given by Eq. (4.82). In the case of intermetallic NiAl, Eq. (4.82) is not completely satisfied by the presence of two types of atoms – Ni and Al. The value of the atomic volume of NiAl can be calculated by taking the mean value of the atomic mass of Ni and Al:

  $m_a^{\text{Ni}} = 58.69\text{u}$ (taken from [242]),
  $m_a^{\text{Al}} = 26.98\text{u}$ (taken from [242]),
  $\rho_{\text{theo}}^{\text{NiAl}} = 5910 \text{ kg/m}^3$.

  Atomic mass m_a is expressed by u – *unified atomic mass units*, which is equal to $1.66 \cdot 10^{-27}$ kg, thus:

  $$\Omega = \frac{m_a^{\text{Ni}} + m_a^{\text{Al}}}{2 \cdot \rho_{\text{theo}}^{\text{NiAl}}} = \frac{(58.69 + 26.98) \cdot 1.66 \cdot 10^{-27}\text{kg}}{2 \cdot 5910\text{kg/m}^3} = 1.20 \cdot 10^{-29}\text{m}^3$$

  Detailed studies of the atomic volume of NiAl have been carried out in the work [220].

- **Thickness of the grain boundary** δ – taken from Fisher [198] as the value of $\delta = 0.5$ nm as to be a good estimation.

- **Pre-exponential factor of grain boundary diffusion** $D_{0\text{gb}}$ – given by Eq. (4.84), can be estimated from the following calculation:

$$D_{0\text{gb}} = D'_{0\text{gb}}\exp\left(\frac{\Delta S}{R}\right) = 7.69 \cdot 10^{-7}\,\frac{\text{m}^2}{\text{s}}\,\exp\left(\frac{3.5\text{R}}{\text{R}}\right) = 2.55 \cdot 10^{-5}\,\frac{\text{m}^2}{\text{s}},$$

where

$\Delta S = 3.5\text{R}$ (taken from [186]),

$D'_{0\text{gb}} = 7.69 \cdot 10^{-7}\,\frac{\text{m}^2}{\text{s}}$, calculated from Eq. (4.85):

$$D'_{0\text{gb}} = f\nu_\text{D}\lambda^2 = 0.727 \cdot 1.27 \cdot 10^{13}\,\text{Hz} \cdot (2.887 \cdot 10^{-10}\,\text{m})^2 = 7.69 \cdot 10^{-7}\,\frac{\text{m}^2}{\text{s}},$$

where

$f = 0.727$ (taken from [189]),
$\nu_\text{D} = 1.27 \cdot 10^{13}$ Hz (calculated from Eq. (4.86)),
$\lambda = 2.887 \cdot 10^{-10}$ m (taken from [220]).

The obtained value of pre-exponential factor of grain boundary diffusion of NiAl is in the good correspondence with the literature data [192], where D_0 of the stoichiometric polycrystalline NiAl varies between $2.71^{+10.0}_{-2.14} \cdot 10^{-5}$ and $2.77^{+2.25}_{-1.24} \cdot 10^{-5}\,\frac{\text{m}^2}{\text{s}}$.

- **Young's modulus** E – a temperature-depended parameter; in the sintering conditions (1400°C) its value is lower (≈ 150 GPa [90]) than in the room-temperature (182 GPa).

- **Poisson's ratio** ν – analogically to Young's modulus, depends on the temperature conditions. The temperature dependence of Poisson's ratio for NiAl has been calculated from the Young's modulus and the shear modulus in [243]. Applying given consideration, ν in the sintering conditions of 1400°C can be calculated by:

$$\nu = 0.307 + 2.15 \cdot 10^{-5} \cdot T = 0.307 + 2.15 \cdot 10^{-5} \cdot 1673\,\text{K} = 0.34,$$

where T is the temperature in Kelvin.

- **Surface energy** γ_s – depends on the materials constants, such as the shear modulus G, the Burgers vector b and the Poisson's ratio ν. The value of γ_s can be estimated by the fairly simple relation (Eq. (4.92)):

$$\gamma_\text{s} = \frac{Gb}{4\pi\,(1-\nu)} = \frac{52\,\text{GPa} \cdot 2.5 \cdot 10^{-10}\,\text{m}}{4\pi\,(1-0.34)} = 1.57\,\text{J/m}^2,$$

where

$G = 52$ GPa in temperature of $1400°$C (taken from[90]),
$b = 2.5 \cdot 10^{-10}$ m (calculation based on [244]),
$\nu = 0.34$ in temperature of $1400°$C (taken from [243]).

The surface energy value of intermetallic NiAl has been measured and simulated in a paper [221], where the average energy for all studied surfaces of NiAl material was 1.53 J/m^2, thus the calculated value is relatively closed to with the literature data.

- **Dihedral angle Ψ** – evaluated by the interfacial energies: the surface energy γ_s and the grain boundary energy γ_gb, using the Eq. (4.91), which can be transformed to the following form:

$$\Psi = 2\arccos\left(\frac{\gamma_\text{gb}}{2\gamma_\text{s}}\right) = 2\arccos\left(\frac{0.89 \text{ J/m}^2}{2 \cdot 1.57 \text{ J/m}^2}\right) = 145,$$

where

$\gamma_\text{s} = 1.57$ J/m^2 was calculated from Eq. (4.92),
$\gamma_\text{gb} = 0.89$ J/m^2 was taken from [221] as a reasonable value of the grain boundary energy for NiAl.

C

Algorithm of generation of geometrical model of powder specimen

Appendix C presents the description of numerical algorithm of generation of initial dense assembly of particles after mixing process. The preparation of a geometrical model is the substantial matter and it may affect the further works on granular material properties [65]. The geometrical model of powder metallurgy specimen should meet many requirements resulting from the microstructural attributes and concerning the geometrics, particle size or particles distribution. The examples of real sintered specimen at the micro and macro scale have been shown in Sec. 3.

The main assumption of the generation of powder metallurgy geometrical model is the isotropy, which results from the state of a powder before the sintering process. Experimental procedure of powder preparation, presented in Subsec. 3.2 as the first stage of powder metallurgy, is based on grinding and mixing. Due to the mechanical treatment, particles of different size are randomly distributed in the whole volume. Furthermore, the powder mixing intensifies irregular configuration of particles, which ensures the same properties (Young's modulus, strength) in every point of the material. One of the main requirements for the generation of a geometric model of sintered specimen is taking into account the real particle size distributions, which improves the comparison of experimental and numerical results of sintering analysis. After the process of mixing the powder is placed in the sintering die in a loose form for further compaction. After a compressive treatment, the material (the green body) is characterized by a relatively low porosity and a dense packing of powder particles, which is the next requirement in the generation of the geometrical model of powder material after mixing.

In order to generate an initial dense arrangement of discrete elements to powder metallurgy application, special numerical procedures are required. Generally, the majority of discrete element models employ one of two types of generation

methods: constructive and dynamic methods. The main feature of the constructive algorithm is the assembly preparation of the geometric model (the position and orientation of the particles) using purely geometrical calculations without simulating the dynamics of particle motion. The main constructive methods include the regular arrangements method, sequential inhibition model, sedimentation techniques, closed front technique and inwards packing algorithm [245].

Dynamic methods are based on the simulation of discrete elements and use the equations of motion in generation procedure to create an initial dense arrangement. Since the motion of each particle has to be simulated with the DEM code during the whole process, these preparation methods require a huge amount of calculations, hence they are rather time-consuming [245]. On the other hand the undeniable advantages of dynamic methods are the simplicity and the fact that required arrangement of particles can be obtained by the most of DEM software. The most common of dynamic methods are particle expansion, multi-layer compaction, isotropic compression and gravitational deposition. In the current work the latter two have been applied together to obtain the initial dense arrangement of discrete elements (Figs. C.1 and C.2).
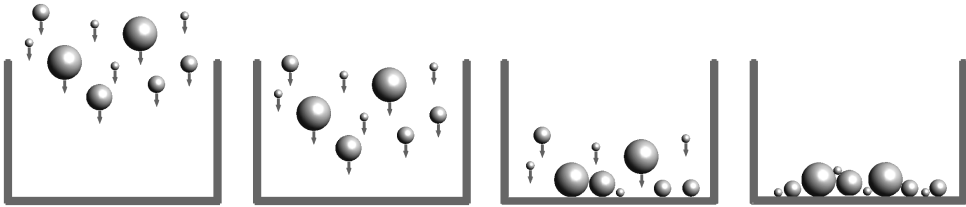
Figure C.1. Scheme of generation of geometrical discrete element model based on gravitational deposition.
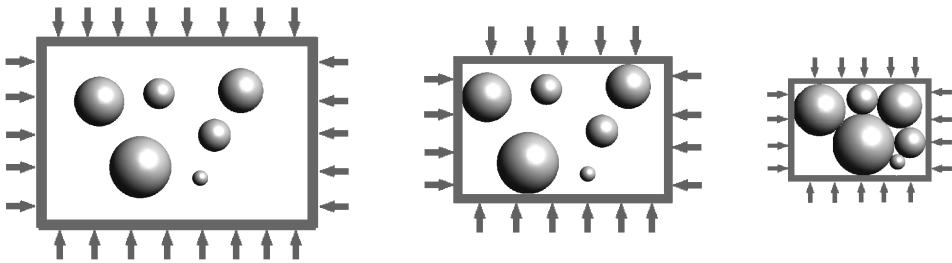
Figure C.2. Scheme of generation of geometrical discrete element model based on isotropic compression.

The generation of loose particles was achieved by the special procedure described schematically in Fig. C.3.
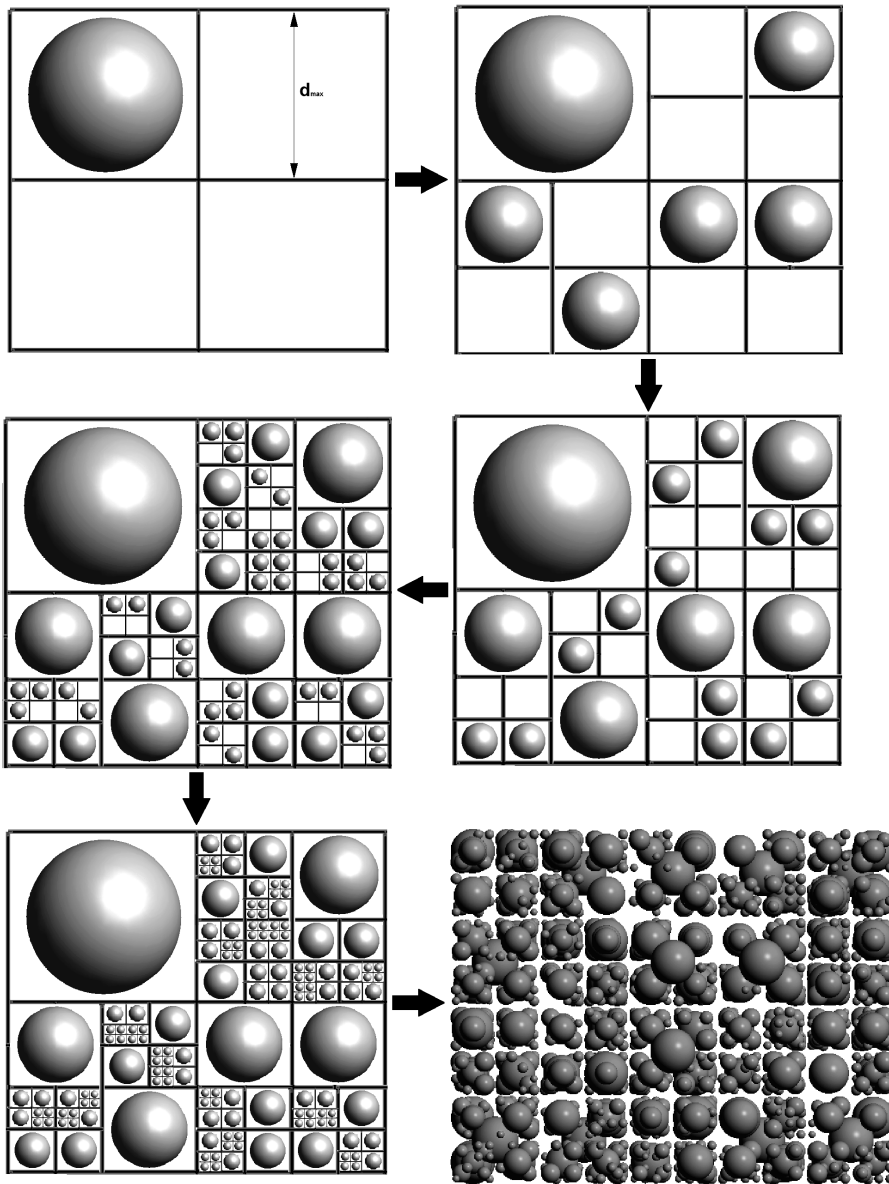
Figure C.3. Scheme of the generation of the geometrical model of the initial loose discrete elements based on 'sub-grid' strategy.

The special procedure was based on the 'sub-grid' strategy. In the first step the entire collection of particles is divided into sets. Set I includes particles with a diameter within the range of $d_{max}/2$ and d_{max}, set II – $d_{max}/4$ and $d_{max}/2$, set III – $d_{max}/8$ and $d_{max}/4$, etc. In the next step, particles of each sets are randomly distributed in the grid characterized by special sizes of cells equal to the maximum particle diameter for each set. Therefore the size of cells for set I equals d_{max}, for set II – $d_{max}/2$, for set III – $d_{max}/4$, etc. The distribution occurs within a few steps starting from the particles from the set I and finishing with the last set. Due to its specific character, the procedure provides the most important requirements in the discrete element generation: the initial dense arrangement of discrete elements by the performance of 'sub-grid' strategy without the penetration of the particles, random distribution and irregular configuration of particles in the volume of the grid (or the sub-grid). In the Fig. C.3 in the last picture the generated initial loose NiAl particles configuration was shown.

In the case of two-phase powder, the algorithm operates similarly. The particles of the first phase (in the current work the intermetallic matrix NiAl) are mixed with the particles of the second phase (ceramic reinforcement Al_2O_3). The only difference refers to the requirement of a uniform distribution of ceramic reinforcement. The algorithm distributing randomly the ceramic particles ensured the condition of isotropy of composite.
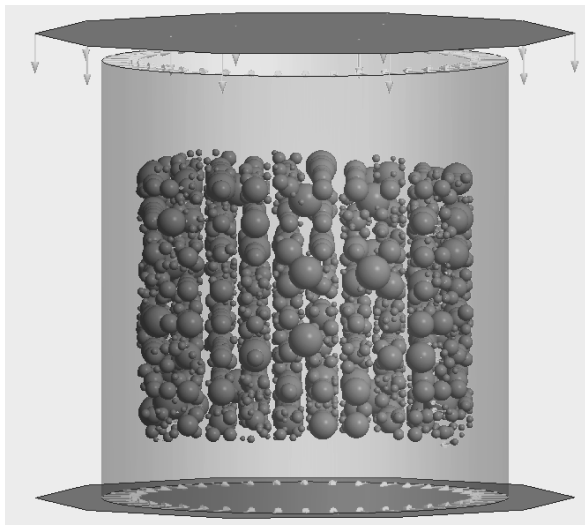
Figure C.4. Scheme of the compaction of the loosely-packed discrete elements based on the dynamic methods.

The second stage of the generation of the geometric model of the powder specimen was the compaction of generated loosely-packed powder. The compaction of the powder was carried out using two dynamic methods in parallel: gravitational deposition, shown schematically in Fig. C.1, and the compression of particles (Fig. C.2). It should be noticed that the scheme of applied compression is a slightly different than the scheme of isotropic compression presented in Fig. C.2. In the current method the cylinder and the walls are in motion, but the bottom of the container is blocked. Figure C.4 shows the generated loosely packed intermetallic powder placed in the container.

To obtained the geometrical model of initially compressed green body, the simulation of dynamic methods was performed. The phenomenon of particle deposition under gravity in parallel is accompanied by an inward movement of the side wall of the container together with the movement of the cylinder in the direction to the particles. The movement of the side wall and the cylinder of the container were calculated to obtain the initial dense geometrical model of discrete elements.

Bibliography

1. I. Chang, Y. Zhao. *Advances in Powder Metallurgy. Properties, Processing and Applications*. Woodhead Publishing, 2013.

2. P. Ramakrishnan. Automotive applications of powder metallurgy. *In Advances in Powder Metallurgy. Properties, Processing and Applications, Eds. by I. Chang, Y. Zhao*, Woodhead Publishing, 2013.

3. M. N. Rahaman. *Ceramic Processing and Sintering*. Marcel Dekker Inc., II Edition, 2003.

4. J. W. Kaczmar, K. Pietrzak, W. Włosiński. The production and application of metal matrix composite materials. *Journal of Materials Processing Technology*, 106:58–67, 2000.

5. J. M. Missiaen. Modelling of sintering: recent developments and perspectives. *Rev. Met. Paris*, (12):1009–1019, 2002.

6. H. E. Exner, T. Kraft. Review on computer simulations of sintering processes. In *Powder Metallurgy World Congress 1998*, volume 2, pages 278–283, EPMA, Shrewsbury, U.K., 1998.

7. D. Gendron. *Numerical and experimental study of sintering at the grain scale* [in French: *Edtude numérique et expérimentale du frittage a l'echelle du grain*]. Ph.D. Thesis, L'Universite Bordeaux I, 2001.

8. J. Pan. Modelling sintering at different length scales. *International Materials Reviews*, 2(17):69–85, 2003.

9. P. Z. Cai, D. J. Green, G. L. Messing. Constrained densification of alumina/zirconia hybrid laminates, I: Experimental observations of processing defects. *Journal of the American Ceramic Society*, 80:1929–1939, 1997.

10. B. Zhang, M. Gasik. Stress evolution in graded materials during densification by sintering processes. *Computational Materials Science*, 25:264–271, 2002.

11. M. Gasik, B. Zhang. A constitutive model and fe simulation for the sintering process of powder compacts. *Computational Materials Science*, 18:93–101, 2000.

12. K. Shinagawa, Y. Hirashima. A constitutive model for sintering of mixed powder compacts. *Mater. Sci. Forum*, 42:1041–1046, 1999.

13. H. G. Kim, O. Gilla, D. Bouvard. A phenomenological constitutive model for sintering of alumina powder. *J. Euro. Ceram. Soc.*, 23:1675–1685, 2003.

14. O. Gillia, D. Bouvard. Phenomenological analysis of densification kinetics during sintering: application to WC-Co mixture. *Materials Science and Engineering A*, 279(1-2):185–191, 2000.

15. M. Abouaf, J. L. Chenot, G. Raisson, P. Bauduin. Finite element simulation of hot isostatic pressing of metal powders. *International Journal for Numerical Methods in Engineering*, 25:191–212, 1988.

16. J. M. Duva, P. D. Crow. The densification of powders by power-law creep during hot isostatic pressing. *Acta Metall. Mater.*, 40:31–35, 1992.

17. A. C. F. Cocks. Inelastic deformation of porous materials. *J. Mech. Phys. Solids*, 37(6):693–715, 1989.

18. P. Sofronis, R. M. McMeeking. Creep of power-law material containing spherical voids. *ASME J. Appl. Mech.*, 59:S88–S95, 1992.

19. P. Ponte Castañeda. The effective mechanical properties of nonlinear isotropic composites. *J. Mech. Phys. Solids*, 39:45–71, 1991.

20. E. A. Olevsky. Theory of sintering: From discrete to continuum. *Mater. Sci. Eng. R.*, 23:41–100, 1998.

21. A. C. F. Cocks. Constitutive modelling of powder compaction and sintering. *Prog. Mater. Sci.*, 46:201–229, 2001.

22. R. M. German. *Sintering Theory and Practice.* Wiley, New York, 1996.

23. R. M. German. Critical overview of sintering computer simulations. In V. Arnhold, C.L. Chu, W.F. Jandeska, H.I. Sanderow, editors, *Advances in Powder Metallurgy & Particulate Materials, Part 9 – Modeling*, pages 1–15. MPIF, Princeton, 2002.

24. G. W. Scherer. Sintering inhomogeneous glasses: Application to optical waveguides. *J. Non-Crystalline Solids*, 34:239–256, 1979.

25. A. Jagota, P. R. Dawson. Micromechanical modeling of powder compacts – Unit problems for sintering traction induced deformation. *Acta Metall. Mater.*, 36:2551–2573, 1988.

26. R. M. McMeeking, L. T. Kuhn. A diffusional creep law for powder compacts. *Acta Metall. Mater.*, 40:961–969, 1992.

27. J. Svoboda, H. Riedel. New solutions describing the formation of interparticle necks in solid-state sintering. *Acta Metall. Mater.*, 43:1–10, 1995.

28. J. Svoboda, H. Riedel, H. Zipse. Equilibrium pore surfaces, sintering stresses and constitutive equations for the intermediate and late stages of sintering – Part I: Computation of equilibrium surfaces. *Acta Metall. Mater.*, 42:435–443, 1994.

29. H. Riedel, D. Z. Sun. Simulation of die pressing and sintering of powder metals, hard metals and ceramics. J.L. Chenot, R.D. Wood, O.C. Zienkiewicz [Eds.] *Numerical Methods in Industrial Forming Processes, Numiform 92*, pages 883–886. A.A. Balkema, Rotterdam, 1998.

30. H. Riedel, V. Kozák, J. Svoboda. Densification and creep in the final stage of sintering. *Acta Metall. Mater.*, 42:3093–3103, 1994.

31. H. Riedel, H. Zipse, J. Svoboda. Equilibrium pore surfaces, sintering stresses and constitutive equations for the intermediate and late stages of sintering, 2: Diffusional densification and creep. *Acta Metall. Mater.*, 42:445–452, 1994.

32. H. Riedel, B. Blug. A Comprehensive Model for Solid State Sintering and its Application to Silicon-Carbide. T.J. Chuang, J.W. Rudnicki [Eds.] *Multiscale Deformation and Fracture in Materials and Structures: The J.R. Rice 60th Anniversary Volume, Solid Mechanics and Its Application, Vol. 84*, pages 49–70. Kluwer Academic Publishers, Dordrecht, 2001.

33. H. A. Häggblad, W. B. Li. A micro mechanical based constitutive model for finite element simulation of hot isostatic pressing of powder. *Comput. Meth. Appl. Mech. Eng.*, 128:191–198, 1995.

34. H. Matsubara. Computer simulations for the design of microstructural developments in ceramics. *Computational Materials Science*, 14:125–128, 1999.

35. M. P. Anderson, G. S. Grest, R. D. Doherty, K. Li, D. J. Srolovitz. Inhibition of grain growth by second phase particles: Three dimensional Monte Carlo computer simulations. *Scripta Metallurgica*, 23(5):753–758, 1989.

36. Q. Yu, S. K. Esche. A Monte Carlo algorithm for single phase normal grain growth with improved accuracy and efficiency. *Computational Materials Science*, 27(3):259–270, 2003.

37. M. Morhac, E. Morhacova. Monte Carlo simulation algorithms of grain growth in polycrystalline materials. *Crystal Research and Technology*, 35(1):117–128, 2000.

38. R. B. Potts. Some generalized order-disorder transformations. *Mathematical Proceedings of the Cambridge Philosophical Society*, 48(1):106–109, 1952.

39. G. N. Hassold, I. W. Chen, D. J. Srolovitz. Computer simulation of final-stage sintering: I, Model kinetics, and microstructure. *Journal of the American Ceramic Society*, 73(10):2857–2864, 1990.

40. J. Pan, A. C. F. Cocks. A numerical technique for the analysis of coupled surface and grain-boundary diffusion. *Acta Mater.*, 43:1395–1406, 1995.

41. J. Pan, A. C. F. Cocks, S. Kucherenko. Finite element formulation of coupled grain-boundary and surface diffusion with grainboundary migration. *Proc. Roy. Soc., London A*, 453:2161–2184, 1997.

42. J. Pan, H. Le, S. Kucherenko, J. A. Yeomans. A model for the sintering of spherical particles of different sizes. *Acta Mater.*, 46:4671–4690, 1998.

43. J. Frenkel. Viscous flow of crystalline bodies under the action of surface tension. *J. Phys. USSR*, 9:385–391, 1945.

44. G. C. Kuczynski. Self diffusion in sintering of metallic particles. *Metal Trans.*, 185:169–178, 1949.

45. W. D. Kingery, M. Berg. Study of the initial stages of sintering of solids by viscous flow, evaporation-condensation and self-diffusion. *J. Appl. Phys.*, 26:1205–1212, 1955.

46. R. L. Coble. Sintering of Crystalline Solids. I. Intermediate and Final State Diffusion Models. *J. Appl. Phys.*, 32:787–792, 1961.

47. J. K. McKenzie, R. Shuttleworth. A phenomenological theory of sintering. *Proc. Phys. Soc. B*, 62:833–852, 1949.

48. M. F. Ashby. A first report on sintering diagrams. *Acta Metall.*, 22:275–289, 1974.

49. E. Arzt. The influence of an increasing particle coordination on the densification of spherical powders. *Acta Metall.*, 30:1883–1890, 1982.

50. H. E. Exner, E. Arzt. Sintering processes. In R.W. Cahn and P. Haasen, editors, *Physical Metallurgy*, volume 30, pages 2628–2662. Elsevier Science, 1996.

51. M. R. Zachariah, M. J. Carrier. Molecular dynamics computation of gas-phase nanoparticle sintering: a comparison with phenomenological models. *Journal of Aerosol Science*, 30:1139–1151, 1999.

52. H. Zhu, R. S. Averback. Molecular dynamics simulations of densification process in nanocrystalline materials. *Materials Science and Engineering A*, A204(1–2):96–100, 1995.

53. Z. Huilong, R. S. Averback. Sintering processes of two nanoparticles: a study by molecular-dynamics simulations. *Phil. Mag. Let.*, 73(1):27–33, 1996.

54. P. Zeng, S. Zajac, P. C. Clapp, J. A. Rifkin. Nanoparticle sintering simulations. *Materials Science and Engineering*, A252:301–306, 1998.

55. K. Kadau, P. Entel, P. S. Lomdahl. Molecular-dynamics study of martensitic transformations in sintered Fe-Ni nanoparticles. *Computer Physics Communications*, 147:126–129, 2002.

56. E. Olevsky, V. Tikare, T. Garino. Multi-scale study of sintering: A review. *Journal of the American Ceramic Society*, 89(6):1914–1922, 2006.

57. L. Jing, O. Stephansson. *Fundamentals of Discrete Element Methods for Rock Engineering: Theory and Applications*. Elsevier, 2007.

58. F. Parhami, R. M. McMeeking. A network model for initial stage sintering. *Mechanics of Materials*, 27:111–124, 1998.

59. C. L. Martin, L. C. R. Schneider, L. Olmos, D. Bouvard. Discrete element modeling of metallic powder sintering. *Scripta Materialia*, 55:425–428, 2006.

60. B. Henrich. *Partikelbasierte Simulationsmethoden in Pulvertechnologie und Nanofluidik*. Ph.D. Thesis, Albert-Ludwigs-Universität Freiburg im Breisgau, 2007.

61. S. Luding, K. Manetsberger, J. Müllers. A discrete model for long time sintering. *Journal of Mechanics and Physics of solids*, 53:455–491, 2005.

62. R. M. Kadushnikov, V. V. Skorokhod, I. G. Kamenin, V. M. Alievskii, E. Nurkanov, D. M. Alievskii. Theory and technology of sintering, heat, and chemical heat-treatment processes computer simulation of spherical particle sintering. *Powder Metallurgy and Metal Ceramics*, 40(3–4):154–163, 2001.

63. L. Olmos, C. L. Martin, D. Bouvard. Sintering of mixtures of powders: Experiments and modelling. *Powder Technology*, 190:134–140, 2009.

64. B. Henrich, A. Wonisch, T. Kraft, M. Moseler, H. Riedel. Simulations of the influence of rearrangement during sintering. *Acta Materialia*, 55:753–762, 2007.

65. A. Wonisch, T. Kraft, M. Moseler, H. Riedel. Effect of different particle size distributions on solid-state sintering: A microscopic simulation approach. *J. Am. Ceram. Soc.*, 92:1428–1434, 2009.

66. A. Wonisch, O. Guillon, T. Kraft, M. Moseler, H. Riedel, J. Rodel. Stress-induced anisotropy of sintering alumina: Discrete element modelling and experiments. *Acta Materialia*, 55:5187–5199, 2007.

67. T. Rasp, Ch. Jamin, A. Wonisch, T. Kraft, O. Guillon. Shape distortion and delamination during constrained sintering of ceramic stripes: Discrete element simulations and experiments. *J. Am. Ceram. Soc.*, 95:586–592, 2012.

68. C. L. Martin, R. K. Bordia. The effect of a substrate on the sintering of constrained films. *Acta Materialia*, 57:549–558, 2009.

69. L. Olmos, C. L. Martin, D. Bouvard, D. Bellet, M. Di Michiel. Investigation of the sintering of heterogeneous powder systems by synchrotron microtomography and discrete element simulation. *J. Am. Ceram. Soc.*, 92:1492–1499, 2009.

70. C. L. Martin, H. Camacho-Montes, L. Olmos, D. Bouvard, R. K. Bordia. Evolution of defects during sintering: Discrete element simulations. *J. Am. Ceram. Soc.,* 92:1435–1441, 2009.

71. L. C. R. Schneider, C. L. Martin, Y. Bultel, D. Bouvard, E. Siebert. Discrete modelling of the electrochemical performance of SOFC electrodes. *Electrochimica Acta*, 52:314–324, 2006.

72. L. C. R. Schneider, C. L. Martin, Y. Bultel, L. Dessemond, D. Bouvard. Percolation effects in functionally graded SOFC electrodes. *Electrochimica Acta*, 52:3190–3198, 2007.

73. J. Liu, N. Jones. Experimental investigation of clamped beams struck transversely by a mass. *Int. J. Impact Eng.*, 6:303–335, 1987.

74. S. Martin, M. Guessasma, J. Léchelle, J. Fortin, K. Saleh, F. Adenot. Simulation of sintering using a non smooth discrete element method. application to the study of rearrangement. *Computational Materials Science*, (84):31–39, 2014.

75. C. Wang, S. Chen. Application of the complex network method in solid-state sintering. *Computational Materials Science*, 69:14–21, 2013.

76. X. Liu, C. L. Martin, G. Delette, J. Laurencin, D. Bouvard, T. Delahaye. Microstructure of porous composite electrodes generated by the discrete element method. *Journal of Power Sources*, 196:2046–2054, 2011.

77. P.C. Angelo, R. Subramanian. *Powder Metallurgy: Science, Technology and Applications*. Prentice-Hall of India Pvt.Ltd, 2008.

78. J. Song. *Experiments, Modelling and Numerical Simulation of the Sintering Process for Metallic or Ceramic Powders*. Ph.D. Thesis, Shanghai Jiaotong University, Shanghai, China, 2007.

79. J. Lis, R. Pampuch. *Sintering* [in Polish: *Spiekanie*]. Wydawnictwo AGH, Kraków, 2000.

80. M. Chmielewski, S. Nosewicz, J. Rojek, S. Mackiewicz, K. Pietrzak, B. Romelczyk. A study of densification and microstructure evolution during hot pressing of NiAl/Al_2O_3 composite. *Advanced Composite Materials*, 24(1):57–66, 2015.

81. S. Nosewicz, J. Rojek, S. Mackiewicz, M. Chmielewski, K. Pietrzak, B. Romelczyk. The influence of hot pressing conditions on mechanical properties of nickel aluminide/alumina composite. *Journal of Composite Materials*, 48(29):3577–3589, 2014.

82. M. Chmielewski, S. Nosewicz, K. Pietrzak, J. Rojek, A. Strojny-Nędza, S. Mackiewicz, J. Dutkiewicz. Sintering behavior and mechanical properties of NiAl, Al_2O_3 and NiAl-Al_2O_3 composites. *Journal of Materials Engineering and Performance*, 23(11):3875–3886, 2014.

83. K. Morsi. Review: reaction synthesis processing of Ni-Al intermetallic materials. *Materials Science and Engineering A*, 299:1–15, 2001.

84. K. Matsuura, T. Kitamutra, M. Kudoh. Microstructure and mechanical properties of NiAl intermetallic compound synthesized by reactive sintering under pressure. *Journal of Materials Processing Technology*, 63:293–302, 1997.

85. T. Chmielewski, D. A. Golanski. New method of in-situ fabrication of protective coatings based on Fe-Al intermetallic compounds. *Proceedings of the Institution of Mechanical Engineers, Part B: Journal of Engineering Manufacture*, 225(B4):611–616, 2011.

86. R. Darolia. Ductility and fracture toughness issues related to implementation of NiAl for gas turbine applications. *Corrosion Science*, 8:1321–1327, 2000.

87. D. Kalinski, M. Chmielewski, K. Pietrzak, K. Choregiewicz. An influence of mechanical mixing and hot-pressing on properties of NiAl/Al$_2$O$_3$ composite. *Archives of Metallurgy and Materials*, 57:695–702, 2012.

88. R. G. Munro. Evaluated material properties for a sintered α-alumina. *J. Am. Ceram. Soc.*, 80(8):1919–28, 1997.

89. P. Patnaik. *Handbook of Inorganic Chemicals*. McGraw-Hill, 2002.

90. J. H. Westbrook, R. L. Fleischer. *Intermetallic Compounds, Volume 3 – Structural Applications of Intermetallic Compounds*. John Wiley and Sons, 2000.

91. D. Kalinski, M. Chmielewski, M. Kozlowski. NiAl matrix composites modified by ceramic particles addition. *Composites theory and practice*, 3:97–102, 2005.

92. A. Michalski, J. Jaroszewicz, M. Rosinski, D. Siemiaszko. NiAl-Al$_2$O$_3$ composites produced by pulse plasma sintering with the participation of the SHS reaction. *Intermetallics*, 14:603–606, 2006.

93. M. M. Moshksar, H. Doty, R. Abbaschian. Grain growth in NiAl-Al$_2$O$_3$ in situ composites. *Intermetallics*, 5:393–399, 1997.

94. D. Tingaud, F. Nardou. Influence of non-reactive particles on the microstructure of NiAl and NiAl-ZrO$_2$ process by thermal explosion. *Intermetallics*, 16:732–737, 2008.

95. M. Chmielewski, K. Pietrzak. Processing, microstructure and mechanical properties of Al$_2$O$_3$-Cr nanocomposite. *Journal of the American Ceramic Society*, 27(2–3):1273–1279, 2007.

96. M. Chmielewski, J. Dutkiewicz, D. Kalinski, L. Litynska-Dobrzynska, K. Pietrzak, A. Strojny-Nedza. Microstructure and properties of hot-pressed molybdenum-alumina composites. *Archives of Metallurgy and Materials*, 57(3):687–693, 2012.

97. W.H. Tuan. The effect of Al$_2$O$_3$ addition on the milling behavior of NiAl powder. *Journal of Materials Engineering and Performance*, 7:613–616, 1998.

98. W.H. Tuan. Toughening alumina with nickel aluminide inclusions. *Journal of the European Ceramic Society*, 20:895–899, 2000.

99. A. Kitaoka, K. Hirota, M. Yoshinaka, Y. Miyamoto, O. Yamaguchi. Toughening and strengthening of NiAl with Al$_2$O$_3$ by the addition of ZrO2(3Y). *J. Am. Ceram. Soc.*, 83:1311–13, 2000.

100. C. L. Hsieh, W. H. Tuan, T. T. Wu. Elastic behaviour of a model two – phase material. *Journal of the European Ceramic Society*, 24:3789–3793, 2004.

101. C. L. Hsieh, W. H. Tuan. Elastic properties of ceramic – metal particulate composites. *Materials Science and Engineering A*, 393:133–139, 2005.

102. M. R. Ghomashchi. Al_2O_3 reinforced Al/Ni intermetallic matrix composite by reactive sintering. *J. Mater. Sci.*, 30:2849–2854, 1995.

103. W. H. Tuan, Y. P. Pai. Mechanical properties of Al_2O_3-NiAl composites. *J. Am. Ceram. Soc.*, 82:1624–26, 1999.

104. Z. Witczak, S. Dymek. Effectivness of dispersion strengthening in the NiAl intermetallic alloy produced by self-sustaining high-temperature synthesis. *Archives of Metallurgy and Materials*, 54:747–753, 2009.

105. A. Upadhyay, R. S. Beniwal, R. Singh. Elastic properties of Al_2O_3-NiAl: a modified version of Hashin-Shtrikman bounds. *Continuum Mech. Thermodyn.*, 24:257–266, 2012.

106. ISO. *2738, Sintered metal materials, excluding hardmetals – Permeable sintered metal materials – Determination of density, oil content and open porosity.* 1999.

107. EN623-2. *Advanced technical ceramics. Monolithic ceramics. General and textural properties. Determination of density and porosity.* 1993.

108. E. Gregorova, Z. Zivcova, W. Pabst. Porosity and pore space characteristics of starch-processed porous ceramics. *J. Mater. Sci.*, 41:6119–6122, 2006.

109. T. M. Besmann, J. C. McLaughlin, H-T. Lin. Fabrication of ceramic composites: forced CVI. *Journal of Nuclear Materials*, 219:31–35, 1995.

110. Y. P. Kwan, J. R. Alcock. The impact of water impregnation method on the accuracy of open porosity measurements. *Journal of Materials Science*, 37(12):2557–2561, 2002.

111. H. A. Bruck, Y. M. Shabana, B. Xu, J. Laskis. Evolution of elastic mechanical properties during pressureless sintering of powder-processed metals and ceramics. *J. Mater. Sci*, 42:7708–7715, 2007.

112. B. A. Auld. *Acoustic Fields and Waves in Solids.* John Wiley and Sons, New York, London, Sydney, Toronto, 1973.

113. International Society for Rock Mechanics. Commission on Standardization of Laboratory and Field Tests. Suggested methods for determining tensile strength of rock materials. *Int. J. Rock Mech. Min. Sci.*, 15:99–103, 1978.

114. ASTM. *D3967-95a, Standard test method for splitting tensile strength of intact rock core specimens*. 1996.

115. J. R. Capua Proveti, G. Michot. The brazilian test: a tool for measuring the toughness of a material and its brittle to ductile transition. *Int. J. Fract.*, 139:455–460, 2006.

116. M. Hangl, A. Börger, R. Danzer, H. M. Luxner. Application of the brazilian disc test for strength measurements on ceramic green bodies. *Fracture Mechanics of Ceramics*, 13:159–167, 2002.

117. I. Doltsinis, F. Osterstock. Modelling and experimentation on the strength of porous ceramics. *Arch. Comput. Meth. Engng*, 12:303–336, 2005.

118. A. Börger, P. Supancic, R. Danzer. *Optimization of the Brazilian Disc Test for ceramic materials, in Ceramic Materials and Components for Engines* (eds J. G. Heinrich and F. Aldinger). Wiley-VCH Verlag GmbH, Weinheim, Germany, 2007.

119. R. Pampuch, K. Haberko, M. Kordek. *Science of ceramic processes* [in Polish: *Nauka o procesach ceramicznych*]. Wydawnictwo Naukowe PWN, Warsaw, 1992.

120. X. Xiaoping, Y. Wuwen, R. M. German. Densification and strength evolution in solid-state sintering. *J. Mater. Sci.*, 37:567–575, 2002.

121. A. P. Roberts, E. J. Garboczi. Elastic properties of model porous ceramics. *Journal of the American Ceramic Society*, 83:3041–3048, 2000.

122. A. P. Roberts, E. J. Garboczi. Computation of the linear elastic properties of random porous materials with wide variety of microstructure. *The Proceedings of the Royal Society of London, Series A – Mathematical, Physical and Engineering Sciences*, 458:1033–1054, 2002.

123. S. Mackiewicz. Theoretical model for calculation of elastic coefficients of composite materials based on polycrystalline diamond and cubic boron nitride. In *Proceedings of AMAS Workshop, Nondestructive Testing of Materials and Structures II*, Warsaw, 2003.

124. E. Ryshkewitch. Compression strength of porous sintered alumina and zirconia. *J Am Ceram Soc*, 36:65–68, 1953.

125. E. A. Olevsky, G. A. Shoales, R. M. German. Temperature effect on strength evolution under sintering. *Materials Research Bulletin*, 36(3–4):449–459, 2001.

126. K. M. Uhl, B. Lucht, H. Jeong, D. K. Hsu. *Mechanical Strength Degradation of Graphite Fiber Reinforced Thermoset Composites Due to Poros-*

ity, in Review of Progress in Quantitative Nondestructive Evaluation, D. O. Thompson, D. E. Chimenti [Eds.]. Springer US, 1988.

127. C. Y. Wu, S. M. Best, A. C. Bentham, B. C. Hancock, W. Bonfield. A simple predictive model for the tensile strength of binary tablets. *European Journal of Pharmaceutical Sciences*, 25:331–336, 2005.

128. M. E. Cura, J. Lagerbom, R. Ritasalo, J. Syren, J. Lotta, O. Soderberg, T. Ritvonen, E. Turunen, S.-P. Hannula. Process parameter optimization of pulsed electric current sintering of recycled WC-8Co powder. *Estonian Journal of Engineering*, 15:255–265, 2009.

129. W. Weglewski, M. Basista, M. Chmielewski, K. Pietrzak. Modelling of thermally induced damage in the processing of Cr-Al_2O_3 composites. *Composites Part B*, 43(2):255–264, 2012.

130. S. Nosewicz, J. Rojek, K. Pietrzak, M. Chmielewski. Viscoelastic discrete element model of powder sintering. *Powder Technology*, (246):157–168, 2013.

131. P. A. Cundall. A computer model for simulating progressive, large scale movements in blocky rock systems. *Proc. Int. Symp. Rock Fracture*, 1, 1971.

132. B. C. Burman. *A Numerical Approach to the Mechanics of Discontinua.* Ph.D. Thesis. University of North Queensland, 1971.

133. P. A. Cundall. Adaptive density-scaling for time-explicit calculations. *Proc. 4th Int. Conf. on Numerical Methods in Geomechanics*, 1982.

134. P. A. Cundall. Formulation of a three-dimensional distinct element model – Part I: A scheme to detect and represent contacts in a system composed of many polyhedral blocks. *International Journal of Rock Mechanics and Mining Sciences and Geomechanics Abstracts*, 25, 1988.

135. B. A. Chappel. *The Mechanics of Blocky Material.* Ph.D. Thesis. Australia National University, 1972.

136. B. A. Chappel. Numerical and physical experiments with discontinua. *Proc. 3rd Cong. ISRM*, 2A, 1974.

137. R. J. Byrne. *Physical and numerical model in rock and soil slope stability.* Ph.D. Thesis. James Cook University of North Queensland, 1974.

138. P. A. Cundall, O. D. L. Strack. A discrete numerical method for granular assemblies. *Geotechnique*, 29:47–65, 1979.

139. P. A. Cundall, O. D. L. Strack. *The Development of Constitutive Laws for Soil using the Distinct Element Method.* Third Intl. Conf. on Num. Meth. in Geomechanics, Aachen, 289-298, 1979.

140. P. A. Cundall, O. D. L. Strack. *Report to NSF Concerning Grant ENG 76-20711, Part II.* Dept. Civ. Engng, University of Minnesota, 1979.

141. J. R. Williams, G. Hocking, G. G. W. Mustoe. *The Theoretical Basis of the Discrete Element Method.* Numerical Methods in Engineering, Theory and Application, Conf. in Swansea, Balkema Publishers, 1985.

142. J. R. Williams, G. G. W. Mustoe. Modal methods for the analysis of discrete systems. *Computers and Geotechnics*, 4, 1987.

143. G. Shi. *Discontinuous deformation analysis – a new numerical model for statics and dynamics of block systems.* Ph.D. Thesis. University of California, 1988.

144. G. Shi, R. E. Goodman. *Discontinuous deformation analysis – a new method for computing stress, strain, and sliding of block systems. In: Cundall, P. A., Sterling, R. L. and Starfield, A. M. (eds), Key Questions in Mechanics.* Proc. of the 29th US Symp. on Rock Mechanics, University of Minnesota,, 1988.

145. R. Barbosa, J. Ghaboussi. *Discrete Finite Element Method.* 1st US Conf. on Discrete Element Methods, 1989.

146. R. Kacanauskas, L. Tumonis, A. Džiugys. Simulation of the normal impact of randomly shaped quasi-spherical particles. *Granular Matter*, 16(3):339–347, 2014.

147. P. A. Cundall, R. D. Hart. Numerical modeling of discontinua. *J. Eng. Comp.*, 9, 1992.

148. P. W. Cleary. Large scale industrial dem modeling. *Engineering Computations*, 21, 2004.

149. P. W. Cleary. The effect of particle shape on simple shear flows. *Powder Technology*, 179, 2008.

150. O. Pouliquen, F. Chevoir. Dense flows of dry granular matterial. *Comptes Rendus Physique*, 3:163–175, 2002.

151. O. R. Walton. *Particle dynamics calculations of shear flow.* J.T. Jenkins, M. Satake [Eds.]. Mechanics of Granular Materials: New Models and Constitutive Relations. Elsevier, 1983.

152. J. Rojek. Discrete element modelling of rock cutting. *Computer Methods in Materials Science*, 7:224–230, 2007.

153. C. Labra, J. Rojek, E. Onate, F. Zarate. Advances in discrete element modelling of underground excavations. *Acta Geotechnica*, 3:317–322, 2008.

154. H. Huang. *Discrete Element Modeling of Tool-Rock Interaction*. Ph.D. Thesis. University of Minnesota, 1999.

155. G. A. D'Addetta, E. Ramm. *Discrete modelling of geomaterials*. In: P. A. Vermeer, W. Ehlers, H. J. Hermann, E. Ramm [Eds.], Continuous and Discontinuous Modelling of Cohesive Frictional Materials. Proc. of CDM 2004, 2004.

156. T. T. Ng. Numerical simulations of granular soil using elliptical particles. *Computers and Geotechnics*, 16, 1994.

157. M. J. Jiang, H. S. Yu, D. Harris. Discrete element modelling of deep penetration in granular soils. *International Journal for Numerical and Analytical Methods in Geomechanics*, 30, 2006.

158. S. Hentz, L. Daudeville, F.V. Donzé. Identification and validation of a discrete element model for concrete. *Journal of Engineering Mechanics – ASCE*, 130, 2004.

159. K. Meguro, M. Hakuno. Fracture analysis of concrete structures by the modified distinct element method. *Structural Engineering/Earthquake Engineering*, 6, 1989.

160. N. M. Azevedo, J. V. Lemos, J. Rocha de Almeida. Influence of aggregate deformation and contact behaviour on discrete particle modelling of fracture of concrete. *Engineering Fracture Mechanics*, 75:569–1586, 2008.

161. Y. R. Kim, D. H. Allen, D. N. Little. Damage-induced modeling of asphalt mixtures through computational micromechanics and cohesive zone fracture. *Journal of Materials in Civil Engineering*, 17, 2005.

162. A. T. Papagiannakis, A. Abbas, E. Masad. *Micromechanical Analysis of Viscoelastic Properties of Asphalt Concretes*. Transportation Research Record, 2002.

163. CIMNE. Dempack, explicit nonlinear dynamic analysis by the finite and discrete element method. *web:<www.cimne.upc.edu/dempack>*.

164. E. Ońate, C. Labra, F. Zarate, J. Rojek. Modelling and simulation of the effect od blast loading on structures using an adaptive blending of discrete and finite element methods. *Risk Analysis, Dam Safety, Dam Security and Critical Infrastructure Management*, pages 365–372, 2012.

165. H. Hertz. On the contact of elastic solids. *Journal für die reine und angewandte Mathematik*, 92:156–171, 1882.

166. K. L. Johnson. *Contact Mechanics*. Cambridge University Press, 1985.

167. L. M. Taylor, D. S. Preece. Simulation of blasting induced rock motion. *Eng. Comput.*, 9(2):243–252, 1992.

168. D. L. Johnson. New method of obtaining volume, grain boundary, and surface diffusion coefficients from sintering data. *J. Appl. Phys.*, 40:192–200, 1969.

169. L.C. De Jonghe, M. N. Rahaman. Sintering stress of homogeneous and heterogeneous powder compacts. *Acta Metall.*, 36:223–229, 1988.

170. A. V. Khomenko, O. V. Yushchenko. Solid-liquid transition of ultrathin lubricant film. *Phys. Rev. E*, 68:036110, 2003.

171. E. Riande, R. Diaz-Calleja, M. G. Prolongo, R. M. Masegosa, C. Salomon. *Polymer Viscoelasticity. Stress and Strain in Practice*. Marcel Dekker, Inc., New York, Basel, 2000.

172. D. W. Van Krevelen. *Properties of Polymers*. Elsevier, 1990.

173. S. Gan, J. C. Seferis, R. B. Prime. A viscoelastic description of the glass transition-conversion relationship for reactive polymers. *Journal of Thermal Analysis*, 37(3):463–478, 1991.

174. J. Sorvari, J. Hamalainen. Time integration in linear viscoelasticity – a comparative study. *Mechanics of Time-Dependent Materials*, 14(3):307–328, 2010.

175. T. Hatada, T. Kobori, M. Ishida, N. Niwa. Dynamic analysis of structures with maxwell model. *Earthquake Engineering and Structural Dynamics*, 29(2):159–176, 2000.

176. A. N. B. Poliakov, P. A. Cundall, Y. Y. Podladchikov, V. A. Lyakhovsky. *An Explicit Inertial Method for the Simulation of Viscoelastic Flow: An Evaluation of Elastic Effects on Diapiric Flow in Two- and Three-Layers Models*, D. Stone, S. K. Runcorn [Eds.], Springer Netherlands, 1993.

177. C. O'Sullivan, J. D. Bray. Selecting a suitable time step for discrete element simulations that use the central difference time integration scheme. *Engineering Computations*, 21:278–303, 2004.

178. Y. T. Feng, K. Han, D. R. J. Owen, J. Loughran. On upscaling of discrete element models: similarity principles. *Engineering Computations*, (26):599–609, 2009.

179. J. F. Douglas, J. M. Gasiorek, J. A. Swaffield, L. B. Jack. *Fluid Mechanics*. 5th ed., Pearson Education, London, 2005.

180. C. Herring. *The Physics of Powder Metallurgy*. McGraw-Hill Book Co., 1951.

181. D. W. Jung. Study of dynamic explicit analysis in sheet metal forming processes using faster punch velocity and mass scaling scheme. *Journal of Materials Engineering and Performance*, 7(4):479–490, 1998.

182. C. Thornton. Numerical simulations of deviatoric shear deformation of granular media. *Géotechnique*, 50:43–53, 2000.

183. X. Tu, J. Andrade. Criteria for static equilibrium in particulate mechanics computations. *International Journal for Numerical Methods in Engineering*, 75(13):1581–1606, 2008.

184. D. Bolster, R. E. Hershberger, R. J. Doneelly. Dynamic similarity, the dimensionless science. *Physics Today*, 9:42–47, 2011.

185. H. Mehrer. *Diffusion in Solids – Fundamentals, Methods, Materials, Diffusion-Controlled Processes*. Springer Series in Solid-State Sciences, 2007.

186. P. Heitjans, J. Kärger. *Diffusion in Condensed Matter Methods, Materials Models*. Springer, III edition, 2010.

187. T. L. Hill. *An Introduction to Statistical Thermodynamics*. New York: Dover, 1986.

188. N. G. Szwacki, T. Szwacka. *Basic Elements of Crystallography*. Pan Stanford Publishing Pte. Ltd, 2010.

189. J. Philibert. *Atom Movements – Diffusion and Mass Transport in Solids*. Les Editions de Physique, Les Ulis, 1991.

190. J. R. Davis. *Copper and Copper Alloys*. ASM International. Handbook Committee, 2004.

191. A. Kuper, H. Letaw, L. Slifkin, E. Sonder, C. T. Tomizuka. Self-diffusion in copper. *Phisical Review*, 96:1224–1225, 1955.

192. S. Frank, S. V. Divinski, U. Sodervall, Chr. Herzig. Ni tracer diffusion in the B2-compound NiAl : Influence of temperature and composition. *Acta mater.*, 49:1399–1411.

193. Chr. Herzig, S.V. Divinski. Essentials in diffusion behavior of nickel- and titanium-aluminides. *Intermetallics*, 12:993–1003, 2004.

194. I. Kaur, W. Gust. *Diffusion in Solid Metals and Alloys*. Springer-Verlag, III edition, 1990.

195. I. Kaur, W. Gust, L. Kozma. *Handbook of Grain and Interphase Boundary Diffusion Data*. Ziegler Press, 1989.

196. E. H. Brown. Plastic asymetrical bending of beams. *Int. J. Mech. Sci.*, 9:77–82, 1963.

197. W. Gust, S. Mayer, A. Bogel, B. Predel. Generalized representation of grain-boundary self-diffusion data. *J. Physique*, 46:537–544, 1985.

198. J. C. Fisher. Calculation of diffusion penetration curves for surface and grain boundary diffusion. *J. Appl. Phys.*, 22:74–77, 1951.

199. I. Kaur, Y. Mishin, W. Gust. *Fundamentals of Grain and Interphase Boundary Diffusion*. Wiley, Chichester West Sussex, 1995.

200. W. D. Kingery, H. K. Bowen, D. R. Uhlmann. *Introduction to Ceramics (2nd ed.)*. John Wiley and Sons, 1976.

201. J. R. Rice, T. J. Chuang. Energy variations in diffusive cavity growth. *Journal of the American Ceramic Society*, 64:46–53, 1981.

202. S. J. L. Kang. *Sintering: Densification, Grain growth and Microstructure*. Elsevier, Amsterdam, 2005.

203. W. R. Tyson, W. A. Miller. Surface free energies of solid metals: Estimation from liquid surface tension measurements. *Surface Science*, 62:267–276, 1977.

204. F. R. de Boer, R. Boom, W. C. M. Mattens, A. R. Miedema, A. K. Niessen. *Cohesion in Metals*. North-Holland, Amsterdam, 1988.

205. M. Methfessel, D. Hennig, M. Scheffler. Calculated surface energies of the 4d transition metals: A study of bond-cutting models. *Applied Physics A*, 55:442–448, 1992.

206. H. L. Skriver, N. M. Rosengaard. Surface energy and work function of elemental metals. *Physical Review B*, 46:7157–7168, 1992.

207. L. Vitos, J. Kollar, H. L. Skriver. Full charge-density calculation of the surface energy of metals. *Physical Review B*, 49:16694–16701, 1994.

208. A. M. Rodríguez, G. Bozzolo, J. Ferrante. Multilayer relaxation and surface energies of FCC and BCC metals using equivalent crystal theory. *Surface Science*, 289:100–126, 1993.

209. P. S. Kislyi, M. A. Kuzenkova. Role of surface energy in the initial sintering period. *Powder Metallurgy And Metal Ceramics*, 8:482–485, 1979.

210. G. Gottstein, L. Shvindlerman. *Grain Boundary Migration in Metals*. Taylor and Francis US, 1999.

211. D. L. Olmsted, S. M. Foiles, E. A. Holm. Survey of computed grain boundary properties in FCC metals: I. Grain boundary energy. *Acta Mater.*, 57:3694–3703, 2009.

212. G. S. Rohrer, E. A. Holm, A. D. Rollett, S. M. Foiles, J. Li, D. L. Olmsted. Comparing calculated and measured grain boundary energies in nickel. *Acta Mater.*, 58:5063–5069, 2010.

213. J. K. Mackenzie. Second paper on the statistics associated with the random disorientation of cubes. *Biometrika*, 45:229–240, 1958.

214. G. Palumbo, K. T. Aust. *Special Properties of Σ Grain Boundaries*, In: *Materials Interfaces: Atomic-Level Structure and Properties*, by D. Wolf, S. Yip [Eds.], Chapman and Hall, London, 1992.

215. M. W. Finnis. Accessing the excess: An atomistic approach to excesses at planar defects and dislocations in ordered compounds. *Physica Status Solidi. A – Applied Research*, 166:397–416, 1998.

216. L. E. Murr. *Interfacial phenomena in metals and alloys*. Addison-Wesley Pub. Co., Advanced Book Program, 1975.

217. H. E. Exner. Principles of single phase sintering. *Rev. Powder Metall. Physic. Ceram.*, 1:1–4, 1979.

218. N. J. A. Sloane. The packing of spheres. *Scientific American*, 250:116–125, 1984.

219. V. A. Levchenko, V. A. Borisenko. Temperature dependence of the elastic modulus of copper and its alloys. *Khimicheskoe i Neftyanoe Mashinostroenie*, (7):11–12, 1978.

220. P. H. Kitabjian, W. D. Nix. Atomic size effects in nial based solid solutions. *Acta Metallurgica*, 46:701–710, 1998.

221. Y. Amouyal, E. Rabkin, Y. Mishin. Correlation between grain boundary energy and geometry in Ni-rich NiAl. *Acta Materialia*, 53:3795–3805, 2005.

222. G. F. Hancock, B. R. McDonnel. Diffusion in the intermetallic compound nial. *Physica Status Solidi (A)*, 4(1):143–150, 1971.

223. S. Kitaoka, T. Matsudaira, M. Wada. Mass-transfer mechanism of alumina ceramics under oxygen potential gradients at high temperatures. *Materials Transactions*, 50(2):1023–1031, 2009.

224. J. Wang, R. Raj. Estimate of the activation energies for boundary diffusion from rate-controlled sintering of pure alumina, and alumina doped with zirconia or titania. *Journal of the American Ceramic Society*, 73(5):1172–1175, 1990.

225. P. Agrawala, K. Conlon, K. J. Bowman, C. T. Sun, F. R. Cichocki JR, K. P. Trumble. Thermal residual stresses in co-continuous composites. *Acta Materialia*, 51:1143–1156, 2003.

226. J. Rojek, G.F. Karlis, L. J. Malinowski, G. Beer. Setting up virgin stress conditions in discrete element models. *Computers and Geotechnics*, 48:228–248, 2013.

227. S. Luding. Micro-Macro Transition for anisotropic, aperiodic, granular materials. *International Journal of Solids and Structures*, 41(21):5821–5836, 2004.

228. C. Miehe, J. Schröder, M. Becker. Computational homogenization analysis in finite elasticity: Material and structural instabilities on the micro- and macro-scales of periodic composites and their interaction. *Comput. Meth. Appl. Mech. Eng.*, 191:4971–5005, 2002.

229. E. Ramm, G. A. D'Addetta, M. Leukart. Interrelations between continuum and discontinuum models for geomaterials. In *VII International Conference on Computational Plasticity COMPLAS 2003*, Barcelona, 2003.

230. V. Kouznetsova. *Computational Homogenization for the Multi-Scale Analysis of Multi-Phase Materials*. Ph.D. Thesis, Technische Universiteit of Eindhoven, 2002.

231. M. Lätzel. *From Microscopic Simulations Towards a Macroscopic Description of Granular Media*. Ph.D. Thesis, University of Stuttgart, 2003.

232. C. Wellmann, C. Lillie, P. Wriggers. Homogenization of granular material modeled by a three-dimensional discrete element method. *Computers and Geotechnics*, 35(3):394–405, 2008.

233. M. Lätzel, S. Luding, H. Herrmann. Macroscopic material properties from quasi-static, microscopic simulations of a two-dimensional shear-cell. *Granular Matter*, 2:123–135, 2000.

234. R. Christensen. *Mechanics of Composite Materials*. John Wiley, New York, 1979.

235. S. Nemat-Nasser, M. Hori. *Micromechanics: Overall Properties of Heterogeneous Materials*. North Holland, Amsterdam, 1993.

236. C. Chang, S. Chao, Y. Chang. Estimates of elastic moduli for granular material with anisotropic random packing structure. *Int. J. Solids and Structures*, 32:1989–2008, 1995.

237. A. S. Edelstein, R. C. Cammaratra. *Nanomaterials: Synthesis, Properties and Applications, Second Edition*. Institute of Physics. Series in Micro and Nanoscience and Technology. Taylor & Francis, 1998.

238. E. A. Olevsky, V. Tikare. *Macro-Meso Scale Modeling of Sintering. Part I, in Recent Developments in Computer Modeling of Powder Metallurgy Processes*, A. Zavaliangos, A. Laptev [Eds.], IOS Press, 2001.

239. W. Węglewski, M. Basista, A. Manescu, M. Chmielewski, K. Pietrzak, Th. Schubert. Effect of grain size on thermal residual stresses and damage in sintered chromium-alumina composites: Measurement and modeling. *Composites Part B-Engineering*, 67:119–124, 2014.

240. D. Bouvard, R. M. McMeeking. The deformation of interparticle necks by diffusion controlled creep. *J. Am. Ceram. Soc.*, 79(3):666–672, 1996.

241. R. L. Coble. Initial sintering of alumina and hematite. *J. Am. Ceram. Soc.*, 41:55–62, 1958.

242. M. E. Wieser, T. B. Coplen. Atomic weights of the elements 2009. *Pure Appl. Chem.*, 83(2):359–396, 2011.

243. C. A. Moose. *Interfacial Shear Studies of Sapphire Fiber-Reinforced Nickel Aluminide Matrix Composites*. M.Sc. Thesis. Pennsylvania State University, 1991.

244. V. Raghavan. *Material Science and Engineering: A First Course*. Prentice-Hall of India Pvt.Ltd, 2004.

245. K. Bagi. An algorithm to generate random dense arrangements for discrete element simulations of granular assemblies. *Granular Matter*, 7:31–43, 2005.